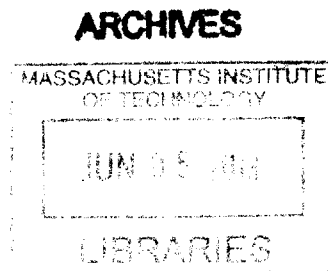


# Selective Metal Ion-Capturing by Striped Nanoparticles

By  
Eun Seon Cho

M.S. Materials Science and Engineering  
Seoul National University, 2008  
B.S. Materials Science and Engineering  
Seoul National University, 2006



SUBMITTED TO  
THE DEPARTMENT OF MATERIALS SCIENCE AND ENGINEERING  
IN PARTIAL FULFILLMENT OF THE REQUIREMENTS FOR THE DEGREE OF  
DOCTOR OF PHILOSOPHY IN MATERIALS SCIENCE AND ENGINEERING  
AT THE  
MASSACHUSETTS INSTITUTE OF TECHNOLOGY

February 2013  
©2013 Massachusetts Institute of Technology  
All rights reserved

Signature of Author: \_\_\_\_\_

Department of Materials Science and Engineering

Jan 9<sup>th</sup> 2013

Certified by: \_\_\_\_\_

Francesco Stellacci

Adjunct Associate Professor of Department of Materials Science and Engineering

Thesis Advisor

Accepted by: \_\_\_\_\_

Gerbrand Ceder

Professor of Department of Materials Science and Engineering

Chair, Departmental Committee on Graduate Students

# Selective Metal Ion-Capturing by Striped Nanoparticles

by Eun Seon Cho

Submitted to the Department of Materials Science and Engineering on January 9<sup>th</sup>  
2013 in Partial Fulfillment of the Requirements for the degree of Doctor of  
Philosophy in Materials Science and Engineering

## Abstract

Nanomaterials have attracted lots of attention due to their tremendous potential in extensive fields, ranging from biology, physics, and chemistry to electronics, and also already proven their superior functionality to conventional materials. The unique properties of nanomaterials comes from their size, morphology, and structure, and frequently a ligand shell structure plays a key role in their distinct behavior and feature since it determines an interaction with environments.

We manipulated gold nanoparticles protected by self-assembled monolayer (SAM) of mixed ligand molecules, which have shown noticeable characteristics. Thiol-ended molecules adsorb onto gold surface, resulting in the formation of SAM. Particularly, two dissimilar ligand molecules undergo a phase-separation on gold nanoparticle surface, and it leads to an ordered structure, alternating striped-like domains. This so-called "striped" structure is induced by a competition between enthalpy and entropy. The longer ligand molecules surrounded by the shorter molecules gain extra conformation entropy at the expense of enthalpy loss, generated by the presence of two different molecules in the same interface.

This unique ligand shell structure, i.e. the striped structure, contributes to the superior properties of our gold nanoparticles. Here we report that the striped gold nanoparticles, consisting of a hydrophilic and a hydrophobic molecule, can selectively capture metal ions, of which sensitivity and selectivity are incomparable to homo-ligand coated nanoparticles and disordered structure nanoparticles. The interaction between striped gold nanoparticles and metal ions was intensively demonstrated with various experimental methods, including UV-vis, FT-IR, ITC, zeta potential, and XPS.

As a part of application, a solid-state metal ion sensor using striped gold nanoparticles with a different pair of hydrophilic and hydrophobic ligands was exploited. The change of the conductance was measured upon the interaction with a particular metal ion, and it exhibited a matchless selectivity and sensitivity. For example, the conductance of gold nanoparticle film with a specific pair of ligands is changed remarkably with methylmercury ions, but that of other kinds films is not, and also it shows extremely low detection limit, which is in the unit of aM ( $10^{-18}$ M),

corresponding to ~600 methylmercury ions in a 1ml of solution. Furthermore, the removal methods of toxic metal ion contaminants from water were manipulated with striped gold nanoparticles, functionalizing with magnetic particles, and also fabricating them as a metal-ion sponge.

Additionally, it was observed that these striped nanoparticles display a different ion-capturing behaviour, depending on temperature, which has rarely shown in other ion-chelating materials. This was induced by the entropy effect of the flexible hydrophilic ligands on the striped nanoparticles.

Finally, the same ion-capturing behaviour was found in nanoparticles of a different core material (i.e. silver) with  $\text{Eu}^{3+}$  ions. This proposed the possibility of the use of other core materials when this striped nanoparticle was applied in a real life.

Thesis Advisor: Francesco Stellacci

## **Acknowledgement**

Firstly, I would like to acknowledge and thank my advisor, Francesco Stellacci. He is an energetic, passionate and brilliant scientist, and he was always encouraging and inspiring me. I was so lucky to be his student. I am very thankful to my committee professors, Prof. Rubner, Prof. Alexander-Katz, and Prof. Gschwend.

I sincerely appreciate SuNMIL group members for being kind and great friends. I really had a great time in the group with them. Particularly, I thank my office-mates Paulo and Yun for their kind help and being pleasant friends. I am also thankful to Mauro for his genuine help with smile, to Miao for her patient STM work, and to Hyewon and Jin-mi for their warm-hearted advice and friendship. Additionally, I thank Arum Amy, who gave me a sincere advice when I joined the group. I am very grateful to my collaborators, Prof. Glotzer and Dr. Hao Jiang at University of Michigan, Prof. Grzybowski, Dr. Hideyuki Nakanishi and Jiwon Kim at Northwestern University, Prof. Clevea Ow-Yang at Sabanci University, Prof. Guiducci and Giulia Cappi at EPFL for their all help and support. Also, I am thankful to Samsung Scholarship for their financial support during my Ph.D.

I thank my best friends in Korea, Da Eun and Tae-eun, for sharing all memories and always standing by me, and Minhee for her warm friendship. I also thank Bit-na for her constant concern and encouragement during my Ph.D. I am very thankful to KGMSE people at MIT and other Korean friends in Boston, especially to ShinYoung, Dahyun, Jeong Yun, Sungmin and Uhi Rinn who supported my life during my Ph.D.

Finally, I would like to thank my family. I truly appreciate my parents for their encouragement, support and endless love throughout my life. Also, I thank my lovely sister and my little nephew, Dawon, who always makes me smile. I deeply love them and appreciate for making my life happier. I appreciated my brother-in-law all the time, and regret that I could not say how much I did, but believe that he is always watching us with his smile.

## Contents Overview

Chapter 1: Introduction and Background .....	13
Chapter 2: Investigation of Metal Ion-Capturing by Striped Gold Nanoparticles.....	40
Chapter 3: Metal-Ion Sensor Using Striped Gold Nanoparticles .....	75
Chapter 4: Removal of Metal Ions from Water Using Striped Gold Nanoparticles ....	84
Chapter 5: Temperature Effect on Ion-Capturing .....	95
Chapter 6: Ion-Capturing with a Different Core Material: Eu <sup>3+</sup> -Binding to Silver Nanoparticles .....	106
Chapter 7: Conclusions and Future Work .....	117
Appendix .....	124

## Table of Contents

1. Introduction and Background .....	13
1.1. Nanoparticles .....	13
1.2. Self-assembled monolayers (SAM) on gold nanoparticles .....	14
1.3. Phase separation of mixed ligands on gold nanoparticle: striped Structure .....	16
1.4. Metal ions in environment, biology and engineering .....	19
1.5. Ion-chelating Materials .....	21
1.5.1. Concept of ion-chelating .....	21
1.5.2. Examples of ion-chelating material .....	22
1.5.3. Theoretical description: thermodynamics and kinetics .....	26
1.5.4. Chelate stability deciding factors .....	29
1.6. General scope of the work .....	31
1.7. References .....	34
2. Investigation of Metal Ion-Capturing by Striped Gold Nanoparticles .....	40
2.1. Introduction .....	40
2.2. Preparation of gold nanoparticles .....	40
2.2.1. Synthesis of striped gold nanoparticles .....	42
2.2.2. Synthesis of other gold nanoparticles for control experiments .....	43
2.2.3. Purification .....	44
2.3. Characterization of the prepared gold nanoparticles .....	45
2.4. Solution based conductivity test .....	49
2.4.1. Concept of conductivity .....	49
2.4.2. HT/EGn striped nanoparticles .....	51
2.4.3. Homo-ligand and disordered structured nanoparticles .....	54
2.4.4. Striped nanoparticles with other compositions .....	56
2.5. Release of captured-metal ions from gold nanoparticles .....	59
2.6. Ion-capturing dependence on the size of gold nanoparticles .....	60
2.7. Characterization of the interaction between gold nanoparticles and metal ions .....	62
2.7.1. Ultraviolet-visible spectroscopy (UV-vis) .....	62
2.7.2. X-ray photoelectron spectroscopy (XPS) .....	63
2.7.3. Fourier transform infrared spectroscopy (FT-IR) .....	65
2.7.4. Isothermal titration calorimetry (ITC) .....	68
2.7.5. Zeta Potential ( $\zeta$ -potential) .....	69
2.7.6. Transmission electron microscope (TEM) .....	71
2.8. References .....	72
3. Metal-Ion Sensor Using Striped Gold Nanoparticles .....	75
3.1. Introduction .....	75
3.2. Preparation of metal-ion sensor .....	76
3.3. Measurement of conductance of gold nanoparticle films .....	77

3.3.1. The films of the striped gold nanoparticles .....	79
3.3.2. The films of homoligand gold nanoparticles .....	80
3.3.3. Measurement in a blank sample .....	81
3.4. References .....	81
4. Removal of Metal Ions from Water Using Striped Gold Nanoparticles.....	84
4.1. Introduction .....	84
4.2. Magnetization of gold nanoparticles: composite nanoparticle.....	85
4.2.1. Magnetic nanoparticles.....	85
4.2.2. Synthesis of magnetic particles functionalized with gold nanoparticles.....	85
4.2.3. Characterization of magnetic nanoparticles functionalized with gold nanoparticles.....	87
4.2.4. Removal of metal ions from water.....	88
4.3. Metal ion sponge .....	89
4.3.1. Fabrication of metal ion sponge.....	89
4.3.2. Absorption of metal ions from water .....	90
4.3.3. Removal of metal ions from an environmental sample.....	91
4.4. References .....	92
5. Temperature Effect on Ion-Capturing.....	95
5.1. Introduction .....	95
5.2. Different ion-capturing behavior on conductivity test .....	96
5.3. Characterization of metal ion-capturing gold nanoparticles at high temperatures.....	99
5.3.1. Isothermal titration calorimetry (ITC).....	99
5.3.2. Fourier transform infrared spectroscopy (FT-IR) .....	101
5.4. Transition temperature .....	102
5.5. References .....	104
6. Ion-Capturing with a Different Core Material: Eu <sup>3+</sup> -Binding to Silver Nanoparticles.....	106
6.1. Introduction .....	106
6.2. Background for lanthanide ions.....	106
6.3. Synthesis and characterization of silver nanoparticles .....	108
6.4. Investigation of the interaction between the striped nanoparticles and Eu <sup>3+</sup> ions .....	109
6.4.1. Conductivity test.....	109
6.4.2. Ultraviolet-visible spectroscopy (UV-vis).....	110
6.4.3. Fluorescence.....	111
6.5. References .....	114
7. Conclusions and Future Work.....	117
7.1. Ongoing and Future work.....	117
7.1.1. Striped gold nanoparticles with various ligand compositions .....	117
7.1.2. Manipulation of a metal-ion sensor for a real-time monitoring .....	118

7.1.3. Sensor array for detecting multiple ions.....	119
7.1.4. Modification of the metal ion sponge .....	120
7.1.5. Striped nanoparticles with different core materials.....	120
7.1.6. Manipulation of a filter membrane for remediation .....	121
7.2. Conclusions .....	121
7.3. References .....	122
8. Appendix.....	124
A.1. Theoretical explanation for ion-capturing by striped nanoparticles .....	124
A.2. Supporting materials for metal ion sensor (Chapter 3) .....	128
A.2.1. Determination of the detection limit.....	128
A.2.2. Reversibility of the sensor .....	129
A.2.3. Selectivity upon the exposure to mixed ions .....	131
A.2.4. Application to environmental samples.....	133
A.3. References .....	135



## List of Figures

<b>Figure 1.1.</b> Schematic image of SAM structure.....	15
<b>Figure 1.2.</b> Representation of hexagonal arrangement of thiolates on gold surface	15
<b>Figure 1.3.</b> (a) Worm-like domain formed on a flat gold surface with its schematic image and simulation result (b) The rippled structure on a gold nanoparticle with its schematic image and STM image.....	17
<b>Figure 1.4.</b> (a) The free volume created by the arrangement of dissimilar ligands on the curved surface (b) The size-range of gold nanoparticle for the rippled structure (green): for the smaller particle, the bulk phase-separation happens, and for the larger particle, the worm-like domain forms.....	18
<b>Figure 1.5.</b> (a) A chemical structure of ethylenediamine and (b) Chelates between $\text{Ni}^{2+}$ and ethylenediamines.....	22
<b>Figure 1.6.</b> (a) A representation of porphyrin, (b) the complex of porphyrin with $\text{Fe}^{2+}$ for the formation of heme, (c) the complex of porphyrin with $\text{Mg}^{2+}$ for the formation of chlorophyll .....	23
<b>Figure 1.7.</b> (a) A chemical structure of EDTA and (b) a chelate of EDTA and a metal ion.....	24
<b>Figure 1.8.</b> Examples of crown ethers.....	26
<b>Figure 1.9.</b> (a) Ligand molecules with various dentates and (b) their binding constants on the complexation with $\text{Ni}^{2+}$ .....	29
<b>Figure 1.10.</b> The chemical structure and abbreviation of ligands.....	33
<b>Figure 1.11.</b> The schematic cartoon of the striped gold nanoparticles composed of two ligands.....	34
<b>Figure 2.1.</b> A typical TEM image of gold nanoparticles synthesized by (a) one-phase method and (b) Stucky method.....	46
<b>Figure 2.2.</b> TGA curve for gold nanoparticles prepared.....	47
<b>Figure 2.3.</b> A typical STM image of the striped gold nanoparticles (The scale bar is 10 nm.).....	49
<b>Figure 2.4.</b> The conductivity test results of various kinds of metal ions with (a) HT/EG1 striped nanoparticles, (b) HT/EG2 striped nanoparticles, and (c) HT/EG3 striped nanoparticles.....	52
<b>Figure 2.5.</b> The conductivity test with HT/EG1 striped nanoparticles and the mixed ions (lithium and cesium ions).....	54
<b>Figure 2.6.</b> The result of conductivity test for (a) EG1 homo-nanoparticle, (b) EG2 homo-nanoparticle, and (c) EG3 homo-nanoparticle.....	55
<b>Figure 2.7.</b> The result of conductivity for gold nanoparticles with EG2 and brHT ...	56
<b>Figure 2.8.</b> The results of conductivity test for gold nanoparticles consisting of EG2 and different spacing group (a) MHO, (b) AH, (c) OT, and (d) BT.....	57
<b>Figure 2.9.</b> The results of conductivity test for OT/EG3 striped nanoparticles with (a) $\text{Na}^+$ , $\text{K}^+$ , $\text{Cs}^+$ and (b) $\text{Ca}^{2+}$ , $\text{Sr}^{2+}$ .....	58
<b>Figure 2.10.</b> The change of the conductivity for (a) $\text{Zn}^{2+}$ + HT/EG1 particles, $\text{Cd}^{2+}$ + HT/EG2 particles, $\text{Cs}^+$ + HT/EG3 particles and (b) $\text{Zn}^{2+}$ , $\text{Cd}^{2+}$ , $\text{Cs}^+$ without gold	

nanoparticles.....	60
<b>Figure 2.11.</b> TEM images and conductivity test result for corresponding fractionated HT/EG3 striped particles with a mean diameter of (a) $2.59 \pm 0.55$ nm, (b) $3.16 \pm 0.51$ nm, (c) $3.72 \pm 0.62$ nm, (d) $4.14 \pm 0.75$ , and (e) $4.64 \pm 0.99$ nm .....	61
<b>Figure 2.12.</b> UV-vis spectra of (a) HT/EG2 nanoparticles before and after adding $K^+$ and (b) HT/EG3 nanoparticles before and after adding methylmercury.....	62
<b>Figure 2.13.</b> A schematic cartoon of FT-IR with ATR accessory.....	65
<b>Figure 2.14.</b> FT-IR spectra for (a) HT/EG1 particles, (b) HT/EG2 particles, and (c) HT/EG3 particles.....	67
<b>Figure 2.15.</b> ITC results for (a) HT/EG2 particles with $K^+$ , (b) HT/EG2 particles with $Cd^{2+}$ , (c) HT/EG3 particles with $Cs^+$ , and (d) HT/EG3 particles with $K^+$ .....	68
<b>Figure 2.16.</b> TEM images for (a) HT/EG2 nanoparticles without $K^+$ and (b) HT/EG2 nanoparticles with $K^+$ .....	71
<b>Figure 3.1.</b> (a) The cartoon of the scheme and dimension of the sensor device and (b) side view of the film of the gold nanoparticle.....	76
<b>Figure 3.2.</b> The j-E dependence for the film of the striped HT/EG3 nanoparticles before exposure to ions (black circles) and after exposure to ions (colored circles): (a) in a solution of $Zn^{2+}$ and (b) in a solution of $CH_3Hg^+$ .....	77
<b>Figure 3.3.</b> The change in conductance for the films of gold nanoparticles upon the exposure to various metal ions; the sensitivity and selectivity were illustrated .....	79
<b>Figure 4.1.</b> TEM images of (a) $Fe_2O_3$ (100 nm for scale bar), (b) $SiO_2/ Fe_2O_3$ (100 nm for scale bar), and (c) gold nanoparticle/ $SiO_2/ Fe_2O_3$ (20 nm for scale bar) .....	87
<b>Figure 4.2.</b> SQUID measurement of (a) $Fe_2O_3$ , (b) $SiO_2/ Fe_2O_3$ , and (c) gold nanoparticle/ $SiO_2/ Fe_2O_3$ .....	87
<b>Figure 4.3.</b> (a) The picture that the composite particles can be easily removed by a magnet and (b) the change in conductivity value at each step: (i) the initial value without $Cd^{2+}$ , (ii) right after adding $Cd^{2+}$ , (iii) after mixing with the composite particles, followed by that they being removed, and (iv) after the captured $Cd^{2+}$ being released by heating the solution up to $80^\circ C$ .....	88
<b>Figure 4.4.</b> (a) The schematic representation of manipulating the metal ion sponge (black: plastic frame, gray: epoxy resin, purple: nanoparticle-pellet, and (b) The picture of metal ion sponge in a plastic frame.....	90
<b>Figure 5.1.</b> The result of conductivity test for HT/EG3 striped nanoparticles (a) at $40^\circ C$ with $K^+$ and $Cs^+$ , (b) at $50^\circ C$ with $K^+$ , (c) at $60^\circ C$ with $K^+$ .....	96
<b>Figure 5.2.</b> The result of conductivity test for HT/EG3 striped nanoparticles with (a) $Na^+$ , $Ca^{2+}$ , $Fe^{2+}$ , $Zn^{2+}$ , $Cd^{2+}$ , $Ni^{2+}$ , $Cu^{2+}$ and $Co^{2+}$ at room temperature, (b) $Na^+$ , $Ca^{2+}$ , $Fe^{2+}$ , $Zn^{2+}$ , $Cd^{2+}$ , $Ni^{2+}$ , $Cu^{2+}$ and $Co^{2+}$ at $40^\circ C$ and (c) $Ca^{2+}$ , $Fe^{2+}$ , and $Cd^{2+}$ at $50^\circ C$ .....	98
<b>Figure 5.3.</b> ITC results for HT/EG3 particles (a) with $Cs^+$ at $40^\circ C$ , (b) with $Cs^+$ at $60^\circ C$ , (c) with $K^+$ at $40^\circ C$ , (d) with $K^+$ at $50^\circ C$ , and with $K^+$ at $60^\circ C$ .....	100
<b>Figure 5.4.</b> FT-IR spectra of HT/EG3 striped particles at varied temperatures.....	102
<b>Figure 5.5.</b> The change in conductivity of $K^+$ aqueous solution with and without HT/EG3 nanoparticles measured by varying the temperature (a) in 5 degrees and (b) in 3 degrees .....	103
<b>Figure 6.1.</b> A typical TEM image of silver nanoparticles.....	108
<b>Figure 6.2.</b> The conductivity test upon the addition of $Eu^{3+}$ ions for (a) OT/EG3	

striped and EG3 homo-gold nanoparticles and (b) OT/EG3 striped and EG3 homo-silver nanoparticles .....	110
<b>Figure 6.3.</b> The change of UV-vis spectra upon the addition of $\text{Eu}^{3+}$ (a) for the striped silver nanoparticles and (b) for the EG3 homo-silver nanoparticles .....	111
<b>Figure 6.4.</b> Variation of emission intensity of $\text{Eu}^{3+}$ on the addition of (a) the striped silver nanoparticles and (b) the EG3 homo-silver nanoparticles, and (c) the intensity ratio of the transition of $^5\text{D}_0$ to $^7\text{F}_2$ transition and $^5\text{D}_0$ to $^7\text{F}_1$ transition for both types of silver nanoparticles .....	112
<b>Figure 7.1.</b> A schematic representation of a real-time monitoring sensor .....	119
<b>Figure A.1.</b> Molecular simulations of ion trapping; a snapshot from MD simulations shows that the ion is trapped near the edge of an EGN stripe .....	124
<b>Figure A.2.</b> The structures and lifetime of the longest-lasting ion-trapping motifs found in the simulations of the HT/EG <sub>2</sub> and HT/EG <sub>3</sub> nanoparticles.....	125
<b>Figure A.3.</b> Reversibility of the film of the striped nanoparticle (a) I-V characteristic plots of the film of HT/EG <sub>2</sub> particles (i) before no ion binding, (ii) after binding $\text{Cd}^{2+}$ ions, (iii) after releasing $\text{Cd}^{2+}$ by putting the film in 80 °C water, and (iv) after re-binding $\text{Cd}^{2+}$ ions, (b) the change in conductance of HT/EG <sub>2</sub> striped nanoparticle film as a function of time from which $\text{Cd}^{2+}$ ions are being released.....	130
<b>Figure A.4.</b> The film selectivity of HT/EG <sub>2</sub> striped particles upon exposure to the mixture of $\text{Cd}^{2+}$ and $\text{K}^+$ .....	132
<b>Figure A.5.</b> Selectivity of the film of HT/EG <sub>3</sub> striped nanoparticles on exposure to ion mixtures and environmental samples .....	134

## List of Tables

<b>Table 2.1.</b> Summary for ion-capturing effect: (+) means that each gold nanoparticle can capture each ion and (-) means that it cannot.....	53
<b>Table 2.2.</b> XPS analysis for HT/EG1 particles without /with Zn <sup>2+</sup> and HT/EG3 particles without /with CH <sub>3</sub> Hg <sup>+</sup> .....	64
<b>Table 2.3.</b> Change of zeta potential of HT/EG2 striped nanoparticles in the presence of various metal ions.....	70
<b>Table 3.1.</b> The $\chi$ values for the films of EGn homo-nanoparticles .....	81
<b>Table A.1.</b> Detection limits for each pair of nanoparticle and metal ion determined by the two-sample <i>t</i> -test at the 99 % confidence level .....	129
<b>Table A.2.</b> The film sensitivity upon the exposure to the mixture of metal ions.....	131

# 1. Introductions and Background

## 1.1. Nanoparticles

Nanoscale materials have been in the center of conceiving and designing new materials for past decades, having drawn lots of attentions<sup>1-6</sup>. Generally, they are referred to as materials in the feature unit of 1~100 nm, encompassing from quantum dots, nanoparticles, nanowire, nanorods and graphene to carbon nanotubes. They have a nanometer scale length in at least one-dimension, and due to their size, exhibit distinctively different properties from bulk materials, resulting from the quantum size effect. Their unique electric, optical, thermal and magnetic properties are determined by the dimensionality.

Nanoparticles belong to zero-dimensional nanomaterials, and includes noble metal nanoparticles such as gold and silver, oxide nanoparticles such as iron oxide and silicon oxide, and semiconducting nanoparticles (i.e. quantum dots) such as cadmium selenide. The unique properties of nanoparticles depend on their core composition, size, shape, and ligands. With a proper combination of these factors, a desirable characteristic of nanoparticles can be achieved.

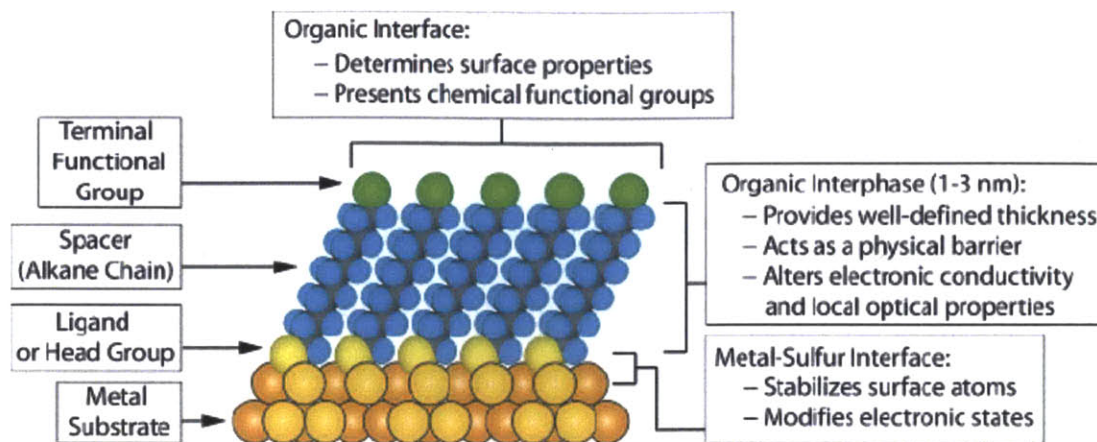
The superior properties of nanometer-sized materials frequently come from their highly increased ratio of surface area to volume. However, the high surface energy

of metal nanoparticles makes them easily aggregated at the same time; hence they need to be stabilized with capping molecules.

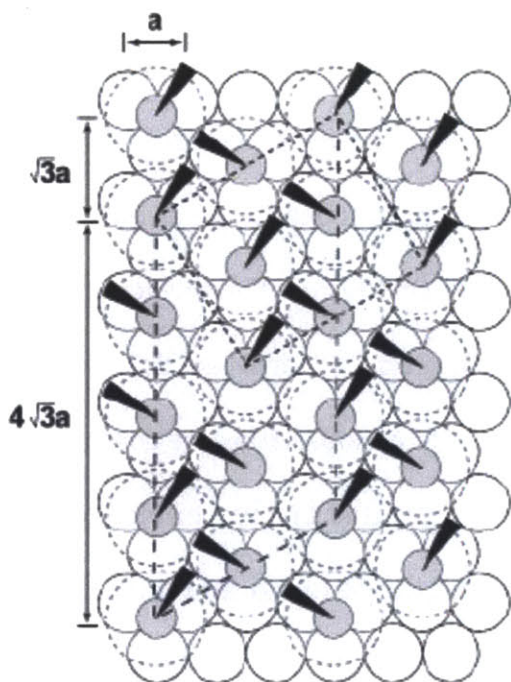
Surface chemistry has been used to stabilize the nanoparticles, promoting a self-assembly of the nanoparticles in a desired way or preventing them from being aggregated. The ligand molecules play an important role in the interaction of nanoparticles with environments surrounding them in the interface. For this reason, normally the surface of nanoparticles is modified with appropriate molecules in a purpose of a particular function.

## **1.2. Self-Assembled Monolayers (SAM) on Gold Nanoparticles**

Self-assembled monolayer (SAM) can be spontaneously formed when molecules ended with functional groups adsorb onto the surface (Figure 1.1)<sup>7-12</sup>. Typical head groups used in the formation of SAM are thiols, silanes, and phosphonates. Ligand molecules tend to anchor to the surface since it decreases the surface energy of the substrate, and the bond formed between the head group of the ligand and the substrate is reasonably strong so that it can stabilize the adsorption<sup>13</sup>. After anchoring, the tail groups pack quite tightly thanks to van der Waals force, which leads to the decrease in free energy of ligand molecules<sup>7,14</sup>.



**Figure 1.1.** Schematic image of SAM structure (Taken from Love, J.C.; Estroff, L. A.; Kriebel, J. K.; Nuzzo, R. G.; Whitesides, G. M. Chem. Rev. 2005, 105, 1103-1169.)



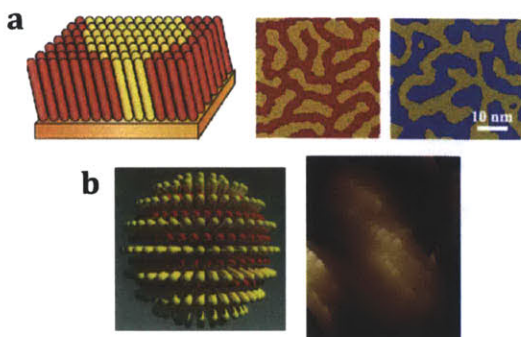
**Figure 1.2.** Representation of hexagonal arrangement of thiolates on gold surface: the arrangement is a  $(\sqrt{3} \times \sqrt{3})R30^\circ$  structure where the sulfur atoms (dark gray circles) are positioned in the 3-fold hollows of the gold lattice (white circles,  $a=2.88 \text{ \AA}$ ). The light gray circles with the dashed lines indicate the approximate projected surface area occupied by each alkane chain. (Taken from Love, J.C.; Estroff, L. A.; Kriebel, J. K.; Nuzzo, R. G.; Whitesides, G. M. Chem. Rev. 2005, 105, 1103-1169.)

Especially, thiol-ended ligands can self-assemble on noble metal surfaces such as gold and silver<sup>7,11,12</sup>. They form highly ordered monolayers on gold surfaces (Au(111)). Alkanethiols tend to pack along their chain, which results in a crystalline and hexagonal arrangement (Figure 1.2). The Au-S bond is quite strong, which is approximately 40~50 kcal/mol in a level of semi-covalent bond, and it makes the bond stable in a wide range of temperature and solvents<sup>7,15,16</sup>. The other end groups can have a variety of functionalities, endowing the surface with different features<sup>17,18</sup>.

### **1.3. Phase separation of mixed ligands on gold nanoparticle: striped structure**

As depicted in the previous section, SAM is spontaneously formed on gold surface with thiolated ligands. Particularly, an interesting phase separation was observed when mixed ligands adsorbed onto the surface<sup>19,20</sup>. On the gold flat surface, SAMs of mixed composition undergo phase separation and produce worm-like domains whose shape is as shown in Figure 1.3(a). When gold nanoparticles are coated with SAMs composed of two dissimilar ligands, phase-separated thin worm-like domains (Figure 1.3(b)), termed hereafter 'striped' domains, can be found, and the formation of the striped domains depends on the size mismatch and immiscibility of ligands, and also size of gold nanoparticle<sup>19,21</sup>.

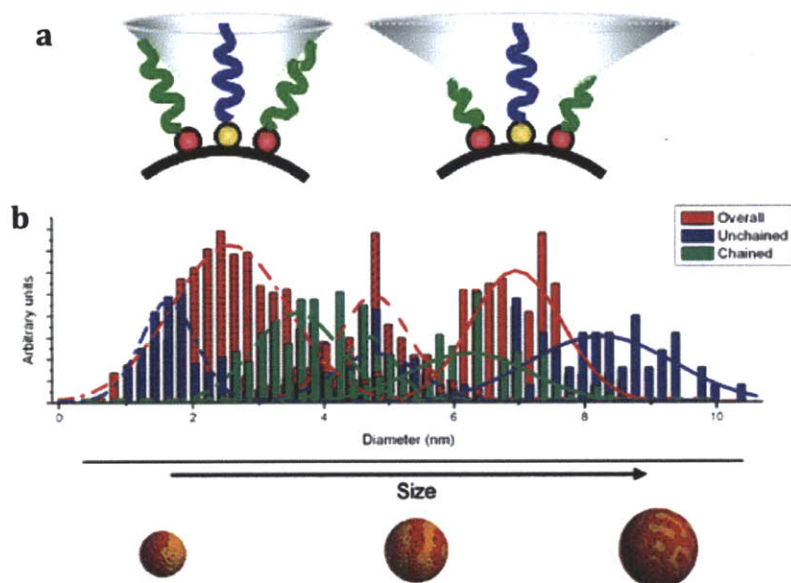




**Figure 1.3.** (a) Worm-like domain formed on a flat gold surface with its schematic image and simulation result (Taken from Singh, C.; Ghorai, P. K.; Horsch, M. A.; Jackson, A. M.; Larson, R. G.; Stellacci, F.; Glotzer, S. C. *Phys. Rev. Lett.* 2007, 99, 226106) (b) The striped structure on a gold nanoparticle with its schematic image and STM cartoon (Taken from Jackson, A. M.; Myerson, J. W.; Stellacci, F. *Nature Materials* 2004, 3, 330-336)

The striped structure is a result of a competition between entropy and enthalpy<sup>19</sup>. When two dissimilar ligands are self-assembled onto gold nanoparticles, there is a loss in enthalpy anytime two dissimilar ligands are close, hence a driving force towards complete ligand separation. However, when one ligand is surrounded by the dissimilar and shorter ligands, there is an increase in free volume for the extra length of the ligand, leading to a gain in conformational entropy (Figure 1.4(a)), compared to a case when the same ligands are close-packed. The balance between enthalpy loss and entropy gain depends on the characteristics of ligands and the size of nanoparticles. Particularly, in a certain size-range of nanoparticles (i.e. within a certain curvature range) and with two dissimilar ligands, the increase of entropy plays a more significant role in phase-separation, and the striped domain becomes thermodynamically favored. However, beyond this certain size-range, the enthalpy

loss is dominant. As a result, the worm-like domains are formed in larger particle. On the contrary bulk phase-separation occurs in the smaller particles, called Janus nanoparticle (Figure 1.4(b))<sup>22</sup>.



**Figure 1.4.** (a) The free volume created by the arrangement of dissimilar ligands on the curved surface (Taken from Singh, C.; Ghorai, P. K.; Horsch, M. A.; Jackson, A. M.; Larson, R. G.; Stellacci, F.; Glotzer, S. C. *Phys. Rev. Lett.* 2007, 99, 226106) (b) The size-range of gold nanoparticle for the rippled structure (green): for the smaller particle, the bulk phase-separation happens, and for the larger particle, the worm-like domain forms (Taken from Carney, R. P.; DeVries, G. A.; Dubois, C.; Kim, H.; Kim, J. Y.; Singh, C.; Ghorai, P. K.; Tracy, J. B.; Stiles, R. L.; Murray, R. W.; Glotzer, S. C.; Stellacci, F. *Journal of the American Chemical Society* 2007, 130, 798-799)

The ligand shell plays an important role in the interaction with the environment surrounding nanoparticles; thus, with the ordered structure of mixed ligands, the striped nanoparticle is expected to show a distinctive property, compared to gold nanoparticles protected with homo-ligands, as other hetero-structured nano-

materials do. For instance, they have shown an enhanced cell-permeability, non-monotonic solubility as a function of ligands ratio, and atypical interfacial energy<sup>23-25</sup>.

#### **1.4. Metal ions in environment, biology and engineering**

Metal elements are generally soluble in water, and most of them exist in a form of positively charged ions in an aqueous solution. They are solvated by water molecules, and the chemical formula in water is  $[M(H_2O)_n]^{z+}$ , where the values of  $n$  and  $z$  are different, depending on oxidation states of metal ions<sup>26,27</sup>.

Such metal ions have a substantial effect in our lives, exiting every field. They are vital elements in biological system. For example,  $Na^+$  and  $K^+$  are crucial elements in water balance, nerve impulses and controlling fluids over cells<sup>28</sup>, and  $Ca^{2+}$  ions are a key component in bones and teeth<sup>29,30</sup>.  $Cu^{2+}$  is cofactor in an activity of enzymes<sup>31,32</sup>, and  $Zn^{2+}$  also has a similar effect besides its role in growth and healing<sup>33,34</sup>. In addition,  $Fe^{2+}$  plays a vital role in carrying oxygen<sup>31</sup>, and  $Co^{3+}$  is essential in vitamin B12<sup>35,36</sup>. Also,  $Mg^{2+}$  greatly contributes to intracellular activity<sup>37</sup>.

Apart from their roles in human body, in the aspect of science and engineering, metal elements occupy a large part in a history of materials due to their excellent mechanical, optical, and electronic properties. For instance, cadmium has been used in battery and electroplating, and also a major element for quantum dots in

laboratory<sup>38,39</sup>. Zinc is used as an anti-corrosion agent, battery, and an element of alloy<sup>40-42</sup>. In addition, cesium is used in nuclear and isotope applications, along with petroleum exploration<sup>43</sup>. Mercury is used in medicine and laboratory application, and historically it was used in diverse areas due to their peculiar property<sup>44,45</sup>.

However, due to their extensive use, a huge amount of metal waste have been released into environment for a long time<sup>46</sup>. Metal pollutants are mainly as a result of human activities, but they also come from a natural phenomenon. For example, substantial amount of mercury is emitted into environment by volcanic eruptions<sup>47</sup>. Such metal contaminants cause a serious problem, reversely threatening our lives. For instance, cadmium caused a serious problem in Japan<sup>48</sup>. People consumed rice constantly, grown up with cadmium-contaminated water, and it brought about bone softening and kidney failure, which was well known as itai-itai disease. Another typical example is methylmercury. Passing through an environmental process, elemental mercury is transformed into an organic form, very frequently into methylmercury, and it is accumulated in an organism<sup>49,50</sup>. Methylmercury is the most toxic form of mercury and bioaccumulated through the food chain. Humans are exposed to methylmercury mostly by the consumption of fish, since 95% of mercury in fish consists of methylmercury<sup>51,52</sup>. As increasing the concentration of methylmercury in fish, it is also necessary to find an appropriate material that can chelate methylmercury with a higher selectivity.

## **1.5. Ion-Chelating Materials**

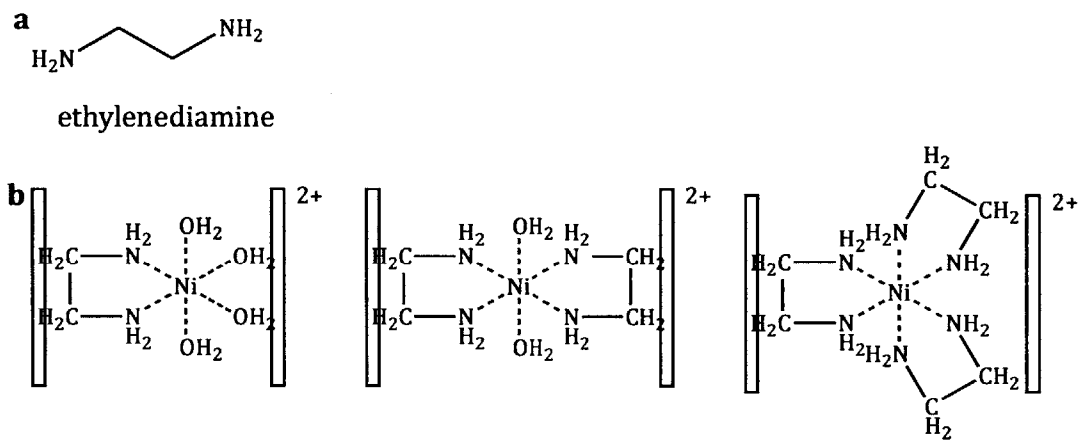
### **1.5.1. Concept of ion-chelating**

Chelation is defined as the formation of coordination bonds between a multidentate ligand and a single atom, which frequently refers to metal ion, and a chelate is a chemical compound produced as a result of a chelation (i.e. a complex of metal ions and chelating agents)<sup>53</sup>. For an expanded explanation, a denticity means a number of atoms in a ligand that can form a bond with a central atom (i.e. metal ion). A monodentate ligand has one denticity, in which only one bond can be formed with a metal ion, and a multidentate (or polydentate) ligand have multiple atoms that can possibly bind to a metal ion. Typically a chelating agent means a ligand molecule more than two dentates. One of key factors that decide the stability of a complex of a metal ion and a chelating agent is the denticity of the ligands. Generally polydentate ligands tend to form a more stable complex than a monodentate or a bidentate ligand, since they provide metal ions with multiple bonds. Besides the denticity, the composition of each dentate plays an important role in forming a bond and also determining the stability. A chelating agent is typically comprised of electron-rich atoms, such as oxygen, nitrogen, and sulfur, so that they can form a coordination bond with a metal ion by donating electrons.

Metal ion-chelating is of great importance biologically, environmentally and also economically. Many biological reactions involve a chelate, and this can be easily

understood, considering that two thirds of enzyme reactions include metal ion catalysts, frequently referred as metalloenzymes<sup>54</sup>. Also, chelates significantly contribute to oxygen transport and photosynthesis, and they play an important role in the uptake and the accumulation of metals into plants and microorganisms<sup>55</sup>. In an economic aspect, chelating agents are utilized in various fields such as nutrition supplements, shampoos, fertilizers, and medicine. Moreover, chelating agents are used to detoxify heavy metal ions, such as mercury, lead and arsenic, in which they extract toxic ions from body by forming an inert complex.

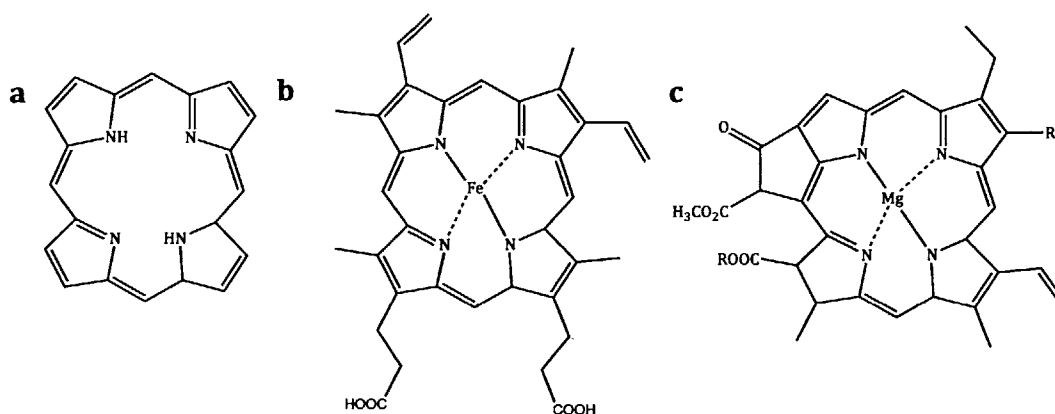
### 1.5.2. Examples of ion-chelating material



**Figure 1.5.** (a) A chemical structure of ethylenediamine and (b) Chelates between  $\text{Ni}^{2+}$  and ethylenediamines

A simple example of a chelating agent is ethylenediamine (Figure 1.5(a)), which is a bidentate<sup>56,57</sup>. One ethylenediamine is able to form two coordination bonds with a

metal ion, such as  $\text{Ni}^{2+}$ , via two nitrogen atoms. A  $\text{Ni}^{2+}$  ion can afford six coordination bonds, which means that three ethylenediamine molecules can make a complex with one  $\text{Ni}^{2+}$ . With one or two ethylenediamine, water molecules are situated in the rest of vacant places, as shown in Figure 1.5(b).

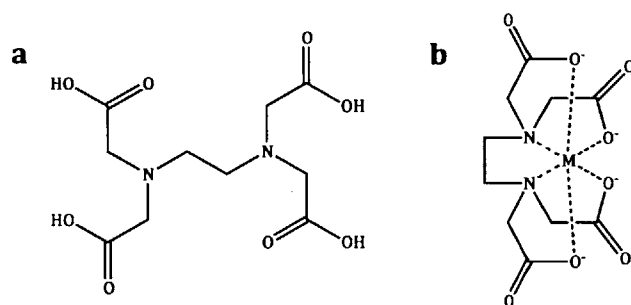


**Figure 1.6.** (a) A representation of porphyrin, (b) the complex of porphyrin with  $\text{Fe}^{2+}$  for the formation of heme, (c) the complex of porphyrin with  $\text{Mg}^{2+}$  for the formation of chlorophyll

A tetradentate ligand includes triethylenetetramine (commonly known as its abbreviation, Trien) and many naturally existing macrocyclic rings such as porphyrin (Figure 1.6(a)). Porphyrin has four nitrogen atoms, and they contribute to the formation of bonds with a metal ion coordinated in the center of the porphyrin ring. Porphyrin produces a chelate, heme, as a result of interacting with  $\text{Fe}^{2+}$  (Figure 1.6(b))<sup>58</sup>. This chelate (heme) is a key component of hemoglobin that transports oxygen in the body. Another chelate naturally formed by porphyrin is chlorophyll, which is a green pigment in plants. A porphyrin makes a complex with  $\text{Mg}^{2+}$  ions, which generates chlorophyll that is critical for photosynthesis (Figure 1.6(c))<sup>59</sup>. Vitamin B12 is also a biologically important chelate, which results from a

formation of coordination bonds between  $\text{Co}^{2+}$  and a tetradentate chelating agent<sup>60</sup>.

Another common ion-chelating agent is ethylenediminetetraacetic acid (EDTA) (Figure 1.7(a))<sup>61</sup>. It is a hexadentate ligand and can form 4- or 6-bonds with metal ions thanks to carboxylate and amine groups, which provide EDTA with a high denticity, functioning as a kind of Lewis base in a complexation with metal ions (Figure 1.7(b)). EDTA is a versatile and effective ion-chelating material, and can make a complex with not only main-group ions, but also transition metal ions. EDTA is familiar to our lives since they are very frequently used in soaps and detergents to make a complex with  $\text{Ca}^{2+}$  and  $\text{Mg}^{2+}$  in water<sup>62</sup>.



**Figure 1.7.** (a) A chemical structure of EDTA and (b) a chelate of EDTA and a metal ion

One of the famous metal ion chelating materials is crown ether, representing macrocyclic molecules, which consists of ether groups in a ring (Figure 1.8)<sup>63-65</sup>. Most typically, it is comprised of ethyleneoxy group ( $-\text{CH}_2\text{CH}_2\text{O}-$ ) as a kind of repeating unit, but it can be other group containing an electron-rich atom such as nitrogen and sulfur. It was firstly found by Charles Pedersen in 1967 when he discovered that 18-crown-6, most popular crown ether type, made a strong complex



with potassium (The first number in crown ether means the number of atoms in a molecule, and the second number indicates the number of electron-donating atoms, which is same as the denticity)<sup>66</sup>. Afterwards, he contrived many kinds of cyclic polyethers and presented diverse synthetic method and thermodynamic studies for their binding properties, leading to the Nobel Prize in 1987. Many kinds of macrocyclic molecules have been manipulated since crown ethers. They strongly bind to a specific metal ion situated in the center of the ring by making coordination bonds. Because the electron-rich atoms such as oxygen tend to be located towards the center of the ring due to the interaction of metal ions, the interior of the ring is hydrophilic, whereas the exterior of the ring is hydrophobic. In this reason, crown ethers are used for phase transfer catalysis since they can dissolve metal ions in nonpolar solvents. They possess selectivity for a specific cation; for example, 18-crown-6 has a high affinity for  $K^+$ , 15-crown-5 for  $Na^+$ , and 14-crown-4 for  $Li^+$ .

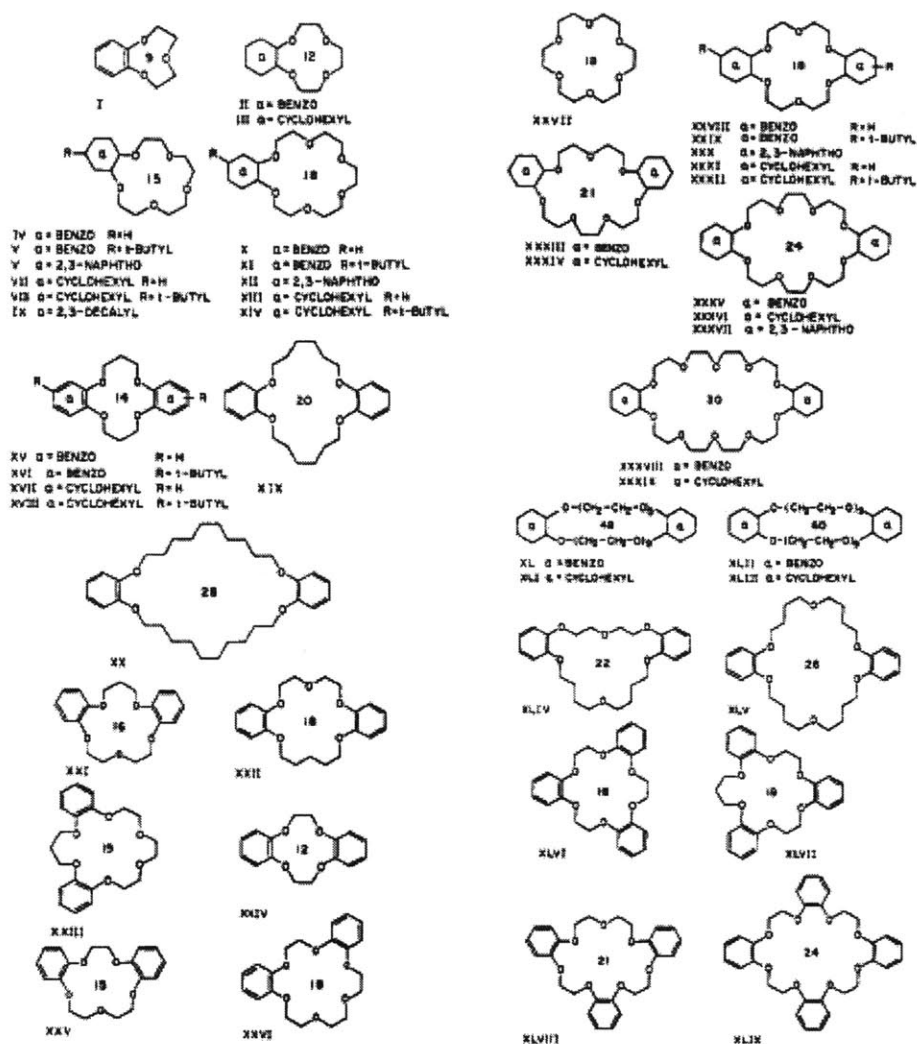
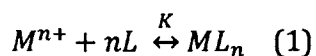


Figure 1.8. Examples of crown ethers (Taken from Pedersen, C. J.; J. Am. Chem. Soc. 1967, 89, 7017-7036)

### 1.5.3. Theoretical description: thermodynamics and kinetics

In a thermodynamic approach, the ion-chelating can be interpreted as an interplay between enthalpy and entropy<sup>67-71</sup>. The chelate formation can be expressed as eqn. (1), where M indicates a metal ion and L refers to a ligand (chelating agent), and this

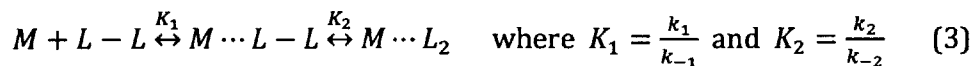
reaction involves a change in free energy with an equilibrium constant, K, as presented in eqn.(2).



$$\Delta G = -RT \ln K = \Delta H - T\Delta S \quad (2)$$

The complex formation is mainly an enthalpy-driven reaction for both non-cyclic and cyclic molecules. It has a negative enthalpy change, which displays the extent of an electronic affinity between a metal ion and a ligand molecule. On the other hand, the entropy is not so favorable to chelating. In most cases,  $\Delta S$  is negative, even though it is sometimes positive in the case of crown ethers. Consequently, the complexation between metal ions and chelating agents happens only when enthalpy gain ( $\Delta H$ ) surpasses entropy loss ( $T\Delta S$ ).

In a kinetic aspect, the reaction can be split into two steps under the assumption of a bidentate ligand,



in which, one dentate forms a coordination with a metal ion firstly, and the other one does later. Under the steady-state approximation, the kinetic equation can be expressed as,

$$\frac{dC}{dt} = \frac{k_1 k_2 [M][L_2]}{k_{-1} + k_2} - \frac{k_1 k_{-2} [ML_2]}{k_{-1} + k_2} \quad (4)$$

in which,  $C$  represents the concentration of a chelate. The eqn. (4) can be re-written as,

$$\frac{dC}{dt} = k_f [M][L] - k_d [ML_2] \quad (5)$$

where  $k_f = \frac{k_1 k_2}{k_{-1} + k_2}$  (formation constant) and  $k_d = \frac{k_1 k_{-2}}{k_{-1} + k_2}$  (dissociation constant).

Under the assumption that a chelate is stable, i.e.  $k_2 \gg k_{-1}$ ,

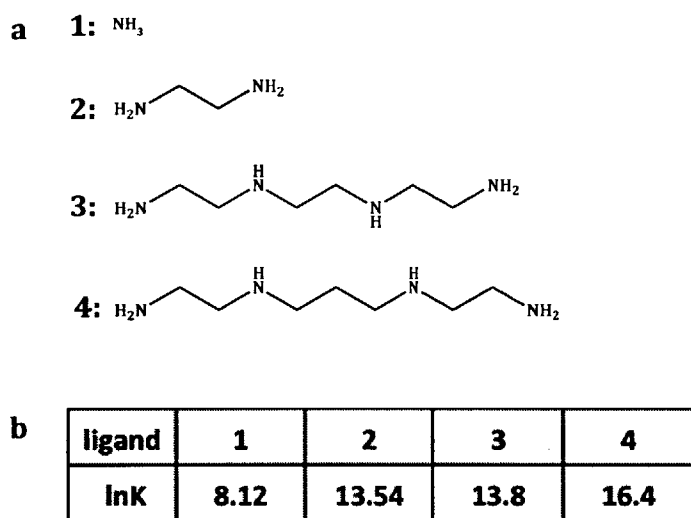
$$k_f = \frac{k_1 k_2}{k_{-1} + k_2} = k_1 \quad (6)$$

$$k_d = \frac{k_1 k_{-2}}{k_{-1} + k_2} = \frac{k_1 k_{-2}}{k_2} \quad (7)$$

For the formation constant, it is same as for a monodentate ligand, which means that a chelating effect, which refers to the enhanced stability of a complex of a metal ion with a multidentate ligand over a similar monodentate ligand, is less relevant for the formation since it is same as other ligands. However, the dissociation constant is highly dependent on a chelating effect.

### 1.5.4. Chelate stability deciding factors

There are several factors affecting the stability of a chelate between a cation and a chelating agent: denticity, geometry and electronic match in the formation of a chelate.



**Figure 1.9.** (a) Ligand molecules with various dentates and (b) their binding constants on the complexation with  $\text{Ni}^{2+}$

Firstly, the denticity is an important factor as briefly mentioned in the previous section. It is a general idea that a chelating agent with more than two dentates forms a more stable complex than a mono-dentate molecule, called a chelate effect. For example,  $\text{Ni}^{2+}$  forms a chelate with ethylenediamine, of which mono-dentate version can be an ammonia molecule, and the formation constant of the complex between  $\text{Ni}^{2+}$  and each molecule is shown in Figure 1.9, in which it is presented that chelating

ligands form a more stable complex than a mono-dentate ligand. It can be explained in the aspect of kinetics introduced in the previous section. Comparing the complexation of a metal ion (M) with one bidentate molecules ( $L_2$ ) to that with two mono-dentate molecules ( $2L$ ), the formation of the second bond ( $M \cdots L$ ) between a metal ion and a bidentate, represented by  $k_2$ , is much easier than a binding of the second mono-dentate molecule to the same metal ion. It is due to an effective concentration; the second nitrogen is held close to the metal ion via ethylene linking group. The value of  $k_2$  is much larger for a bidentate than a mono-dentate, which leads to a smaller  $k_d$ . In other words, dissociation is much slower as a result of a chelating effect. Also, the entropy loss is much greater for a binding of the second mono-dentate molecule than for a second bond formation of a bidentate molecule, since a second atom in the bidentate molecule is already constrained, whereas a second mono-dentate molecule is completely unconstrained before binding.

Furthermore, geometry plays a crucial role in the formation of a stable chelate. Generally it is considered that the more rings can make a more stable complex with metal ions<sup>72</sup>. It is said that a chelate formed by macrocyclic molecule is up to  $10^6$  times more stable than that by non-cyclic molecule with a same number of electron-donating atoms. This is deeply related to the entropy change. The enthalpy change is similar to each other since it is just related to the bond formation between a metal ion and a dentate atom regardless of their geometry. However, the coordination with metal ions requires non-cyclic ligand molecules to sacrifice lots of their degrees of freedom, whereas there is a minimal structural change of cyclic ligand molecules

upon the complexation. Also, in the dissociation, oppositely, breaking the first coordination bond in the complex results in a large distortion of the structure for a cyclic ligand, while it induces a relatively small conformational change for a non-cyclic ligand. In a kinetic aspect, this is interpreted as that the activation energy for the reverse bond-breaking reaction is very high for a cyclic ligand, which indicates that the value of  $k_{-2}$  is very small. This is directly related to a slow dissociation with a small value of  $k_d$ . For a more rigid structure such as cryptand with 3-D shape, the dissociation would be much more difficult, considering a huge deformation upon breaking the first  $M \cdots L$  bond, and this makes a more stable complexation.

Moreover, an electronic match between a chelating ligand and a metal ion is another important factor. It can be explained with HSAB (hard and soft acids and bases) theory, which proposes an idea that soft acids tend to preferentially interact with soft bases and hard acids with hard bases<sup>73,74</sup>. By the Pearson acid base concept, “soft” acids and bases refer to species with large size, low charge states and strongly polarizable, while “hard” acids and bases indicate species with small size, high charge states and weakly polarizable. According to HSAB theory, for instance,  $Fe^{3+}$  binds to  $O^{2-}$  more preferentially than to  $S^{2-}$ .

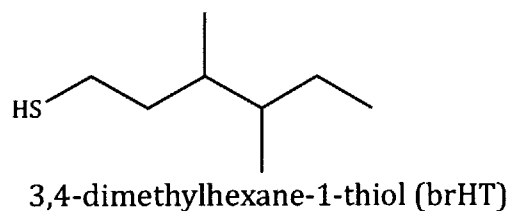
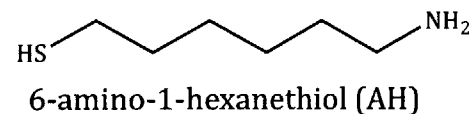
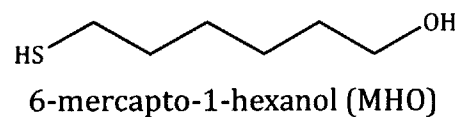
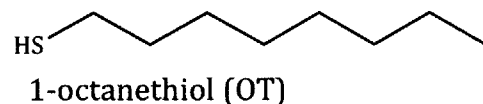
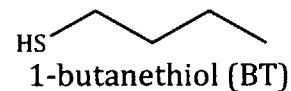
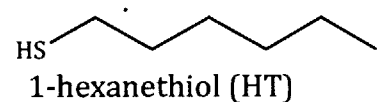
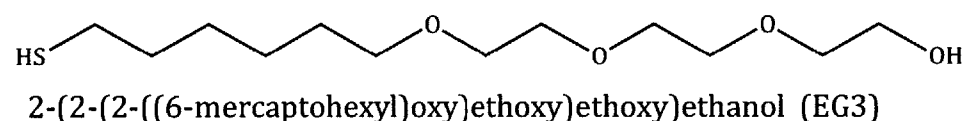
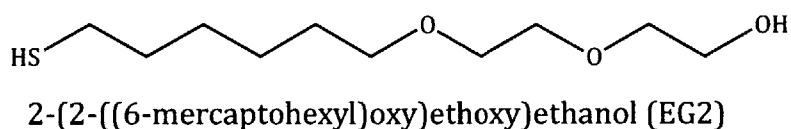
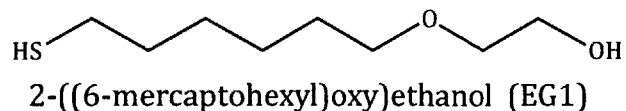
## **1.6. General scope of the work**

In this work, we combined the structure of well-known crown ether with our striped nanoparticles for the application of ion-capturing in a variety of fields. With

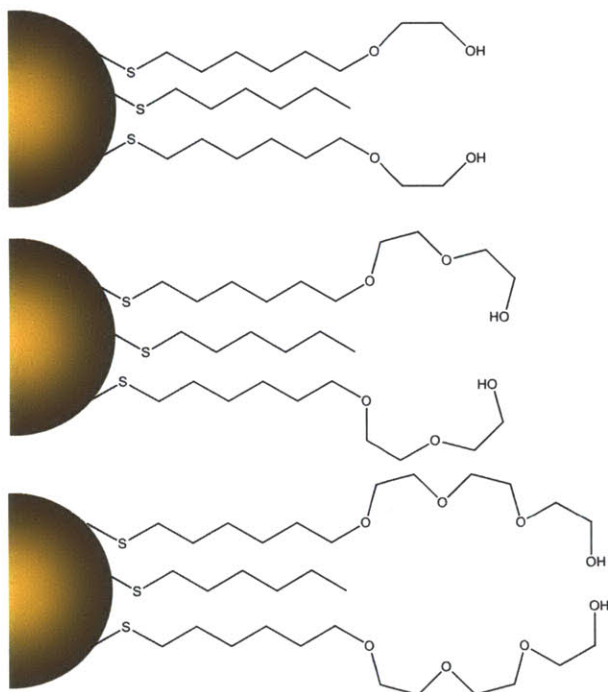
a proper combination of two dissimilar ligands, a hydrophilic and a hydrophobic ligand, it was expected that the striped structure would be formed, which resulted in an “open cavity” for metal ions by the neighboring hydrophilic ligands, which mimicked the structure of crown ethers. The hydrophobic ligand played a critical role in the formation of the ion “pocket” by endowing a space between the neighboring hydrophilic ligands, which would be impossible for homo-ligand protected nanoparticles. The chemical structure and abbreviation of ligands used in our work were summarized in Figure 1.10. Basically, 1-hexanethiol was used as a hydrophobic and shorter ligand, even though other various ligands were also used partially, and three kinds of hydrophilic and longer ligands were used, which were hexanethiols containing ethylene glycol groups: 2-((6-mercaptohexyl)oxy)ethanol (called EG1), 2-(2-((6-mercaptohexyl)oxy)ethoxy)ethanol (called EG2), 2-(2-(2-((6-mercaptohexyl)oxy)ethoxy)ethoxy)ethanol (called EG3). They have been used as one ligand and the number of ethylene glycol groups is varied, comparable to the change of the ring size of crown ethers. The schematic image of gold nanoparticles composed of two ligands is shown in Figure 1.11 where the number of ethylene glycol group contributes to the change of the cavity size, as the ring size of crown ethers alter. Furthermore, this leads to the change in the electrostatic force between metal ions. In this way, the ability of the striped gold nanoparticles to bind different kinds of metal ions were investigated, compared to gold nanoparticles with homo-ligand and also with other compositions. At first, the fundamental experiments were performed to elucidate the interaction between the striped nanoparticles and metal ions, and the engineering manipulation for the application in metal ion sensor and



remediation was carried out. Furthermore, the temperature dependence of the metal ion binding was studied in a scientific aspect, and also the potential use of other core material, except gold, was proposed.



**Figure 1.10.** The chemical structure and abbreviation of ligands



**Figure 1.11.** The schematic cartoon of the striped gold nanoparticles composed of two ligands

## 1.7. References

- 1 Mirkin, C. A., Letsinger, R. L., Mucic, R. C. & Storhoff, J. J. A DNA-based method for rationally assembling nanoparticles into macroscopic materials. *Nature* **382**, 607-609, doi:Doi 10.1038/382607a0 (1996).
- 2 Punties, V. F., Krishnan, K. M. & Alivisatos, A. P. Colloidal nanocrystal shape and size control: The case of cobalt. *Science* **291**, 2115-2117, doi:Doi 10.1126/Science.1057553 (2001).
- 3 Hu, J. T. *et al.* Linearly polarized emission from colloidal semiconductor quantum rods. *Science* **292**, 2060-2063, doi:Doi 10.1126/Science.1060810 (2001).
- 4 Hu, J. T., Odom, T. W. & Lieber, C. M. Chemistry and physics in one dimension: Synthesis and properties of nanowires and nanotubes. *Accounts Chem Res* **32**, 435-445, doi:Doi 10.1021/Ar9700365 (1999).
- 5 Fan, S. S. *et al.* Self-oriented regular arrays of carbon nanotubes and their field emission properties. *Science* **283**, 512-514, doi:Doi 10.1126/Science.283.5401.512 (1999).

- 6 Cui, Y., Wei, Q. Q., Park, H. K. & Lieber, C. M. Nanowire nanosensors for highly sensitive and selective detection of biological and chemical species. *Science* **293**, 1289-1292, doi:Doi 10.1126/Science.1062711 (2001).
- 7 Love, J. C., Estroff, L. A., Kriebel, J. K., Nuzzo, R. G. & Whitesides, G. M. Self-assembled monolayers of thiolates on metals as a form of nanotechnology. *Chem Rev* **105**, 1103-1169, doi:10.1021/cr0300789 (2005).
- 8 Barlow, S. M. & Raval, R. Complex organic molecules at metal surfaces: bonding, organisation and chirality. *Surf Sci Rep* **50**, 201-341, doi:Doi 10.1016/S0167-5729(03)00015-3 (2003).
- 9 Bigelow, W. C., Pickett, D. L. & Zisman, W. A. Oleophobic Monolayers .1. Films Adsorbed from Solution in Non-Polar Liquids. *J Coll Sci Imp U Tok* **1**, 513-538, doi:Doi 10.1016/0095-8522(46)90059-1 (1946).
- 10 Bigelow, W. C., Glass, E. & Zisman, W. A. Oleophobic Monolayers .2. Temperature Effects and Energy of Adsorption. *J Coll Sci Imp U Tok* **2**, 563-591, doi:Doi 10.1016/0095-8522(47)90058-5 (1947).
- 11 Ulman, A. Formation and structure of self-assembled monolayers. *Chem Rev* **96**, 1533-1554, doi:Doi 10.1021/Cr9502357 (1996).
- 12 Ulman, A., Eilers, J. E. & Tillman, N. Packing and Molecular-Orientation of Alkanethiol Monolayers on Gold Surfaces. *Langmuir* **5**, 1147-1152, doi:Doi 10.1021/La00089a003 (1989).
- 13 Vos, J. G., Forster, R. J. & Keyes, T. E. *Interfacial supramolecular assemblies*. (Wiley, 2003).
- 14 Kaifer, A. E. & Gómez-Kaifer, M. *Supramolecular electrochemistry*. (Wiley-VCH, 1999).
- 15 Schlenoff, J. B., Li, M. & Ly, H. Stability and self-exchange in alkanethiol monolayers. *Journal of the American Chemical Society* **117**, 12528-12536, doi:Doi 10.1021/Ja00155a016 (1995).
- 16 Nuzzo, R. G., Dubois, L. H. & Allara, D. L. Fundamental-Studies of Microscopic Wetting on Organic-Surfaces .1. Formation and Structural Characterization of a Self-Consistent Series of Polyfunctional Organic Monolayers. *Journal of the American Chemical Society* **112**, 558-569, doi:Doi 10.1021/Ja00158a012 (1990).
- 17 Koh, S. J. Strategies for controlled placement of nanoscale building blocks. *Nanoscale Res Lett* **2**, 519-545, doi:Doi 10.1007/S11671-007-9091-3 (2007).
- 18 Lud, S. Q. *et al.* Controlling Surface Functionality through Generation of Thiol Groups in a Self-Assembled Monolayer. *Langmuir* **26**, 15895-15900, doi:Doi 10.1021/La102225r (2010).
- 19 Singh, C. *et al.* Entropy-mediated patterning of surfactant-coated nanoparticles and surfaces. *Phys Rev Lett* **99**, doi:Artn 226106 Doi 10.1103/Physrevlett.99.226106 (2007).
- 20 Jackson, A. M., Myerson, J. W. & Stellacci, F. Spontaneous assembly of subnanometre-ordered domains in the ligand shell of monolayer-protected nanoparticles. *Nat Mater* **3**, 330-336, doi:10.1038/nmat1116 (2004).
- 21 Carney, R. P. *et al.* Size limitations for the formation of ordered striped nanoparticles. *Journal of the American Chemical Society* **130**, 798+, doi:Doi 10.1021/Ja077383m (2008).

- 22 Kim, H. *et al.* Synthesis and Characterization of Janus Gold Nanoparticles. *Advanced Materials* **24**, 3857-3863, doi:Doi 10.1002/Adma.201200926 (2012).
- 23 Kuna, J. J. *et al.* The effect of nanometre-scale structure on interfacial energy. *Nat Mater* **8**, 837-842, doi:Doi 10.1038/Nmat2534 (2009).
- 24 Verma, A. *et al.* Surface-structure-regulated cell-membrane penetration by monolayer-protected nanoparticles. *Nat Mater* **7**, 588-595, doi:Doi 10.1038/Nmat2202 (2008).
- 25 Centrone, A. *et al.* The role of nanostructure in the wetting behavior of mixed-monolayer-protected metal nanoparticles. *P Natl Acad Sci USA* **105**, 9886-9891, doi:Doi 10.1073/Pnas.0803929105 (2008).
- 26 Burgess, J. *Metal ions in solution*. (Ellis Horwood ;distributed by Halsted Press, 1978).
- 27 Hunt, J. P. *Metal ions in aqueous solution*. (W.A. Benjamin, 1963).
- 28 Campbell, N. A. *Biology*. 2nd edn, (Benjamin/Cummings Pub. Co., 1990).
- 29 DawsonHughes, B., Harris, S. S., Krall, E. A. & Dallal, G. E. Effect of calcium and vitamin D supplementation on bone density in men and women 65 years of age or older. *New Engl J Med* **337**, 670-676, doi:Doi 10.1056/Nejm199709043371003 (1997).
- 30 Jackson, R. D. *et al.* Calcium plus vitamin D supplementation and the risk of fractures. *New Engl J Med* **354**, 669-683, doi:Doi 10.1056/Nejmoa055218 (2006).
- 31 Lippard, S. J. & Berg, J. M. *Principles of bioinorganic chemistry*. (University Science Books, 1994).
- 32 Adelstein, S. & Vallee, B. L. Copper Metabolism in Man. *New Engl J Med* **265**, 941-&, doi:Doi 10.1056/Nejm196111092651907 (1961).
- 33 Institute of Medicine (U.S.). Panel on Micronutrients. & Institute of Medicine (U.S.). Food and Nutrition Board. *DRI, dietary reference intakes for vitamin A, vitamin K, arsenic, boron, chromium, copper, iodine, iron, manganese, molybdenum, nickel, silicon, vanadium, and zinc : a report of the Panel on Micronutrients ... [et al.]*, Food and Nutrition Board, Institute of Medicine. (National Academy Press, 2001).
- 34 Cotton, F. A. & Cotton, F. A. *Advanced inorganic chemistry / F. Albert Cotton ... [et al.]*. 6th edn, (Wiley, 1999).
- 35 Stangl, G. I., Schwarz, F. J., Muller, H. & Kirchgessner, M. Evaluation of the cobalt requirement of beef cattle based on vitamin B-12, folate, homocysteine and methylmalonic acid. *Brit J Nutr* **84**, 645-653 (2000).
- 36 Schwarz, F. J., Kirchgessner, M. & Stangl, G. I. Cobalt requirement of beef cattle - feed intake and growth at different levels of cobalt supply. *J Anim Physiol an N* **83**, 121-131, doi:Doi 10.1046/J.1439-0396.2000.00258.X (2000).
- 37 Thomas, R. C., Coles, J. A. & Deitmer, J. W. Homeostatic Muffling. *Nature* **350**, 564-564, doi:Doi 10.1038/350564b0 (1991).
- 38 Scoullou, M. J. *Mercury, cadmium, lead : handbook for sustainable heavy metals policy and regulation*. (Kluwer Academic Publishers, 2001).

- 39 Chan, W. C. W. & Nie, S. M. Quantum dot bioconjugates for ultrasensitive nonisotopic detection. *Science* **281**, 2016-2018, doi:Doi 10.1126/Science.281.5385.2016 (1998).
- 40 Ross, T. K. & Wolstenholme, J. Anti-Corrosion Properties of Zinc Dust Paints. *Corros Sci* **17**, 341-351, doi:Doi 10.1016/0010-938x(77)90058-0 (1977).
- 41 Pavlov, A. P., Grigorieva, L. K., Chizhik, S. P. & Stankov, V. K. Nickel-zinc batteries with long cycle life. *J Power Sources* **62**, 113-116, doi:Doi 10.1016/S0378-7753(96)02421-4 (1996).
- 42 Kautek, W., Sahre, M. & Paatsch, W. Transition-Metal Effects in the Corrosion Protection of Electroplated Zinc Alloy Coatings. *Electrochim Acta* **39**, 1151-1157, doi:Doi 10.1016/0013-4686(94)E0030-4 (1994).
- 43 Wiles, D. R., Smith, B. W., Horsley, R. & Thode, H. G. Fission Yields of the Stable and Long-Lived Isotopes of Cesium, Rubidium, and Strontium and Nuclear Shell Structure. *Can J Phys* **31**, 419-431 (1953).
- 44 Liu, J., Shi, J. Z., Yu, L. M., Goyer, R. A. & Waalkes, M. P. Mercury in traditional medicines: Is cinnabar toxicologically similar to common mercurials? *Exp Biol Med* **233**, 810-817, doi:Doi 10.3181/0712-Mr-336 (2008).
- 45 Gibson, B. K. Liquid Mirror Telescopes - History. *J Roy Astron Soc Can* **85**, 158-171 (1991).
- 46 Jarup, L. Hazards of heavy metal contamination. *British Medical Bulletin* **68**, 167-182, doi:10.1093/bmb/ldg032 (2003).
- 47 Dallaglio, M., Brondi, M., Ghiara, E. & Gragnani, R. Mercury in Cold Waters, Thermal, Geothermal and Volcanic Fluids from Italy. *Chem Geol* **70**, 6-6, doi:Doi 10.1016/0009-2541(88)90186-6 (1988).
- 48 Aoshima, K. Recent advances in studies of Itai-itai disease. *Jpn J Tox Env Health* **43**, 317-330 (1997).
- 49 Harada, M. Minamata Disease - Methylmercury Poisoning in Japan Caused by Environmental-Pollution. *Crit Rev Toxicol* **25**, 1-24, doi:Doi 10.3109/10408449509089885 (1995).
- 50 Lebel, J. *et al.* Neurotoxic effects of low-level methylmercury contamination in the Amazonian Basin. *Environ Res* **79**, 20-32, doi:Doi 10.1006/Enrs.1998.3846 (1998).
- 51 Hudson, R. J. M. & Shade, C. W. The chemical form of mercury in fish. *Science* **303**, 763-763 (2004).
- 52 Hall, B. D., Bodaly, R. A., Fudge, R. J. P., Rudd, J. W. M. & Rosenberg, D. M. Food as the dominant pathway of methylmercury uptake by fish. *Water Air Soil Poll* **100**, 13-24 (1997).
- 53 Zelewsky, A. v. *Stereochemistry of coordination compounds*. (Wiley, 1996).
- 54 Jaouen, G. *Bioorganometallics : biomolecules, labeling, medicine*. (Wiley-VCH ;, 2006).
- 55 Waldron, H. A. *Metals in the environment*. (Academic Press, 1980).
- 56 Kodama, M., Fujii, Y. & Ueda, T. Multidentate Ligand Substitution Reactions .11. Substitution Reactions of Nickel(II) Complexes of Diethylenetriamine and Ethylenediaminemonoacetic Acid with Diethylenetriaminepentaacetic Acid and of Nickel(II) Complexes of Diethylenetriamine and Ethylenediamine with

- Cyclohexane-1,2-Diamine-N,N,N',N'-Tetraacetic Acid. *B Chem Soc Jpn* **43**, 2085-&, doi:Doi 10.1246/Bcsj.43.2085 (1970).
- 57 Tsierkezos, N. G., Schroder, D. & Schwarz, H. Complexation of nickel(II) by ethylenediamine investigated by means of electrospray ionization mass spectrometry. *Int J Mass Spectrom* **235**, 33-42, doi:Doi 10.1016/J.ijms.2004.03.005 (2004).
- 58 Scheidt, W. R. & Reed, C. A. Spin-State Stereochemical Relationships in Iron Porphyrins - Implications for the Hemoproteins. *Chem Rev* **81**, 543-555, doi:Doi 10.1021/Cr00046a002 (1981).
- 59 Lindsey, J. S. & Woodford, J. N. A Simple Method for Preparing Magnesium Porphyrins. *Inorg Chem* **34**, 1063-1069, doi:Doi 10.1021/Ic00109a011 (1995).
- 60 Schrauzer, G. Organocobalt Chemistry of Vitamin B12 Model Compounds (Cobaloximes). *Accounts Chem Res* **1**, 97-&, doi:Doi 10.1021/Ar50004a001 (1968).
- 61 Welcher, F. J. *The analytical uses of ethylenediaminetetraacetic acid*. (Van Nostrand, 1958).
- 62 Lindsay, W. L. & Norvell, W. A. Equilibrium Relationships of Zn<sup>2+</sup> Fe<sup>3+</sup> Ca<sup>2+</sup> and H<sup>+</sup> with Edta and Dtpa in Soils. *Soil Sci Soc Am Pro* **33**, 62-& (1969).
- 63 Pedersen, C. J. Cyclic Polyethers and Their Complexes with Metal Salts. *Journal of the American Chemical Society* **89**, 7017-&, doi:Doi 10.1021/Ja01002a035 (1967).
- 64 Pedersen, C. J. & Frensdorff, H. K. Macrocyclic Polyethers and Their Complexes. *Angew Chem Int Edit* **11**, 16-&, doi:Doi 10.1002/Anie.197200161 (1972).
- 65 Christensen, J. J., Hill, J. O. & Izatt, R. M. Ion Binding by Synthetic Macrocyclic Compounds. *Science* **174**, 459-&, doi:Doi 10.1126/Science.174.4008.459 (1971).
- 66 Pedersen, C. J. Cyclic Polyethers and Their Complexes with Metal Salts. *Journal of the American Chemical Society* **89**, 2495-&, doi:Doi 10.1021/Ja00986a052 (1967).
- 67 Haymore, B. L., Lamb, J. D., Izatt, R. M. & Christensen, J. J. Thermodynamic Origin of the Macrocyclic Effect in Crown Ether Complexes of Na<sup>+</sup>, K<sup>+</sup>, and Ba<sup>2+</sup>. *Inorg Chem* **21**, 1598-1602, doi:Doi 10.1021/Ic00134a065 (1982).
- 68 Izatt, R. M., Bradshaw, J. S., Nielsen, S. A., Lamb, J. D. & Christensen, J. J. Thermodynamic and Kinetic Data for Cation Macrocyclic Interaction. *Chem Rev* **85**, 271-339, doi:Doi 10.1021/Cr00068a003 (1985).
- 69 Michaux, G. & Reisse, J. Solution Thermodynamic Studies .6. Enthalpy-Entropy Compensation for the Complexation Reactions of Some Crown Ethers with Alkaline Cations - a Quantitative Interpretation of the Complexing Properties of 18-Crown-6. *Journal of the American Chemical Society* **104**, 6895-6899, doi:Doi 10.1021/Ja00389a002 (1982).
- 70 Wu, H. F., Huan, S. M. & Wu, C. F. Conformational analysis and binding affinity determination for host-guest complexation of alkali metal ions with bis-crown ethers by electrospray mass spectrometry and molecular modeling. *Eur J Mass Spectrom* **8**, 375-380, doi:Doi 10.1255/Ejms.516 (2002).

- 71 Inoue, Y. *et al.* Complexation Thermodynamics of Bis(Crown Ether)S .2. Calorimetric Titration of Complexation of Potassium-Ion with Bis(Benzocrown Ether)S - Enthalpy-Entropy Compensation. *J Phys Chem-US* **92**, 2371-2374, doi:Doi 10.1021/J100319a053 (1988).
- 72 Inoue, Y., Liu, Y., Tong, L. H., Ouchi, M. & Hakushi, T. Complexation Thermodynamics of Crown-Ethers .3. 12-Crown-4 to 36-Crown-12 - from Rigid to Flexible Ligand. *J Chem Soc Perk T 2*, 1947-1950, doi:Doi 10.1039/P29930001947 (1993).
- 73 Jolly, W. L. & Jolly, W. L. *Modern inorganic chemistry*. (McGraw-Hill, 1984).
- 74 Miessler, G. L. & Tarr, D. A. *Inorganic chemistry*. 2nd edn, (Prentice Hall, 1999).

## **2. Investigation of Metal Ion-Capturing by Striped Gold Nanoparticles**

### **2.1. Introduction**

It was expected that the hydrophilic ligands containing ethylene glycol group (EGn) on gold nanoparticle surface could form an “open” cavity so that they could interact with various kinds of metal ions. In this process, the striped structure could play an important role in trapping metal ions by providing an extra space, unlike homo-ligand nanoparticles. Under these assumptions, preliminary experiments were performed to confirm the ion-trapping ability of striped gold nanoparticles. In this chapter, the fundamental procedure to prepare striped gold nanoparticles and their characterization tools are introduced, and also a series of experimental methods to verify the interaction between striped nanoparticles and metal ions are presented.

### **2.2. Preparation of gold nanoparticles**

Gold nanoparticles are synthesized by reducing gold salts in liquid phase as other metal nanoparticles do. Various methods for gold nanoparticles protected by thiolate molecules have been studied. Typically they can be categorized into two groups: the ligand exchange method and the direct synthesis method.



For a long time, gold nanoparticles have been synthesized by being stabilized by sodium citrate ( $\text{Na}_3\text{C}_3\text{H}_5\text{O}(\text{COO})_3$ ), which was firstly developed by Turkevich in 1951<sup>1</sup>. Generally, larger gold nanoparticles were produced in a diameter of 10~20 nm, but quite mono-dispersed. In the reaction, chlorauric acid ( $\text{HAuCl}_4$ ) is reduced by citrate ions, which also act as a capping agent of nanoparticles. The citrate ions can be replaced with a stronger agent such as thiolate.

The direct synthesis methods were developed by Schiffrin and Brust, where gold salts in the presence of thiolate ligands are reduced by an agent (commonly sodium borohydride)<sup>2-4</sup>. They could be categorized into two types, depending on the reaction phase: one is two-phase method, which includes aqueous and organic phase, and the other is one-phase method conducted in ethanol. Both methods give a poly-dispersed nanoparticles in a range of 1~7 nm, and the average particle size can be adjusted by the ratio of gold to ligands, the reduction rate, ligand structure<sup>5</sup>.

Also, recently Stucky and co-workers reported another method with different gold salts, resulting in mono-dispersed nanoparticles<sup>6</sup>. On the contrary to the previous methods that have used strong reducing agents such as sodium borohydride and lithium borohydride, the Stucky method uses a weak reducing agent (amine-borane complex). This plays a key role in making mono-disperse nanoparticles, since a slow reducing process leads to a controlled growth of nanoparticles. The different reducing ability can be confirmed through a color change upon the addition of the reducing agents. For the one-phase synthesis, where the strong reducing agent such

as sodium borohydride is used, an abrupt color change is observed from yellow to black or dark red only with several drops, which means that gold ions are reduced very rapidly. However, for the Stucky synthesis with the weak reducing agent (i.e. amine-borane complexes), the color of the gold solution alters slowly from colorless to brown, red to dark purple, showing a relatively slow reducing rate.

### **2.2.1. Synthesis of striped gold nanoparticles**

In this work, one-phase and modified-stucky methods were used for the synthesis of the striped gold nanoparticles. One-phase methods can be applied more generally, regardless of specific types of ligands, at the expense of a wide-range of size distribution. On the contrary, Stucky method gives mono-dispersed particles, but it requires a solvent and a reaction temperature to be tuned by ligands used, to get a desirable size and ligand ratio of nanoparticles.

In the one-phase method in ethanol, 0.45 mmol of  $\text{HAuCl}_4 \cdot 3\text{H}_2\text{O}$  was dissolved in 40ml of ethanol, followed by the addition of 0.45 mmol of thiol mixtures. After 20 minutes of stirring, 5mmol of  $\text{NaBH}_4$  in 75 ml of ethanol was slowly added drop-wise in 50 minutes, and then kept stirring for additional 3 hours. After completing the reaction, diethyl ether was added into the flask, and the mixture was stored in fridge overnight to precipitate nanoparticles.

In the modified Stucky method, 0.45 mmol of  $\text{AuPPh}_3\text{Cl}$  was mixed with 0.45 mmol

of thiol mixture in 40 ml of chloroform/DMF (1/1) co-solvent, and 5 mmol of tert-butylamine-borane complex was added. The reactant was heated to 55 °C and stirred for 1 hour. After cooling to room temperature, 50 ml of chloroform was added to precipitate out gold nanoparticles.

### **2.2.2. Synthesis of other gold nanoparticles for control experiments**

For control experiments, two kinds of gold nanoparticles were synthesized: one is nanoparticles protected by homo-ligand, i.e. EG ligand, and the other is nanoparticles with a disordered structure. In our previous work, it was reported that the disordered structure was formed when there are some branches (methyl functional groups) in alkanethiols by disturbing an ordered assembly<sup>7</sup>, and it certainly did not show a superior property of the striped nanoparticles. Both types of gold nanoparticles were produced via one-phase method, and it was demonstrated that both nanoparticles had a similar size distribution with the striped nanoparticles.

Homo-ligand nanoparticles were produced by using only EGn ligands, instead of the mixture of ligands, and the disordered structure nanoparticles were prepared with the mixture of 3,4-dimethylhexane-1-thiol (brHT), which is the branched form of hexanethiol, and EG2 ligand. Branched form of 1-hexanethiol (3,4-dimethylhexane-1-thiol) was synthesized with a slight modification of the scheme and different starting materials of the literature<sup>7,8</sup>. The ligand ratio of the disordered structured

nanoparticles was also confirmed via NMR.

### **2.2.3. Purification**

The synthesized gold nanoparticles need to be purified before used to remove impurities such as reactants and residual solvents. The typical methods are centrifugation, vacuum filtration, and dialysis. Here, centrifugation and vacuum filtration were used in the modified-Stucky method and one-phase synthesis, respectively.

The centrifugation is most commonly used in the synthesis of metal nanoparticles, not only in gold nanoparticles. After the completion of reaction, gold nanoparticles were precipitated with the addition of poor solvent and centrifugation. This poor solvent should be chosen carefully so that it can wash out the impurities, but keep gold nanoparticles from aggregating. In our work, chloroform was used, which can dissolve all unreacted starting materials, but precipitate gold nanoparticles. After one-run of centrifuge, by pouring off the supernatants, which include the impurities, and then adding poor solvent, gold nanoparticles were able to be re-dispersed. The solution was centrifuged, and the supernatants were removed again. This step needs to be repeated a few times more, to ensure a complete removal of impurities. Finally, the collected gold nanoparticles were dried under the vacuum overnight to get rid of the residual chloroform.

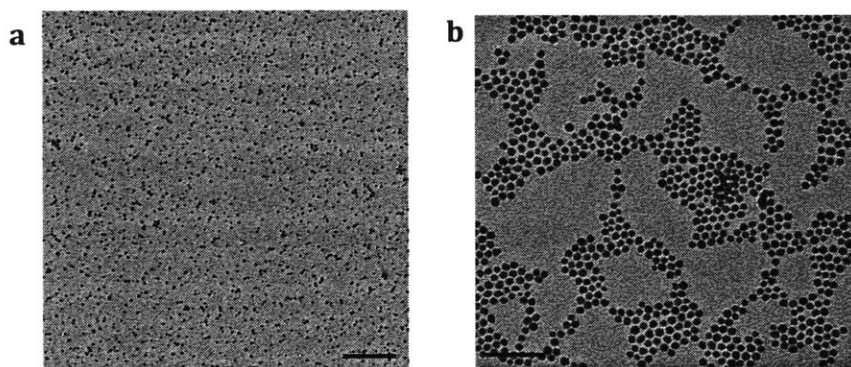
The vacuum filtration is another method for the purification of gold nanoparticles, but it is widely used in various chemical reaction steps. A poor solvent was added into the reactant, following the completion of the reaction, and the solution was kept in the fridge overnight to let gold nanoparticles precipitated. In our work, diethyl ether was used, after solubility test with several kinds of common solvents. The solution was filtered through a filter paper under the vacuum, followed by washing with a few different solvents to dissolve out impurities and reagents. Here, copious amount of ethyl alcohol and also some water were used, followed by acetone in the final step. Lastly, gold nanoparticles on the filter paper were dried under the vacuum, and scraped out from the filter paper, resulting in black solid power.

### **2.3. Characterization of the prepared gold nanoparticles**

Basically, the obtained gold nanoparticles were analyzed with transmission electron microscopy (TEM), nuclear magnetic resonance (NMR), and thermogravimetric analysis (TGA), to get the size distribution, the ligand composition, and the organic amount of gold nanoparticles, respectively. Also, scanning tunneling microscopy (STM) was used to observe the striped structure on gold nanoparticles.

TEM is the most direct method used for the analysis of the core size of metal nanoparticles. A TEM sample was prepared by drop-casting gold nanoparticles dispersed in methanol, and measured after evaporating methanol. The typical TEM image of striped gold nanoparticles is shown in Figure 2.1. Figure 2.1(a) and 2.1(b)

represent the distributions of gold nanoparticles synthesized by one-phase method and Stucky-method, respectively. As expected, gold nanoparticles synthesized by Stucky method have a narrower size distribution.



**Figure 2.1.** A typical TEM image of gold nanoparticles synthesized by (a) one-phase method (the scale bar is 100 nm), and (b) Stucky method (the scale bar is 50 nm)

NMR is also an excellent tool to analyze the ligand shell of nanoparticles. The presence of a sharp peak on the spectrum of nanoparticles implies unreacted free thiols, which is related to the purity of nanoparticles. Furthermore, it can provide the actual ligand ratio on nanoparticles, which could be different from the synthetic ratio. For a precise peak analysis, the gold core was decomposed by adding a small amount of iodine, before measurement, which liberates the adsorbed thiols. The actual composition on nanoparticle surface was calculated with characteristic peaks of each thiol, and in our case, the actual ratio was fairly consistent with the synthetic one. In all NMR analysis, deuterated DMSO (approximately 0.7~1.0 ml) was used as a solvent, and 15~20 mg of nanoparticles were used for measurement.

TGA is one of the most common tools to analyze the organic amount of a certain materials. TGA measurement was performed after confirming the absence of impurities such as unreacted free thiols and residual gold salts with NMR, and the actual amount of each thiol was determined, combining with the composition data from NMR. According to TGA measurement, in which approximately 5 mg of nanoparticles were used and the temperature was raised in the rate of 5 °C/min from 25 °C to 800 °C, the ligand molecules consist of 20 w% in gold nanoparticles, as shown in Figure 2.2.

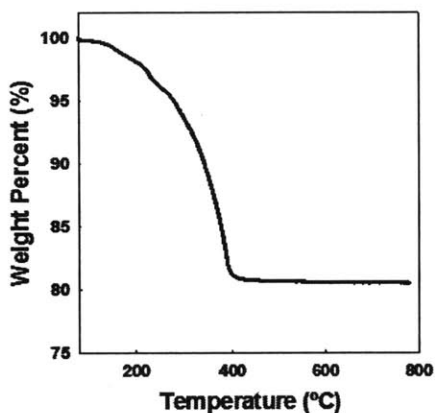
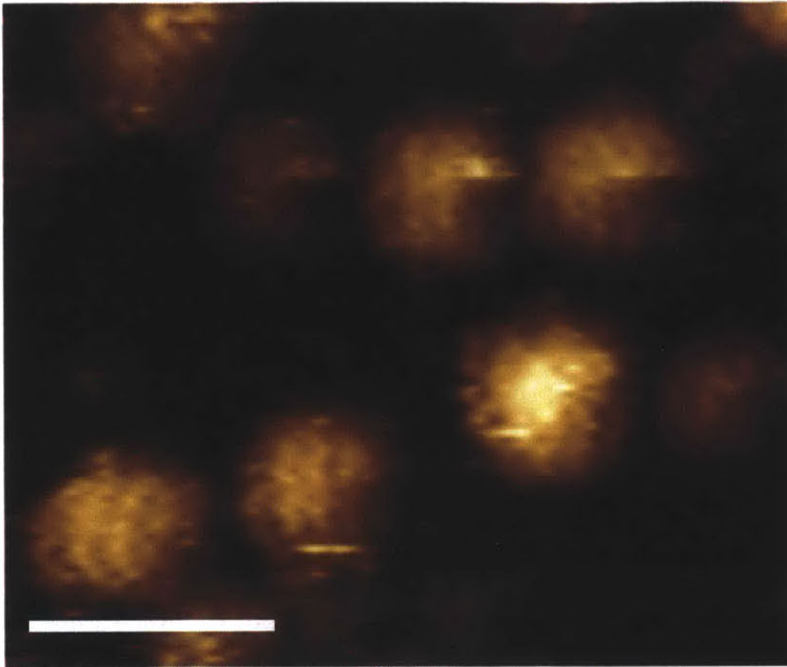


Figure 2.2. TGA curve for HT/EG2 gold nanoparticles prepared

STM can visualize the structure of a sample surface by detecting tunneling currents between a conductive sample and a metallic tip<sup>9</sup>. The tunneling current is varied as the metallic tip scans across the sample surface, attributing to the changes in the height of the surface or the chemical functionality. In other words, the ligand structure can be mapped with a feedback of the tunneling current. For this reason, STM is regarded as the most direct way to confirm the striped structure<sup>10-12</sup>. The

sample was prepared on gold mica substrate by ligand exchange. The gold mica was immersed in 5mM of 1-butanethiol solution overnight, followed by incubating in 5mM of 1,9-nonanedithiol solution for an hour for a ligand exchange. The gold mica was rinsed with ethanol sufficiently after each incubation step to remove free thiols. Finally, it was immersed in the striped nanoparticle solution overnight and rinsed with a copious amount of methanol and ethanol. The sample was stored in nitrogen-filled vial by the measurement. The typical STM image of the striped gold nanoparticles is shown in Figure 2.3 (The STM measurement was done by Dr. Miao Yu.). Only HT/EG2 gold nanoparticles were imaged via STM here, and it was assumed that gold nanoparticles with other ligand combinations, such as HT/EG1, HT/EG3 and OT/EG3 were striped. Due to their flexibility of EGN ligands, compared to the ligand consisting of only carbon chains, it was particularly tricky and hard to get a STM image; hence, we only focused on HT/EG2 nanoparticles. The STM experiments were performed at room temperature in air using a Veeco Multimode Scanning Probe Microscopy in an acoustic chamber sitting on a vibration damping table. Mechanically- cut platinum-iridium STM tips were used. All images were collected with a tunneling current of 25-100 pA and an applied bias of 800-1500 mV. The width of stripes was  $1.3 \pm 0.1$  nm.





**Figure 2.3.** A typical STM image of the striped gold nanoparticles (HT/EG2 nanoparticles for this image) (The scale bar is 10 nm.)

## **2.4. Solution based conductivity test**

### **2.4.1. Concept of conductivity**

The conductivity of an electrolyte solution is an index to measure its ability to conduct electricity. It is frequently used to determine the amount of ions in a solution in both industrial and engineering fields. The SI unit of the conductivity is siemens per meter (S/m), and  $\mu\text{S}/\text{cm}$  is often used. One siemens correspond to the reciprocal of one ohm, which can be easily understood, considering that the conductance is the reciprocal of resistance. The conductivity of an electrolyte

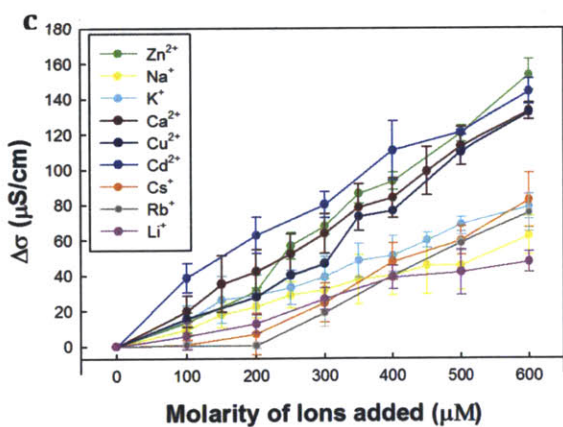
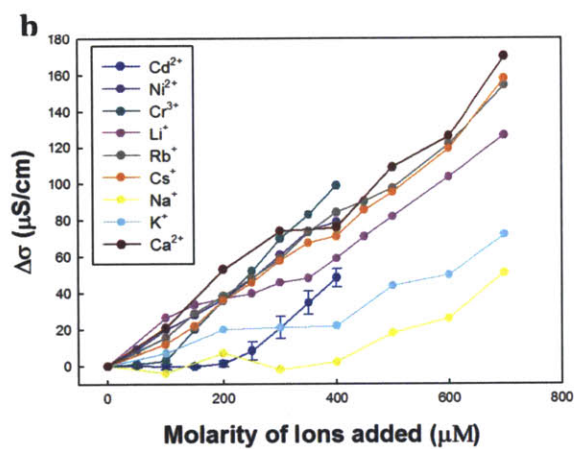
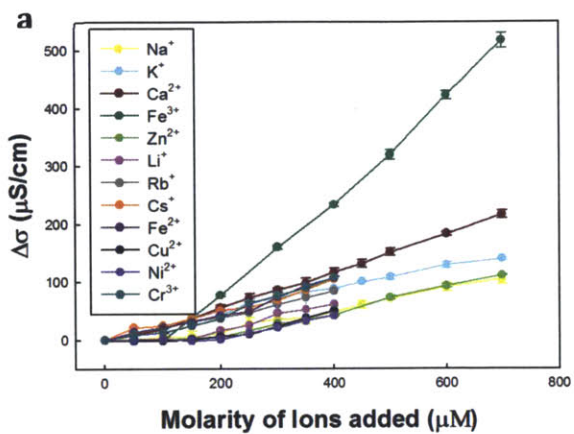
solution is determined by measuring the resistance of the solution using a conductivity meter, where two electrodes are separated by a fixed distance, commonly 1 cm<sup>13</sup>. Many kinds of conductivity meters are commercially available, also providing automatic temperature correction function.

In this work, basically the conductivity measurement gold nanoparticles in the aqueous solution is carried out to examine if the striped gold nanoparticles can make a complex with different kinds of metal ions, as crown ethers do. Generally, gold nanoparticles were dispersed in water (in the concentration of 1mg/2.5ml), and the change of conductivity was measured by adding the aliquot of a particular ion solution in each step, and chloride ions or bromide ions are used as counter-ions. The increase of conductivity was expected in the case of that gold nanoparticles were not able to capture the added metal ions, whereas a plateau region would be observed, where the conductivity would not increase upon the addition of the aliquots of metal ion solution, in the event of ion-trapping. Specifically, when gold nanoparticles capture a certain kind of ions, the added ions cannot contribute to the increase of conductivity, since they are stuck in ligand moieties of gold nanoparticles, which results in the plateau region on the plot of the conductivity. We expect that this plateau region would be observed until a stoichiometric point is reached. The stoichiometric point was estimated on the basis of the relative amount of EGn ligands, assuming that two EGn ligands would interact with one ion like crown ether. The amount of each aliquot was very small (in the unit of micro-liter), compared to that of gold nanoparticle solution (in the unit of

milliliter); hence, the aliquots themselves, without ions, do not affect the conductivity, that is, they do not dilute the solution. The results of conductivity test of various gold nanoparticles were shown in the following sections, and each measurement was done at least three times, leading to each plot by their average values with standard deviations, represented by error bars.

#### **2.4.2. HT/EGn striped nanoparticles**

In the beginning, one kind of metal ion was added in a certain kind of gold nanoparticle solution, and the conductivity was measured in each step. For example, the aliquot of KCl solution was added in the aqueous HT/EG2 gold nanoparticle solution, and the change of conductivity was investigated. The results of the conductivity test for three kinds of the striped nanoparticles with various metal ions are illustrated in Figure 2.4, and summarized in Table 2.1, where plus (+) sign indicates that there was an interaction between each nanoparticle and metal ion and minus (-) sign means that there was not.



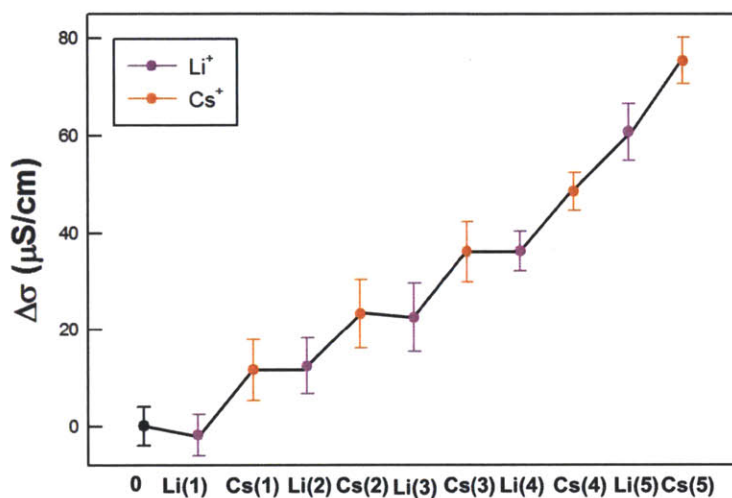
**Figure 2.4.** The conductivity test results of various kinds of metal ions with (a) HT/EG1 striped nanoparticles, (b) HT/EG2 striped nanoparticles, and (c) HT/EG3 striped nanoparticles; each measurement was done at least three times, leading to each plot by their average values with standard deviations, represented by error bars.

	HT/EG1 AuNP	HT/EG2 AuNP	HT/EG3 AuNP
Li	+	-	-
Na	+	+	-
K	-	+	-
Rb	-	-	+
Cs	-	-	+
Ca	-	-	-
Cu(II)	+		-
Fe(II)	-		-
Fe(III)	+		
Zn	+	-	-
Cr(III)	-	+	
Ni	+	-	-
Cd	-	+	-
CH <sub>3</sub> Hg	-	-	+

**Table 2.1.** Summary for ion-capturing effect: (+) means that each gold nanoparticle can capture each ion and (-) means that it cannot.

In addition, to prove that striped nanoparticles can selectively absorb specific ions, conductivity test were carried out with mixture of ions. Based on the above conductivity result, the HT/EG1 gold nanoparticles can capture lithium ions, but not cesium ions. The conductivity was measured by adding lithium and cesium ion solutions alternatively by 10  $\mu$ l of aliquot (Figure 2.5). When adding lithium ion solutions, the conductivity did not change, but when cesium ion solutions were added, the conductivity increased. This phenomenon continued until total 40  $\mu$ l of lithium ion solutions were added, which was the stoichiometric point of HT/EG1

nanoparticles and lithium ions pair, and this point is consistent with the result of Figure 2.4. With this result, it is shown that these striped gold nanoparticles can capture a certain ion selectively even in the presence of other ions.

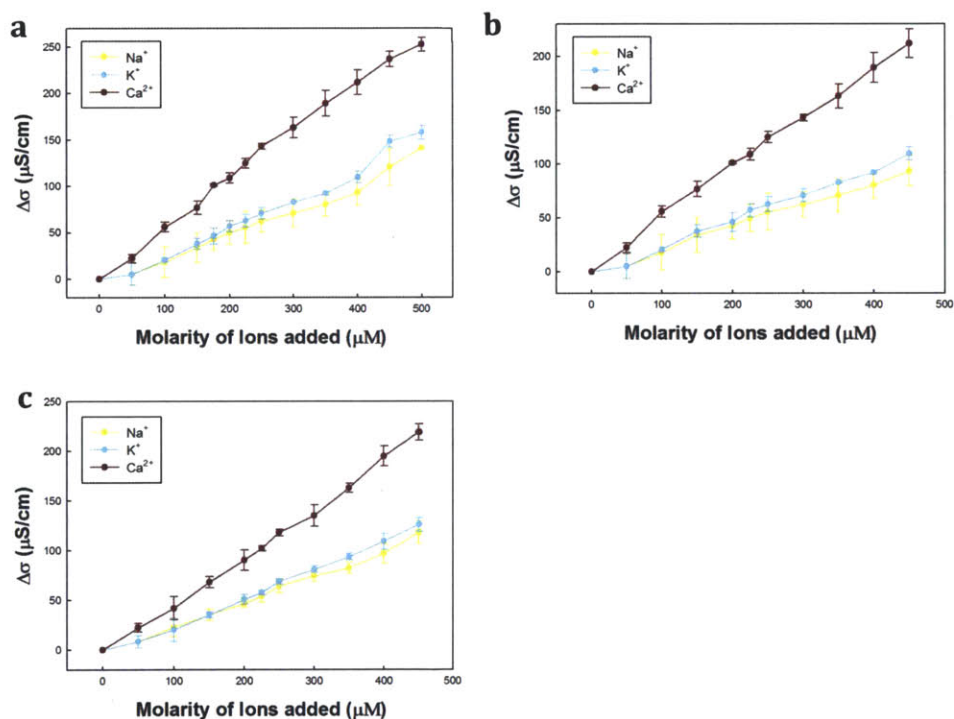


**Figure 2.5.** The conductivity test with HT/EG1 striped nanoparticles and the mixed ions (lithium and cesium ions): a black dot is the initial value before adding ion solutions, and each yellow dot represents the value after adding 10  $\mu\text{l}$  of lithium ion solution and each blue dot represents the value after adding 10  $\mu\text{l}$  of cesium ion solution; the measurement was done five three times, resulting in the plot by their average value with the standard deviation, represented by the error bar.

### 2.4.3. Homo-ligand and disordered structured nanoparticles

A couple of control experiments were required to support that this selective ion-capturing behavior is originated from the striped structure of mixed ligands on gold nanoparticle surface.

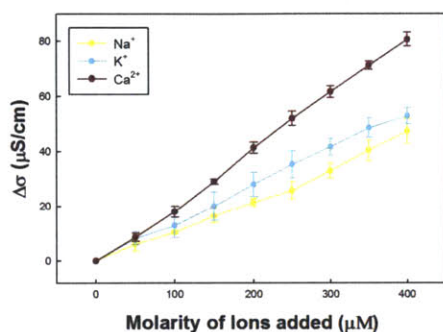
Firstly, gold nanoparticles coated with just homoligands were tested, i.e. gold nanoparticle with just EG1 ligand (call EG1 homo-nanoparticle), one with just EG2 ligand (call EG2 homo-nanoparticle), and one with just EG3 ligand (call EG3 homo-nanoparticle), using sodium, potassium and calcium ions (Figure 2.6). On the result, it was shown that the conductivity increased continuously by adding ion solutions, demonstrating that gold nanoparticles protected entirely by homoligands were not able to capture any those ions.



**Figure 2.6.** The result of conductivity test for (a) EG1 homo-nanoparticle, (b) EG2 homo-nanoparticle, and (c) EG3 homo-nanoparticle; each measurement was done at least three times, leading to each plot by their average values with standard deviations, represented by error bars.

Also, the disordered structure nanoparticles consisting of brHT and EG2 ligands

were tested, and the result of the conductivity test for brHT/EG2 gold nanoparticle was shown in Figure 2.7, and there was no binding effect for this disordered gold nanoparticles, whereas HT/EG2 gold nanoparticles can make a complex with sodium and potassium ions. This can be another indication that the ordered striped structure greatly contributes to the selective ion-capturing.



**Figure 2.7.** The result of the conductivity for gold nanoparticles with EG2 and brHT; each measurement was done at least three times, leading to each plot by their average values with standard deviations, represented by error bars.

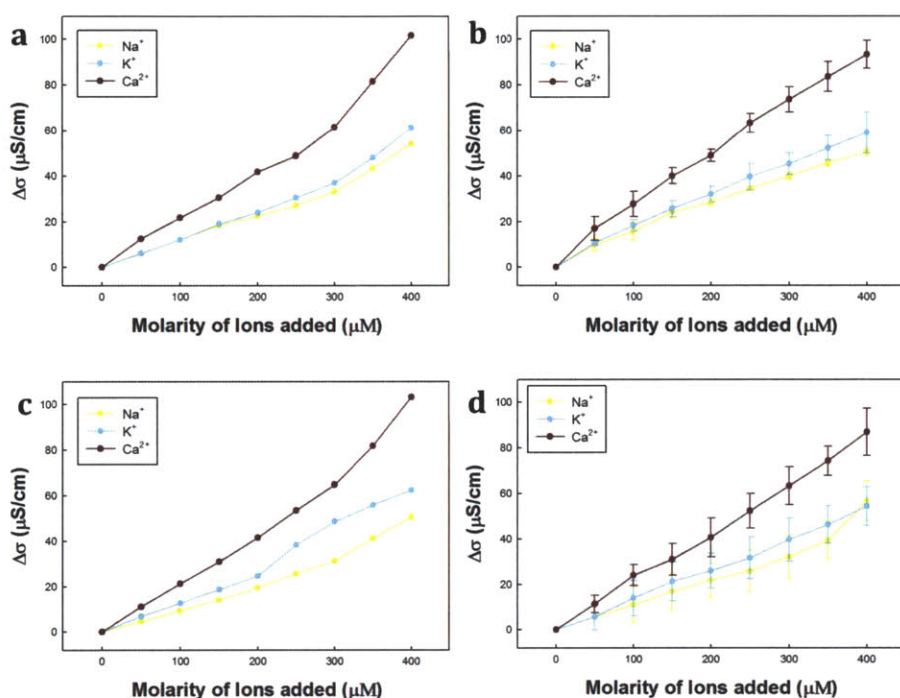
#### 2.4.4. Striped nanoparticles with other compositions

Based on the results of HT/EGn nanoparticles, it can be deduced that it would be possible to capture more different kinds of metal ions with different combination of ligands pairs on the striped nanoparticles. In this aspect, the hydrophobic ligand (i.e. HT) was replaced with other ligands to assess the ion-capturing behavior.

The gold nanoparticles with other spacing ligands, substituting HT, were also synthesized, and the conductivity test has been done to see the effect of this ligand



on the capturing ability. Mainly, two types of ligands were used, one with a hydrophilic head such as 6-mercapto-1-hexanol (MHO) and 6-amino-1-hexanethiol (AH), and the other with the same aliphatic hydrocarbon chains but in a slightly different length such as 1-octanethiol (OT) and 1-butanethiol (BT). The experiments with first group were done to check influence of the ligand property and that of the second group were done to demonstrate the effect of the length.



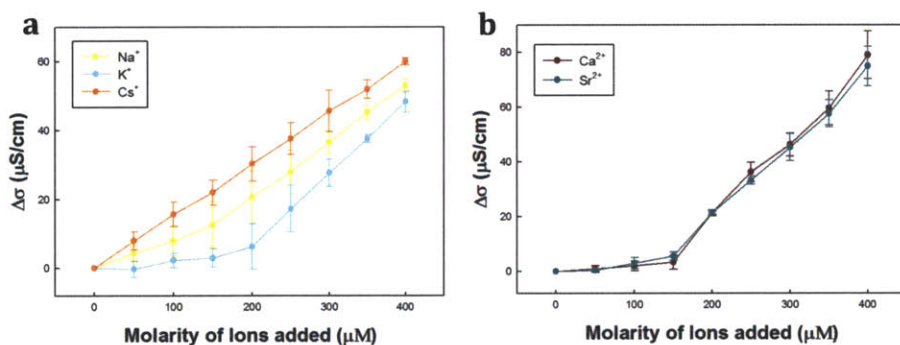
**Figure 2.8.** The results of conductivity test for gold nanoparticles consisting of EG2 and different spacing group (a) MHO, (b) AH, (c) OT, and (d) BT; each measurement was done at least three times, leading to each plot by their average values with standard deviations, represented by error bars.

Gold nanoparticles composed of each spacing group and EG2 ligand were synthesized and the conductivity tests were done, the results are shown in Figure 2.8. Remarkably, there was no capturing effect for all four gold nanoparticles, unlike

the fact that HT/EG2 gold nanoparticles can capture sodium and potassium ions.

This displays that the spacing group also plays a crucial role in forming the striped structure and capturing ions.

More interestingly, when OT pairs with EG3 ligands, it shows a distinguished effect (Figure 2.9). Gold nanoparticles with OT and EG3 ligands no longer captured cesium ions, as HT/EG3 gold nanoparticles did, but they are able to make a complex with potassium, calcium and strontium ions. It is noteworthy that any HT/EGn nanoparticles were not able to capture calcium ions, since this also presents the possibility that more diverse ions could be selectively captured by altering the ligand group in the striped nanoparticles.



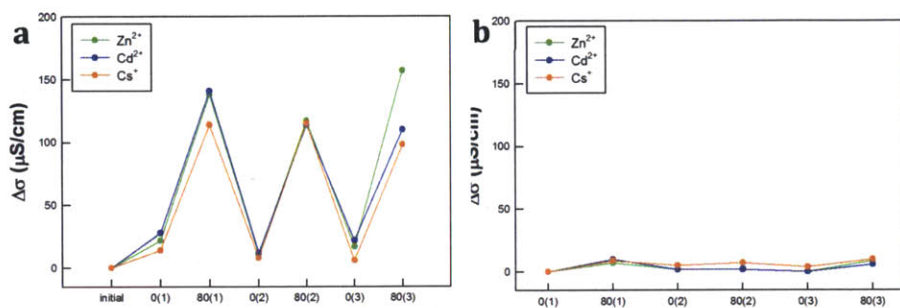
**Figure 2.9.** The results of conductivity test for OT/EG3 striped nanoparticles with (a)  $\text{Na}^+$ ,  $\text{K}^+$ ,  $\text{Cs}^+$  and (b)  $\text{Ca}^{2+}$ ,  $\text{Sr}^{2+}$ ; each measurement was done at least three times, leading to each plot by their average values with standard deviations, represented by error bars.

## 2.5. Release of captured-metal ions from gold nanoparticles

It is also important to release the captured ions from nanoparticles. The influence of temperature on the ion-capturing mechanism was examined to manipulate a method to release ions. The initial conductivity of each striped nanoparticle solution was measured, and then the stoichiometric amount of zinc, cadmium, cesium ions, which was deduced from the conductivity test in the previous section, was added into each HT/EG<sub>n</sub> nanoparticle solutions, i.e. zinc ions into HT/EG1 nanoparticles, cadmium ions to HT/EG2 nanoparticles, and cesium ions to HT/EG3 nanoparticles. Then, the solution was cooled down to 0 °C, and the conductivity was measured again. Moreover, the solution was also heated to 80 °C, and the conductivity was measured at room temperature in the same way. It is shown that the conductivity was increased when the temperature was raised to 80 °C, without further addition of ion solution, as shown in Figure 2.10(a). This means that the captured ions were released from the cavity of gold nanoparticles, induced by the increase of entropic contribution of ligands due to high temperature. This ion-releasing phenomenon by high temperature was also observed in crown ether<sup>14</sup>.

Furthermore, when the temperature was lowered to 0 °C, the conductivity was reduced again, indicating that the released ions have been captured again by gold nanoparticles. This procedure has been repeated three times, proving that the ion-capturing mechanism depends on temperature and it is also reversible. To demonstrate that this conductivity change was caused by the ion capturing and

releasing process, not just thermal effect<sup>15-17</sup>, the same test has been done without gold nanoparticles. In Figure 2.10(b), the conductivity slightly altered during the temperature-regulating procedure, but the amount of change is ignorable, compared to the result of the system with gold nanoparticles.



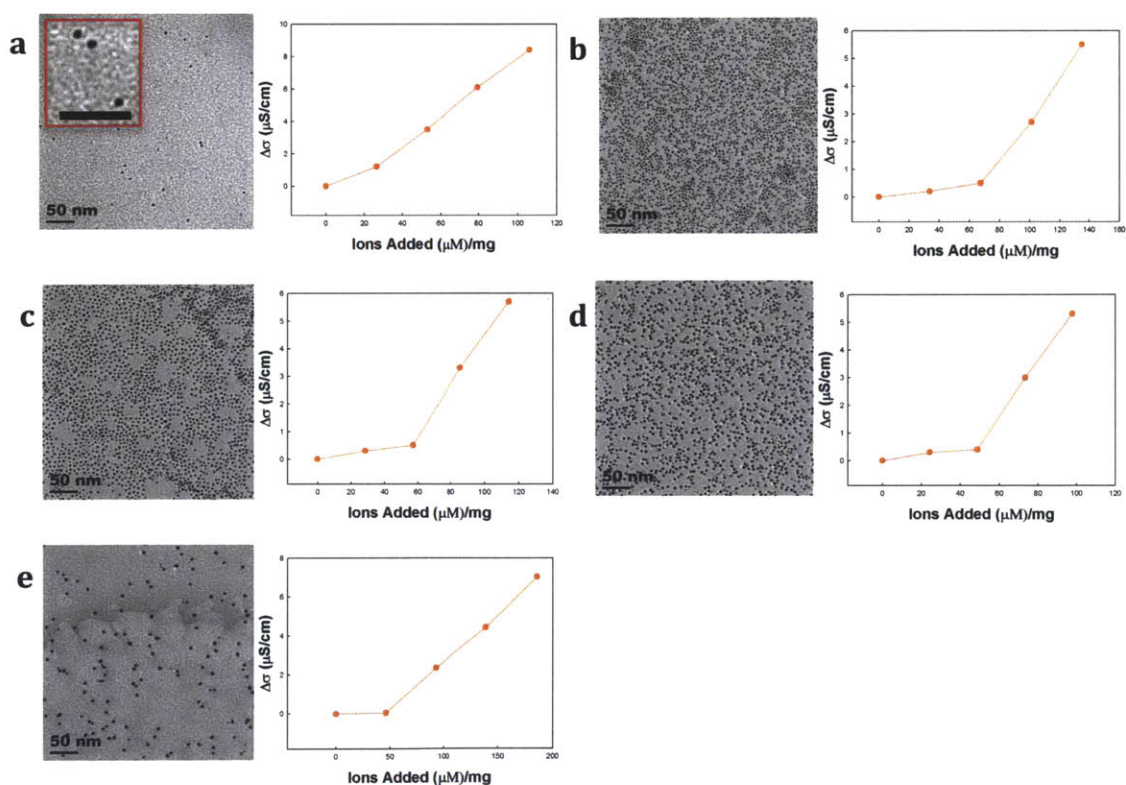
**Figure 2.10.** The change of the conductivity for (a)  $\text{Zn}^{2+}$  + HT/EG1 particles,  $\text{Cd}^{2+}$  + HT/EG2 particles,  $\text{Cs}^+$  + HT/EG3 particles and (b)  $\text{Zn}^{2+}$ ,  $\text{Cd}^{2+}$ ,  $\text{Cs}^+$  without gold nanoparticles

## 2.6. Ion-capturing dependence on the size of gold nanoparticles

Here, the effect of the size of the striped gold nanoparticles on ion-capturing was examined. In our previous study, it was demonstrated that the striped nanoparticles could be formed only within a certain size range of gold nanoparticles, which was predicted due to the curvature effect, as explained in Chapter 1<sup>18</sup>. In the similar context, the ion-trapping behavior was investigated with a different size of nanoparticles.

Recently, we proved that gold nanoparticles could be fractionated by their size via ultra-centrifuge<sup>19</sup>. The HT/EG3 gold nanoparticles were fractionated and divided

into five different batches, and each TEM image was shown in Figure 2.11. The mean diameter was calculated by counting at least 300 particles per batch, and it was distributed from 2.59 nm to 4.64 nm by approximately increasing 0.5 nm. The conductivity test was performed for each batch with Cs<sup>+</sup> ions, and the result was illustrated in Figure 2.11 with the corresponding TEM images. All bathes of particles were able to trap Cs<sup>+</sup> ions similarly, except the smallest one, which fell into the range of Janus particles according to our previous work. Janus particles can be interpreted as a half of EG3 homo-nanoparticles, and in such context this conductivity test result would be reasonable.



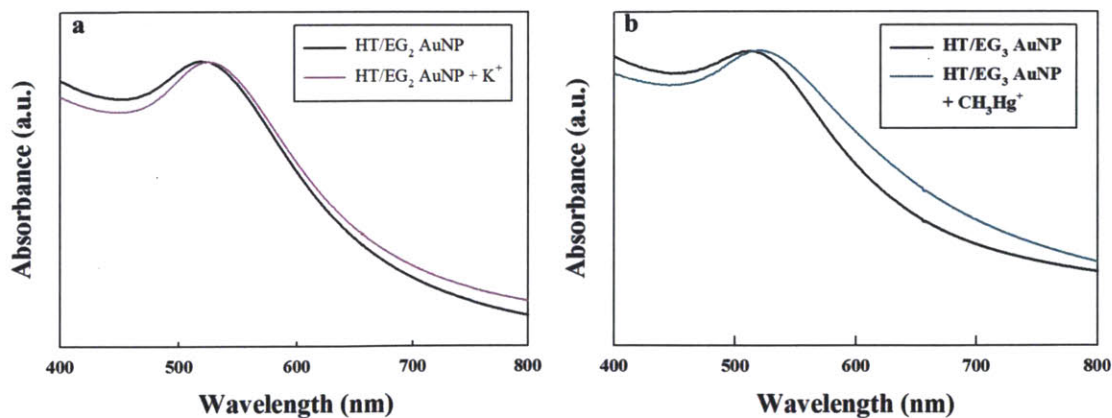
**Figure 2.11.** TEM images and conductivity test result for corresponding fractionated HT/EG3 striped particles with a mean diameter of (a)  $2.59 \pm 0.55$  nm (the scale bar of inset is 25 nm), (b)  $3.16 \pm 0.51$  nm, (c)  $3.72 \pm 0.62$  nm, (d)  $4.14 \pm 0.75$ , and (e)  $4.64 \pm 0.99$  nm; the amount of ions added was normalized so that it represents the ions per 1 mg of nanoparticles.

## 2.7. Characterization of the interaction between gold nanoparticles and metal ions

A series of spectroscopic measurements were performed to verify the interaction between the striped nanoparticles and metal ions, and the details of each experiment are introduced in each section.

### 2.7.1. Ultraviolet-visible spectroscopy (UV-vis)

UV-vis spectroscopy has been widely used to analyze metal nanoparticles since it is a very useful tool to evaluate the solubility of nanoparticles in a solution, and also the size and aggregation of nanoparticles<sup>20,21</sup>. Gold nanoparticle has its own plasmon resonance characteristic peak around 520 nm, and any other factors could affect the absorption spectrum.



**Figure 2.12.** UV-vis spectra of (a) HT/EG<sub>2</sub> nanoparticles before and after adding K<sup>+</sup> and (b) HT/EG<sub>3</sub> nanoparticles before and after adding methylmercury

Here, UV-vis measurement was conducted to quickly see the effect of metal ions captured on the absorption spectrum of nanoparticles. The nanoparticle samples were measured in aqueous solutions first, and a stoichiometric amount of the corresponding metal ions were added and stirred for a while, followed by the measurement (Figure 2.12). As shown in the spectra, the plasmon resonance peak for both striped nanoparticles was red-shifted on the addition of the ions, implying that each nanoparticle forms a complex with ions. For non-captured ions in nanoparticle solution, no shift in plasmon resonance peak was observed.

### **2.7.2. X-ray photoelectron spectroscopy (XPS)**

XPS is a typical spectroscopic technique for a quantitative surface analysis<sup>22</sup>. When irradiating X-ray onto a material, it can measure the kinetic energy and number of electrons escaping from the surface. From the obtained spectra, the information about elemental composition can be acquired. Here we used XPS for a quantitative analysis of the captured metal ions per gold nanoparticle.

Prior to the complex of gold nanoparticle and metal ions, the pure gold nanoparticles were analyzed. The amount of each element was obtained from XPS spectra, and the results were shown in Table 2.2. It was revealed that less sulfur was detected, which was caused by the fact that sulfur is very closed to the surface and shielded by outer elements; hence the actual sulfur amount assumed was adjusted

based on the quantities of other measured elements and the composition of molecules, as shown in Table 2.2.

Conc.at%	C 1s	O 1s	S 2p	Au 4f	Na 1s	Cl 2p	B 1s
HT/EG1 AuNP	39.25	7.1	5.23	12.25	10.2	28.1	1.7
HT/EG1 AuNP + Zn <sup>2+</sup>	58.55	19.7	1.95	14.9	0	0	1.37
HT/EG3 AuNP	44.55	14.8	4.24	13.15	6.55	17.65	2.9
HT/EG3 AuNP+ CH <sub>3</sub> Hg <sup>+</sup>	30.4	60.1	0.22	2.0	0.9	6.1	0.24

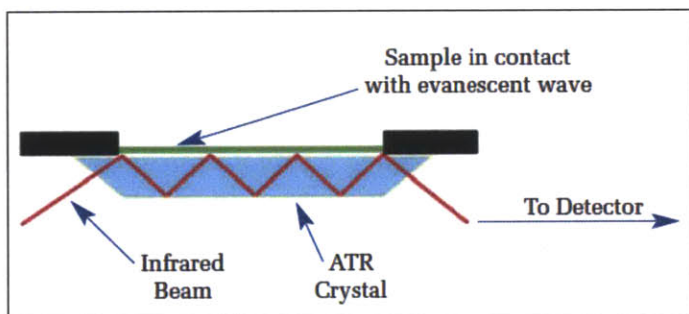
**Table 2.2.** XPS analysis for HT/EG1 particles without /with Zn<sup>2+</sup> and HT/EG3 particles without /with CH<sub>3</sub>Hg<sup>+</sup>

Firstly, HT/EG<sub>1</sub> gold nanoparticles capturing Zn<sup>2+</sup> ions were analyzed. The sufficient amount of ZnCl<sub>2</sub> was added into HT/EG<sub>1</sub> nanoparticle aqueous solution, and the solution was stirred for 30 min to make sure the formation of the complex of gold nanoparticles and Zn<sup>2+</sup> ions. The solution was washed with Millipore water three times by centrifuging to get rid of the un-captured free Zn<sup>2+</sup> ions. After the final run of centrifuge, the solid part was separated, and dried under the vacuum before analysis, and also the liquid part, i.e. water used for washing, was collected separately for analysis. Prior to the analysis of the solid part, the liquid part was analyzed via ion chromatography, and no Zn<sup>2+</sup> ions were found, which means that the un-captured free Zn<sup>2+</sup> ions were completely removed. The solid part, i.e. gold nanoparticles containing Zn<sup>2+</sup> ions, was analyzed with XPS. The sulfur amount was adjusted in the same way as for the pure nanoparticles, and the each elemental quantity is shown in Table 2.2. From the quantitative analysis, it was demonstrated that the ratio of EG<sub>1</sub> ligands to Zn<sup>2+</sup> ions was ~3.4, and we were able to deduce that one Zn<sup>2+</sup> ion was captured by every 3~4 EG<sub>1</sub> ligands, implying the formation of three- dimensional shape just like cryptand.



Secondly, HT/EG<sub>3</sub> gold nanoparticles capturing CH<sub>3</sub>Hg<sup>+</sup> were analyzed. The sample was prepared in a different way from the previous HT/EG<sub>1</sub> gold nanoparticles containing Zn<sup>2+</sup>, since the solubility of CH<sub>3</sub>HgCl in water is very low, whereas ZnCl<sub>2</sub> is highly soluble in water. HT/EG<sub>3</sub> gold nanoparticles were dispersed in water, mixing with CH<sub>3</sub>HgCl for a while. The un-captured CH<sub>3</sub>HgCl was separated from the resulting solution using 0.2 μm pore-size of syringe filter. The filtered solution was analyzed, and the result was shown in Table 2.2, after the adjustment. The ratio of EG<sub>3</sub> ligands to CH<sub>3</sub>Hg<sup>+</sup> was ~2, which means that one CH<sub>3</sub>Hg<sup>+</sup> was captured by every 2 EG<sub>3</sub> ligands, presumably forming crown ether shape.

### 2.7.3. Fourier transform infrared spectroscopy (FT-IR)



**Figure 2.13.** A schematic cartoon of FT-IR with ATR accessory (Taken from FT-IR spectroscopy technical note on [www.perkinelmer.com](http://www.perkinelmer.com))

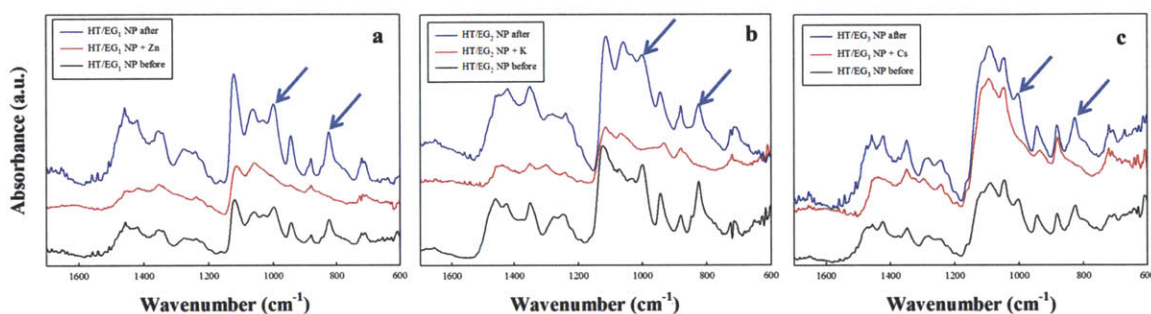
FT-IR is one of the most widely used methods with NMR to get information about organic materials<sup>23</sup>. In this work, the structure of ligand molecules, especially EG ligands, on the gold nanoparticle surface was interpreted via FT-IR measurement. Each striped gold nanoparticle was measured in the powder, using ATR (Attenuated Total Reflectance) accessory, which enables the monitoring of the sample in-situ<sup>24,25</sup>.

Specifically, the infrared beam is directed onto a crystal, where a totally internal reflection occurs, and changed upon contacting with a sample (gold nanoparticle in our experiment). The altered beam exits the other end of the crystal and comes to the detector (Figure 2.13). In this case, a direct contact with ATR crystal is required for a sample.

The pure gold nanoparticles were measured first, and they were collected, followed by the complexation with the corresponding metal ions. The ion-captured nanoparticles were prepared in the same way with XPS samples described in the previous section. The resulting spectra are shown in Figure 2.14.

Firstly, the alkyl chains are in all trans-crystalline states, suggested by the peaks at  $2918\text{ cm}^{-1}$  (asymmetric alkyl CH stretching) and  $2851\text{ cm}^{-1}$  (symmetric alkyl CH stretching)<sup>26,27</sup>. Some samples tended to show the peaks in a slightly lower or higher wavenumber region than  $2918\text{ cm}^{-1}$ , which indicated the highest degree of crystallinity or a slightly higher gauche content. Furthermore, EG parts are in the helix structure, indicated by the peaks at  $1458\text{ cm}^{-1}$  for  $\text{CH}_2$  scissoring,  $1349\text{ cm}^{-1}$  for  $\text{CH}_2$  wagging,  $1247\text{ cm}^{-1}$  for  $\text{CH}_2$  twisting, and  $1116\text{ cm}^{-1}$  for the strong skeletal -C-O-C- stretching, which is caused by the alternating trans and gauche structure; -O-C-C-O- prefers trans-gauche-trans conformation<sup>26</sup>. However, interestingly this kind of helix structure was not shown with shorter EG ligands in the literature<sup>26</sup>. According to the literature, for instance, EG2 and EG4 parts have trans-states like alkyl chains when they form SAM on a flat gold surface, whereas EG6 display a helix structure.

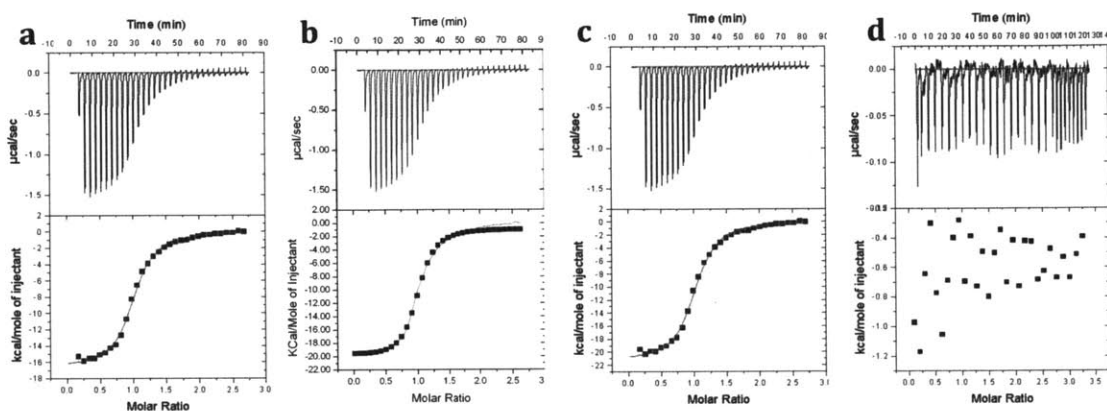
However, in the striped particles, the spectra indicate the presence of an oriented and crystalline, helical EG phase. In addition, according to the literature, it is said that this helical phase is disturbed at high temperature (approximately 60 °C~70 °C), and the helical structure turns into amorphous phase<sup>26</sup>. It was assumed that our ion-releasing effect observed at 80 °C was related to this conformational change.



**Figure 2.14.** FT-IR spectra for (a) HT/EG1 particles, (b) HT/EG2 particles, and (c) HT/EG3 particles: the black plot for each nanoparticle as synthesized, the red plot for the complex of each nanoparticle and the corresponding ion, and the blue plot for each nanoparticle after releasing the captured ions

Generally, the peaks from 1500  $\text{cm}^{-1}$  to 750  $\text{cm}^{-1}$  were attributed to the motions of -C-C- and -C-O-, and it was shown that two major peaks disappeared after the complexation with metal ions, indicating that there was a change in the motions of two bonds as a result of ion-binding by ethylene glycol groups. Also, all peaks were recovered to the original state after the captured ions were released by putting them in hot water, and this verified that the ligand structure was restored and the ion-capturing and releasing process would be reversible.

## 2.7.4. Isothermal titration calorimetry (ITC)



**Figure 2.15.** ITC results for (a) HT/EG2 particles with  $K^+$ :  $N=0.9974$ ,  $K=1.508 \times 10^6 (\pm 1.2 \times 10^5)$ ,  $\Delta H = -69.846$  kJ/mol,  $\Delta S = -118.902$  J/mol $\cdot$ K, (b) HT/EG2 particles with  $Cd^{2+}$ :  $N=0.982$ ,  $K=2.75 \times 10^6 (\pm 3.09 \times 10^5)$ ,  $\Delta H = -83.916$  kJ/mol,  $\Delta S = -161.7$  J/mol $\cdot$ K, (c) HT/EG3 particles with  $Cs^+$ :  $N=1.007$ ,  $K=1.933 \times 10^6 (\pm 1.56 \times 10^5)$ ,  $\Delta H = -89.586$  kJ/mol,  $\Delta S = -183.834$  J/mol $\cdot$ K, and (d) HT/EG3 particles with  $K^+$ : No particular change was observed; the standard deviation of the bonding constants was calculated in the process of fitting with the collected values under conditions that optimize precision<sup>28</sup>.

Calorimetric techniques such as differential scanning calorimetry (DSC) and isothermal titration calorimetry (ITC) have been a powerful tool to get thermo-analytical data. While DSC measures the difference of heat needed to increase the temperature of a sample with a well-known heat capacity of a reference, ITC measures the heat change of a reaction at a constant temperature. In ITC experiment, the reaction is generated by titrating the reactant into the sample cell, and the heat change (exothermic or endothermic) induced by the reaction between the injected reactant and the sample solution is monitored from the beginning of the

experiment<sup>29</sup>. ITC makes it possible to directly characterize thermodynamic parameters, such as  $\Delta H$ ,  $\Delta S$ ,  $\Delta G$ , and  $K$ , and the stoichiometric ratio of two reactants in the formation of the complex with a high sensitivity in a single experiment<sup>30-32</sup>.

In this work, ITC measurement was used to obtain the thermodynamic parameters in ion-capturing and also the stoichiometric ratio of each EG ligand and metal ions. The striped nanoparticle aqueous solution was placed in the sample cell, and each metal ion solution was injected into the cell 20~30 times. The results were illustrated in Figure 2.15, and as expected, all measurement showed a negative entropy change. For HT/EG2 striped particles, the binding constants with  $K^+$  and  $Cd^{2+}$  were similar, although they presented a slightly higher affinity with  $Cd^{2+}$ . Moreover, there was little heat change for HT/EG3 particles with  $K^+$ , and such a very small amount of heat could be induced by the dilution when the ion solution was injected to the sample cell.

#### **2.7.5. Zeta potential ( $\zeta$ -potential)**

$\zeta$ -potential is a standard to judge the stability in colloidal system, referring to electrokinetic potential<sup>33,34</sup>. It represents an electric charge in the interfacial double layer. Typically it is said that nanoparticles with  $\zeta$ -potential value greater than 25 mV or less than -25 mV stay stable in solution due to an electrostatic repulsion. When  $\zeta$ -potential value is low, attractive force prevails repulsion, and particles would be aggregated. Unmodified metal particles tend to have a negative charge in

the solution, and  $\zeta$ -potential value is varied, depending on capping ligands. With a neutral ligand, the surface charge is shielded, which leads to the lower  $\zeta$ -potential, like our nanoparticles.

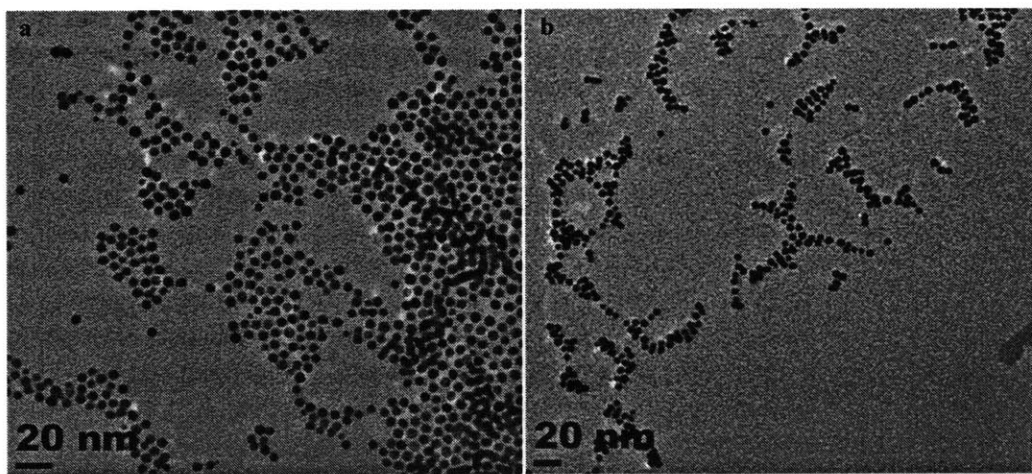
	HT/EG <sub>2</sub> NP	HT/EG <sub>2</sub> NP + Na	HT/EG <sub>2</sub> NP + K	HT/EG <sub>2</sub> NP + Cs
1	-33.44	-28.93	-21.44	-31.55
2	-35.60	-28.25	-17.21	-33.02
3	-34.07	-29.80	-20.31	-32.34
4	-34.95	-28.04	-17.44	-33.31
5	-33.25	-28.85	-18.6	-28.96
6	-32.46	-29.95	-18.28	-33.01
7	-32.15	-31.49	-20.78	-32.02
8	-32.68	-28.49	-19.30	-34.04
avg	-33.58±1.22	-29.23±1.14	-19.17±1.56	-32.28±1.55

**Table 2.3.** Change of zeta potential of HT/EG<sub>2</sub> striped nanoparticles in the presence of various metal ions

Here  $\zeta$ -potential was used to indirectly determine the interaction between the striped nanoparticles and metal ions. It was anticipated that the value of  $\zeta$ -potential would be invariable when there is no interaction between the nanoparticles and metal ions, while it would be changing when the nanoparticles captured metal ions. The gold nanoparticle samples for  $\zeta$ -potential measurement were prepared in Millipore water, and the stoichiometric amount of each metal ion was added into the solution. The measurement was performed in a high-precision mode, where the average value of total measurements (8 measurements here) was obtained. Table

2.3 presents the results of  $\zeta$ -potential measurement for the striped HT/EG<sub>2</sub> nanoparticles with three different kinds of metal ions (Na<sup>+</sup>, K<sup>+</sup>, and Cs<sup>+</sup>). The value of  $\zeta$ -potential for the nanoparticles themselves was approximately -33.58 mV, which could be classified as a stable state, and it was changed to less negative with the binding ion (K<sup>+</sup>), compared to the values with the non-binding ions (Na<sup>+</sup> and Cs<sup>+</sup>). This implied that there was a significant interaction between nanoparticles and K<sup>+</sup>, whereas Na<sup>+</sup> and Cs<sup>+</sup> were not. In the conductivity test, HT/EG<sub>2</sub> striped particles showed an affinity for Na<sup>+</sup>, although it was weaker than that for K<sup>+</sup>. This was also consistent with  $\zeta$ -potential result, which exhibited a small change with Na<sup>+</sup>, whereas it rarely changed with Cs<sup>+</sup>.

#### 2.7.6. Transmission electron microscope (TEM)



**Figure 2.16.** TEM images for (a) HT/EG<sub>2</sub> nanoparticles without K<sup>+</sup> and (b) HT/EG<sub>2</sub> nanoparticles with K<sup>+</sup>

TEM images were taken for the striped nanoparticles with and without metal ions. HT/EG2 gold nanoparticles were dispersed in water, obtaining the sample without potassium firstly, and the stoichiometric amount of potassium salt was added into the solution, stirring for 30 minutes. The second sample was acquired, and TEM sample was prepared as described in the previous section. The images were shown in Figure 2.16. The average diameter before K<sup>+</sup>-binding was 4.770±0.863 nm and that after K<sup>+</sup>-binding was 4.715±0.950 nm. From these results, it was verified that there was no remarkable change in nanoparticle morphologies.

## 2.8. References

- 1 Turkevich, J., Stevenson, P. C. & Hillier, J. A Study of the Nucleation and Growth Processes in the Synthesis of Colloidal Gold. *Discuss Faraday Soc*, 55- & (1951).
- 2 Brust, M., Walker, M., Bethell, D., Schiffrin, D. J. & Whyman, R. Synthesis of Thiol-Derivatized Gold Nanoparticles in a 2-Phase Liquid-Liquid System. *J Chem Soc Chem Comm*, 801-802, doi:Doi 10.1039/C39940000801 (1994).
- 3 Yee, C. K. *et al.* Novel one-phase synthesis of thiol-functionalized gold, palladium, and iridium nanoparticles using superhydride. *Langmuir* **15**, 3486-3491, doi:Doi 10.1021/La990015e (1999).
- 4 Kang, S. Y. & Kim, K. Comparative study of dodecanethiol-derivatized silver nanoparticles prepared in one-phase and two-phase systems. *Langmuir* **14**, 226-230, doi:Doi 10.1021/La970696i (1998).
- 5 Kimling, J. *et al.* Turkevich method for gold nanoparticle synthesis revisited. *J Phys Chem B* **110**, 15700-15707, doi:Doi 10.1021/Jp061667w (2006).
- 6 Zheng, N., Fan, J. & Stucky, G. D. One-step one-phase synthesis of monodisperse noble-metallic nanoparticles and their colloidal crystals. *Journal of the American Chemical Society* **128**, 6550-6551, doi:Doi 10.1021/Ja0604717 (2006).
- 7 Verma, A. *et al.* Surface-structure-regulated cell-membrane penetration by monolayer-protected nanoparticles. *Nat Mater* **7**, 588-595, doi:Doi 10.1038/Nmat2202 (2008).
- 8 Tien, J., Terfort, A. & Whitesides, G. M. Microfabrication through electrostatic self-assembly. *Langmuir* **13**, 5349-5355, doi:Doi 10.1021/La970454i (1997).
- 9 Binnig, G. & Rohrer, H. Scanning Tunneling Microscopy. *Ibm J Res Dev* **30**, 355-369 (1986).



- 10 Jackson, A. M., Myerson, J. W. & Stellacci, F. Spontaneous assembly of subnanometre-ordered domains in the ligand shell of monolayer-protected nanoparticles. *Nat Mater* **3**, 330-336, doi:10.1038/nmat1116 (2004).
- 11 Jackson, A. M., Hu, Y., Silva, P. J. & Stellacci, F. From homoligand- to mixed-ligand-monolayer-protected metal nanoparticles: A scanning tunneling microscopy investigation. *Journal of the American Chemical Society* **128**, 11135-11149, doi:Doi 10.1021/Ja061545h (2006).
- 12 Centrone, A., Hu, Y., Jackson, A. M., Zerbi, G. & Stellacci, F. Phase separation on mixed-monolayer-protected metal nanoparticles: A study by infrared spectroscopy and scanning tunneling microscopy. *Small* **3**, 814-817, doi:Doi 10.1002/Sml.200600736 (2007).
- 13 Bockris, J. O. M., Reddy, A. K. N. & Gamboa-Aldeco, M. E. *Modern electrochemistry*. 2nd edn, (Plenum Press, 1998).
- 14 Warshawsky, A. & Kahana, N. Temperature-Regulated Release of Alkali-Metal Salts from Novel Polymeric Crown Ether Complexes. *Journal of the American Chemical Society* **104**, 2663-2664, doi:Doi 10.1021/Ja00373a067 (1982).
- 15 Petrowsky, M. & Frech, R. Temperature Dependence of Ion Transport: The Compensated Arrhenius Equation. *J Phys Chem B* **113**, 5996-6000, doi:Doi 10.1021/Jp810095g (2009).
- 16 Lintner, W. *The effect of temperature on the electrical conductivity of organic liquids*, Massachusetts Institute of Technology, (1953).
- 17 Jones, H. C. *The electrical conductivity, dissociation, and temperature coefficients of conductivity from zero to sixty-five degrees, of aqueous solutions of a number of salts and organic acids*. (Carnegie Institution of Washington, 1912).
- 18 Carney, R. P. *et al.* Size limitations for the formation of ordered striped nanoparticles. *Journal of the American Chemical Society* **130**, 798+, doi:Doi 10.1021/Ja077383m (2008).
- 19 Carney, R. P. *et al.* Determination of nanoparticle size distribution together with density or molecular weight by 2D analytical ultracentrifugation. *Nat Commun* **2**, doi:Artn 335  
Doi 10.1038/Ncomms1338 (2011).
- 20 Daniel, M. C. & Astruc, D. Gold nanoparticles: Assembly, supramolecular chemistry, quantum-size-related properties, and applications toward biology, catalysis, and nanotechnology. *Chem Rev* **104**, 293-346, doi:Doi 10.1021/Cr030698+ (2004).
- 21 Centrone, A. *et al.* The role of nanostructure in the wetting behavior of mixed-monolayer-protected metal nanoparticles. *P Natl Acad Sci USA* **105**, 9886-9891, doi:Doi 10.1073/Pnas.0803929105 (2008).
- 22 Hüfner, S. *Photoelectron spectroscopy : principles and applications*. 3rd edn, (Springer, 2003).
- 23 Badia, A., Cuccia, L., Demers, L., Morin, F. & Lennox, R. B. Structure and dynamics in alkanethiolate monolayers self-assembled on gold nanoparticles: A DSC, FT-IR, and deuterium NMR study. *Journal of the American Chemical Society* **119**, 2682-2692, doi:Doi 10.1021/Ja963571t (1997).

- 24 Urban, M. W. *Attenuated total reflectance spectroscopy of polymers : theory and practice*. (American Chemical Society, 1996).
- 25 Greener, J., Abbasi, B. & Kumacheva, E. Attenuated total reflection Fourier transform infrared spectroscopy for on-chip monitoring of solute concentrations. *Lab Chip* **10**, 1561-1566, doi:Doi 10.1039/C001889a (2010).
- 26 Valiokas, R., Svedhem, S., Ostblom, M., Svensson, S. C. T. & Liedberg, B. Influence of specific intermolecular interactions on the self-assembly and phase behavior of oligo(ethylene glycol)-terminated alkanethiolates on gold. *J Phys Chem B* **105**, 5459-5469, doi:Doi 10.1021/Jp004441g (2001).
- 27 Harder, P., Grunze, M., Dahint, R., Whitesides, G. M. & Laibinis, P. E. Molecular conformation in oligo(ethylene glycol)-terminated self-assembled monolayers on gold and silver surfaces determines their ability to resist protein adsorption. *J Phys Chem B* **102**, 426-436, doi:Doi 10.1021/Jp972635z (1998).
- 28 Tellinghuisen, J. Optimizing experimental parameters in isothermal titration calorimetry. *J Phys Chem B* **109**, 20027-20035, doi:Doi 10.1021/Jp053550y (2005).
- 29 Wiseman, T., Williston, S., Brandts, J. F. & Lin, L. N. Rapid Measurement of Binding Constants and Heats of Binding Using a New Titration Calorimeter. *Anal Biochem* **179**, 131-137, doi:Doi 10.1016/0003-2697(89)90213-3 (1989).
- 30 Eichenbaum, G. M. *et al.* Alkali earth metal binding properties of ionic microgels. *Macromolecules* **33**, 4087-4093, doi:Doi 10.1021/Ma9917139 (2000).
- 31 Dam, T. K. & Brewer, C. F. Thermodynamic studies of lectin-carbohydrate interactions by isothermal titration calorimetry. *Chem Rev* **102**, 387-429, doi:Doi 10.1021/Cr000401x (2002).
- 32 Arnaud, A. & Bouteiller, L. Isothermal titration calorimetry of supramolecular polymers. *Langmuir* **20**, 6858-6863, doi:Doi 10.1021/La049365d (2004).
- 33 Lyklema, J. & Leeuwen, H. P. v. *Fundamentals of interface and colloid science*. (Academic Press, 1991).
- 34 Hunter, R. J. *Zeta potential in colloid science : principles and applications*. (Academic Press, 1981).

### **3. Metal-Ion Sensor Using Striped Gold Nanoparticles**

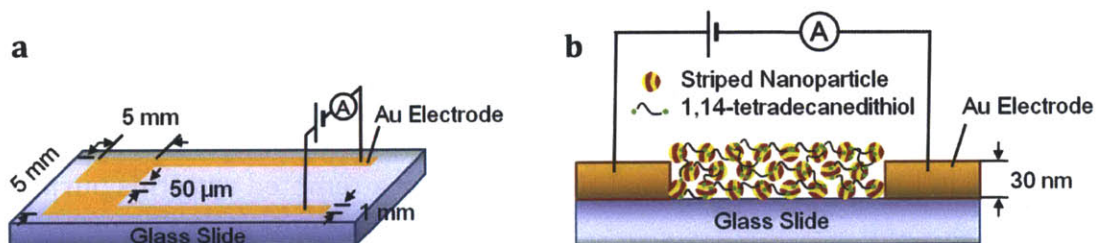
#### **3.1. Introduction**

It is very critical to detect the amount of toxic metal ions in an extremely low limit in water or other environmental samples, considering that they could induce a lethal effect with a fairly small quantity due to their bioaccumulative property<sup>1-3</sup>, as described in Chapter 1. Various methods have been attempted with this purpose, which includes spectroscopic methods such as atomic absorption spectroscopy (AA)<sup>4,5</sup> and inductively coupled plasma spectroscopy (ICP)<sup>6,7</sup>, optical methods such as colorimetric<sup>8,9</sup> or fluorescence-based assay<sup>10,11</sup> and systems based on surface plasmon resonance<sup>12,13</sup> or surface-enhanced Raman scattering<sup>14,15</sup>, and electrochemical methods<sup>16,17</sup>. However, most of these methods require a complicated chemistry, using a sophisticated macrocyclic molecule for selectivity, or elaborate measurement procedure. Particularly, only several methods have been reported for methylmercury in a very low detection limit, due to a lack of an appropriate material that can capture it.

Based on the results of Chapter 2, we exploited a solid-state metal ion sensor, using striped gold nanoparticles. The sensor device was obtained by depositing striped nanoparticles between electrodes, and the conductance change of gold nanoparticle film was measured upon the exposure to metal ions. The supramolecular pockets in the striped nanoparticles enable the selective ion-capturing, and this makes the

conductance of the film of nanoparticles changes noticeably by comprising an enhanced conductive paths. The details are discussed in the following sections.

### 3.2. Preparation of metal-ion sensor



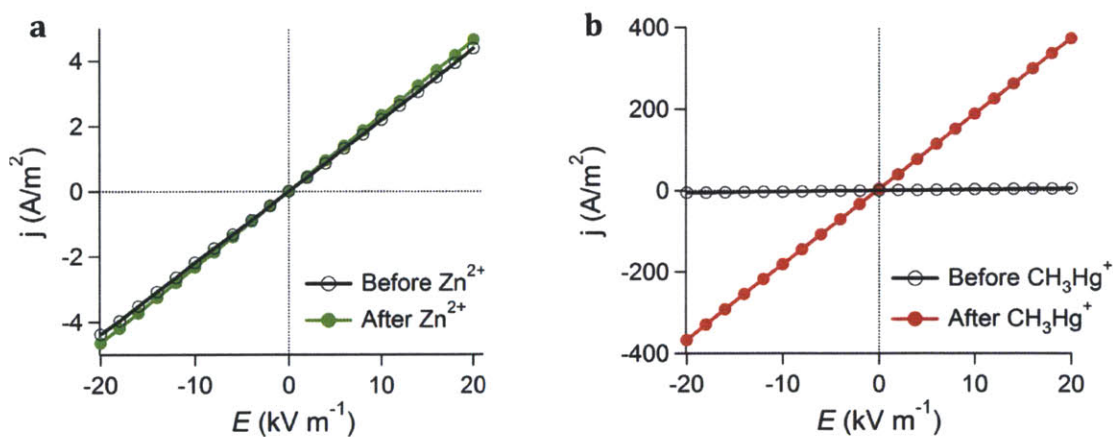
**Figure 3.1.** (a) The cartoon of the scheme and dimension of the sensor device and (b) side view of the film of the gold nanoparticle

The striped gold nanoparticles were prepared as depicted in Chapter 2, using the modified Stucky method, and dispersed in methanol (in a concentration of 2 mM of gold atoms). To fabricate the sensor device, gold electrodes with 30 nm-thickness and 5 mm-length were sputtered onto a glass substrate using a shadow mask, and the typical gap between two electrodes was 50 μm wide and 5 mm long. A 3 μl of gold nanoparticle solution was drop-casted onto the substrate and dried for 2 days under the vacuum, followed by a cross-linking step of gold nanoparticles to prevent them from dissolving out in water. The cross-linking was performed by dipping the film into a 5 mM of 1,14-tetradecanedithiol solution in toluene for 40 minutes, and rinsed with a copious amount of toluene, dried in vacuum for 2 days. These steps resulted in a 150 nm-thick nanoparticle film approximately, which was determined

by profilometry, and the number of gold nanoparticles between two electrodes was roughly in the order of  $10^{11}$ . The schematic cartoon of the sensor is shown in Figure 3.1.

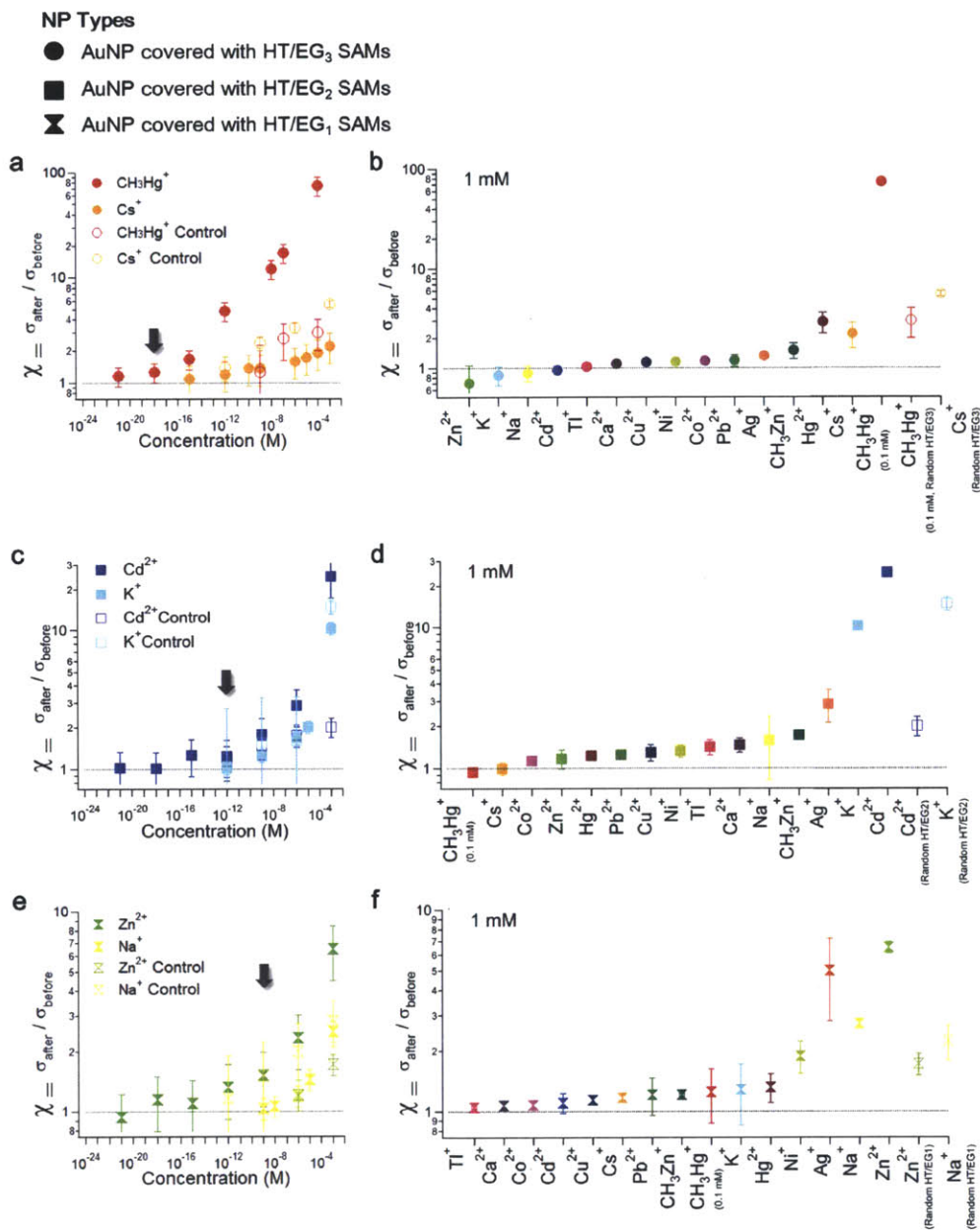
### 3.3. Measurement of conductance of gold nanoparticle films

The prepared electrodes were connected to an electrometer with high precision (Keithley 6517) placed in a home-made Faraday cage to measure the conductance of the film, and the measurements were conducted at room temperature. The films were immersed in 2 ml of metal ion solutions (chloride counter-ions) in Millipore water for 2 minutes, ranging from 1mM to 1zM to measure the detection limit. The films were sufficiently washed with Millipore water after immersion so that the free ions could be completely removed, and then dried under nitrogen environment.



**Figure 3.2.** The  $j$ - $E$  dependence for the film of the striped HT/EG3 nanoparticles before exposure to ions (black circles) and after exposure to ions (colored circles): (a) in a solution of Zn<sup>2+</sup> and (b) in a solution of CH<sub>3</sub>Hg<sup>+</sup>

The current density ( $j$ ) was measured by changing the applied field ( $E$ ) within a range of  $-20 \text{ kVm}^{-1}$  to  $20 \text{ kVm}^{-1}$  for all kinds of nanoparticle films and ions, and the  $j$ - $E$  dependence in the given range was ohmic. Prior to dipping into the ion solutions, the conductivities of the striped gold nanoparticle films ( $\sigma_{\text{before}}$ ) were  $\sim 2 \times 10^{-4} \Omega^{-1}\text{m}^{-1}$ . This is close to the value previously reported for a film of gold nanoparticles protected with thiolate with a similar thickness. The conductivities of the striped nanoparticle films upon the exposure to metal ion solutions ( $\sigma_{\text{after}}$ ) were measured. The conductivity increased when a certain kind of metal ions were captured by gold nanoparticles, whereas it did not change when the ions were not captured. For example, when the film of the striped HT/EG<sub>3</sub> gold nanoparticles was exposed to  $\text{Zn}^{2+}$ , there was no noticeable change of conductivity; however, it changed significantly when exposed to  $\text{CH}_3\text{Hg}^+$ , as shown in Figure 3.2. The change of the conductivity for three kinds of the striped gold nanoparticles on the exposure to various metal ions was measured, indicated as the ratio of the conductivities of the nanoparticle film ( $\chi = \sigma_{\text{after}} / \sigma_{\text{before}}$ ), and also the detection limits were evaluated for interactive pair of nanoparticle and ions, as summarized in Figure 3.3. The conductance change was measured in the decrement of concentrations until the ratio of the conductivities was close to the unity, and the detection limit was determined via two sample  $t$ -test with  $\chi$  values of two different concentrations at 99% confidence level, as described in Appendix.



**Figure 3.3.** The change in conductance for the films of gold nanoparticles upon the exposure to various metal ions; the sensitivity and selectivity were illustrated.

### 3.3.1. The films of the striped gold nanoparticles

Firstly, the film of the striped HT/EG<sub>3</sub> gold nanoparticles were tested, which made a

complex with  $\text{Cs}^+$  and  $\text{CH}_3\text{Hg}^+$  in the earlier result of Chapter 2. Upon the exposure to a variety of metal ions, it exhibited a significant conductance change with  $\text{CH}_3\text{Hg}^+$  and also with  $\text{Cs}^+$  and  $\text{Hg}^{2+}$ , as consistent with the solution-based conductivity test in Chapter 2. Remarkably, the HT/EG3 striped particles were able to detect  $\text{CH}_3\text{Hg}^+$  by an atto-molar ( $10^{-18}$  M) unit, and this corresponds to  $\sim 600$   $\text{CH}_3\text{Hg}^+$  ions in 1 ml of solution. The  $\chi$  value increased as the concentration of  $\text{CH}_3\text{Hg}^+$  was increasing, and it attained  $\sim 75$  at 0.1 mM of  $\text{CH}_3\text{Hg}^+$ . Additionally, the detection limit of  $\text{Cs}^+$  was 0.1  $\mu\text{M}$  (Figure 3.3(a) and (b)). The film of HT/EG2 striped nanoparticles also displayed a notable conductance change with  $\text{Cd}^{2+}$  and  $\text{K}^+$ . Specifically, it detected  $\text{Cd}^{2+}$  up to 1 pM and showed  $\chi=24.7$  at 1mM. Also, it was able to detect  $\text{K}^+$  with  $\chi=10.2$  at 1mM and with 1 pM limit, and it detected  $\text{Ag}^+$  with  $\chi=2.86$  at 1mM. However, it did not noticeably bind other kinds of ions as shown in Figure 3.3(c) and (d). Finally, it was revealed that the film of HT/EG1 striped nanoparticles detected  $\text{Zn}^{2+}$  with  $\chi=6.51$ ,  $\text{Na}^+$  with  $\chi=2.72$ , and  $\text{Ag}^+$   $\chi=5.00$  at 1mM, which was less selective than the film of other striped particles (Figure 3.3(e) and (f)).

### 3.3.2. The films of homoligand gold nanoparticles

The change of the conductivities for the nanoparticles coated with only EGn ligands was measured as it was done in the solution-based conductivity measurement. The measurement was performed for a pair of each EGn homo-nanoparticle and the corresponding ions, and the result was summarized in Table 3.1. The concentration of ion solutions was 1mM, except  $\text{CH}_3\text{Hg}^+$ , which was 0.1 mM. As shown in Table 3.1,



most of  $\chi$  values were close to unity, no bigger than 1.5, which means that there was no particular ion-binding for the homo-nanoparticles.

	EG3 homo-AuNPs	EG2 homo-AuNPs	EG1 homo-AuNPs
CH <sub>3</sub> Hg <sup>+</sup>	1.260 ± 0.365		
Cs <sup>+</sup>	1.449 ± 0.420		
Cd <sup>2+</sup>		1.351 ± 0.061	
K <sup>+</sup>		1.369 ± 0.239	
Zn <sup>2+</sup>			1.000 ± 0.002
Na <sup>+</sup>			0.975 ± 0.215

**Table 3.1.** The  $\chi$  values for the films of EGn homo-nanoparticles

### 3.3.3. Measurement in a blank sample

One control experiment was conducted to prove that the resulting  $\chi$  values were attributed to the ion binding, not caused by any water effect or drying process. The films of the striped nanoparticles were washed with Millipore water, not containing any ions, and dried. No significant change of conductance was observed for any films; for example, for the film of HT/EG2 nanoparticles,  $\chi=1.011\pm0.029$  after one wash/dry cycle and  $\chi=1.013\pm0.031$  after ten wash/dry cycles).

### 3.4. Reference

- 1 Thompson, R. B., Maliwal, B. P., Felliccia, V. L., Fierke, C. A. & McCall, K. Determination of picomolar concentrations of metal lens using fluorescence

- anisotropy: Biosensing with a "reagentless" enzyme transducer. *Anal Chem* **70**, 4717-4723, doi:Doi 10.1021/Ac980864r (1998).
- 2 Forzani, E. S., Zhang, H. Q., Chen, W. & Tao, N. J. Detection of heavy metal ions in drinking water using a high-resolution differential surface plasmon resonance sensor. *Environ Sci Technol* **39**, 1257-1262, doi:Doi 10.1021/Es049234z (2005).
- 3 Kumar, M. & Zhang, P. Highly sensitive and selective label-free optical detection of mercuric ions using photon upconverting nanoparticles. *Biosens Bioelectron* **25**, 2431-2435, doi:Doi 10.1016/J.Bios.2010.03.038 (2010).
- 4 Narin, I., Soylak, M., Elci, L. & Dogan, M. Determination of trace metal ions by AAS in natural water samples after preconcentration of pyrocatechol violet complexes on an activated carbon column. *Talanta* **52**, 1041-1046, doi:Doi 10.1016/S0039-9140(00)00468-9 (2000).
- 5 Ghaedi, M., Ahmadi, F. & Shokrollahi, A. Simultaneous preconcentration and determination of copper, nickel, cobalt and lead ions content by flame atomic absorption spectrometry. *J Hazard Mater* **142**, 272-278, doi:Doi 10.1016/J.Jhazmat.2006.08.012 (2007).
- 6 Caroli, S., Forte, G., Iamicieli, A. L. & Galoppi, B. Determination of essential and potentially toxic trace elements in honey by inductively coupled plasma-based techniques. *Talanta* **50**, 327-336, doi:Doi 10.1016/S0039-9140(99)00025-9 (1999).
- 7 Demuth, N. & Heumann, K. G. Validation of methylmercury determinations in aquatic systems by alkyl derivatization methods for GC analysis using ICP-IDMS. *Anal Chem* **73**, 4020-4027, doi:Doi 10.1021/Ac010366+ (2001).
- 8 Lee, J. S., Han, M. S. & Mirkin, C. A. Colorimetric detection of mercuric ion (Hg<sup>2+</sup>) in aqueous media using DNA-functionalized gold nanoparticles. *Angew Chem Int Edit* **46**, 4093-4096, doi:Doi 10.1002/Anie.200700269 (2007).
- 9 Huang, C. C. & Chang, H. T. Parameters for selective colorimetric sensing of mercury(II) in aqueous solutions using mercaptopropionic acid-modified gold nanoparticles. *Chem Commun*, 1215-1217, doi:Doi 10.1039/B615383f (2007).
- 10 Chiang, C. K., Huang, C. C., Liu, C. W. & Chang, H. T. Oligonucleotide-based fluorescence probe for sensitive and selective detection of mercury(II) in aqueous solution. *Anal Chem* **80**, 3716-3721, doi:Doi 10.1021/Ac800142k (2008).
- 11 Chang, H. Y., Hsiung, T. M., Huang, Y. F. & Huang, C. C. Using Rhodamine 6G-Modified Gold Nanoparticles To Detect Organic Mercury Species in Highly Saline Solutions. *Environ Sci Technol* **45**, 1534-1539, doi:Doi 10.1021/Es103369d (2011).
- 12 Kang, T., Hong, S. R., Moon, J., Oh, S. & Yi, J. Fabrication of reusable sensor for detection of Cu<sup>2+</sup> in an aqueous solution using a self-assembled monolayer with surface plasmon resonance spectroscopy. *Chem Commun*, 3721-3723, doi:Doi 10.1039/B504064g (2005).

- 13 Li, D., Wieckowska, A. & Willner, I. Optical analysis of Hg(2+) ions by oligonucleotide-gold-nanoparticle hybrids and DNA-based machines. *Angew Chem Int Edit* **47**, 3927-3931, doi:Doi 10.1002/Anie.200705991 (2008).
- 14 Wang, G. Q., Wang, Y. Q., Chen, L. X. & Choo, J. Nanomaterial-assisted aptamers for optical sensing. *Biosens Bioelectron* **25**, 1859-1868, doi:Doi 10.1016/J.Bios.2009.11.012 (2010).
- 15 Yin, J. *et al.* SERS-Active Nanoparticles for Sensitive and Selective Detection of Cadmium Ion (Cd<sup>2+</sup>). *Chemistry of Materials* **23**, 4756-4764, doi:Doi 10.1021/Cm201791r (2011).
- 16 Lin, Z. Z., Li, X. H. & Kraatz, H. B. Impedimetric Immobilized DNA-Based Sensor for Simultaneous Detection of Pb<sup>2+</sup>, Ag<sup>+</sup>, and Hg<sup>2+</sup>. *Anal Chem* **83**, 6896-6901, doi:Doi 10.1021/Ac2014096 (2011).
- 17 Zhang, Z., Yu, K., Bai, D. & Zhu, Z. Q. Synthesis and Electrochemical Sensing Toward Heavy Metals of Bunch-like Bismuth Nanostructures. *Nanoscale Res Lett* **5**, 398-402, doi:Doi 10.1007/S11671-009-9495-3 (2010).

## **4. Removal of Metal Ions from Water Using Striped Gold**

### **Nanoparticles**

#### **4.1. Introduction**

Along with the detection of the metal ions in samples, it is also necessary to remove such toxic metal ion pollutants from environments<sup>1,2</sup>. Several million tons of heavy metals, such as mercury, cadmium and lead, are discharged into environments every year as a result of human activities<sup>3-6</sup>. There have been lots of efforts into the remediation of soil and water contaminated by metals, since the metal pollutants have a crucial effect on human health, as discussed in Chapter 1. Typically, the remediation method for water includes precipitation with chemicals<sup>7</sup>, use of absorbents<sup>8,9</sup>, ion-exchange resins<sup>10</sup>, column<sup>11</sup>, and filtration with membrane<sup>12,13</sup>. However, the precipitation with chemicals results in a large amount of secondary waste, and the use of ion-exchange resins is limited to the solutions of low concentrations. Additionally, the filtration is not effective when a large volume of water needs to be processed. Therefore, it is required to properly utilize metal ion absorbent, overcoming those shortcomings. Mostly metal-adsorbent materials were manipulated in a variety of ways in the aspect of their efficiency. They can be used by themselves as sorbents, and also incorporated into filtration or membrane, and column.

For this purpose, two kinds of methods were devised in our work, utilizing these ion-selective gold nanoparticles: magnetic removal by functionalizing gold nanoparticles with magnetic nanoparticle and metal ion sponge made up of gold nanoparticles. Thanks to our striped nanoparticles, they were expected to have an excellent selectivity, and they would be usable in water and also in environmental samples. Also they would not discharge a secondary waste.

## **4.2. Magnetization of gold nanoparticles: composite nanoparticle**

### **4.2.1. Magnetic Nanoparticles**

Magnetic nanoparticles, such as iron oxide ( $\text{Fe}_3\text{O}_4$  and  $\text{Fe}_2\text{O}_3$ ), iron, nickel, and cobalt nanoparticles, have been of great interest in various fields for decades, including biomedicine<sup>14,15</sup>, magnetic resonance imaging (MRI)<sup>16,17</sup>, data storage<sup>18</sup>, and also environmental remediation<sup>9,19,20</sup>. With their diverse applications, synthetic methods and properties are well studied. By utilizing their superparamagnetic property, it was expected that it would be an excellent candidate for a remediation method when they were incorporated into our ion-selective striped nanoparticles.

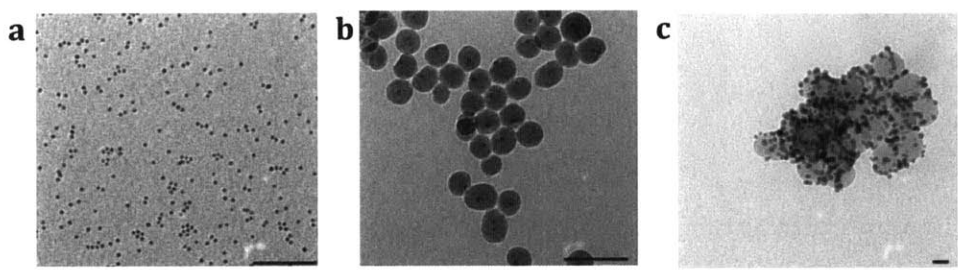
### **4.2.2. Synthesis of magnetic nanoparticles functionalized with gold nanoparticles**

Fe<sub>2</sub>O<sub>3</sub> nanoparticles were synthesized as described in the literature<sup>21</sup>. The entire procedure was carried out under an argon atmosphere. 1.52 mmol of Fe(CO)<sub>5</sub> was added into 10 mL of octyl ether in the presence of 4.56 mmol of oleic acid at 100 °C. The reactant was heated up to 280~290 °C under reflux for 1 hour. In this process, the color change was observed, resulting in black solution. The solution was cooled down to room temperature, and 4.56 mmol of (CH<sub>3</sub>)<sub>3</sub>NO was added into the mixture, followed by heating up to 130 °C, and it was kept at that temperature for 2 hours. After 2 hours, the temperature was raised again, refluxing for 1 hour. Finally, the reactant was cooled down to room temperature. The synthesized nanoparticles were precipitated by pouring ethanol, and purified by centrifuging with ethanol. They were dried under the vacuum overnight. The obtained nanoparticles were well-dispersed in hydrophobic solvents such as hexane and toluene.

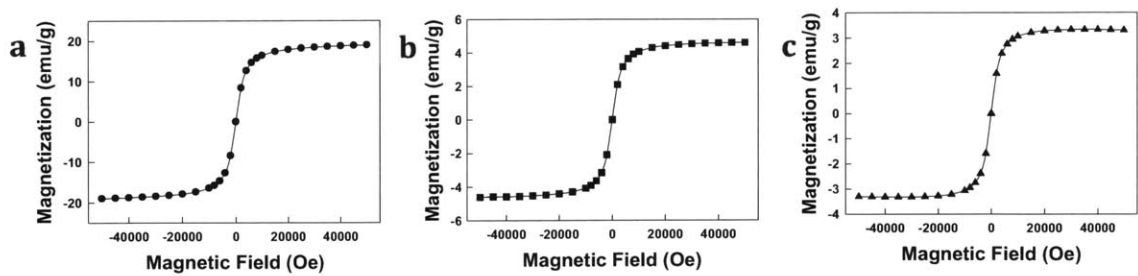
To enhance the compatibility of magnetic particles in hydrophilic solvents, they were coated with silica, which also facilitates to have functionality on the surface. These core-shell structured silica-magnetic nanoparticles have been reported with several methods, and here the silica shell was synthesized by reverse microemulsion, following the literature<sup>22,23</sup>. 80 ml of magnetic nanoparticles dispersed in cyclohexane (in a concentration of 0.4 mg/ml) were added into 440 ml of cyclohexane solution containing 35 g of polyoxyethylene(5)nonylphenyl ether (Igepal CO-520). The mixture was stirred for 30 minutes, followed by the addition of 3.5 ml of ammonium hydroxide. Finally, 1 ml of tetraethylorthosilicate (TEOS) was added, and the mixture was stirred for 2 days at room temperature. 400 ml of

ethanol was added into the solution, which made the resulting silica-magnetic nanoparticles ( $\text{SiO}_2/\text{Fe}_2\text{O}_3$ ) precipitated out. The nanoparticles were collected by centrifuging, washed with ethanol three times, and dried under the vacuum overnight.

#### 4.2.3. Characterization of magnetic nanoparticles functionalized with gold nanoparticles



**Figure 4.1.** TEM images of (a)  $\text{Fe}_2\text{O}_3$  (100 nm for scale bar), (b)  $\text{SiO}_2/\text{Fe}_2\text{O}_3$  (100 nm for scale bar), and (c) gold nanoparticle/ $\text{SiO}_2/\text{Fe}_2\text{O}_3$  (20 nm for scale bar)



**Figure 4.2.** SQUID measurement of (a)  $\text{Fe}_2\text{O}_3$ , (b)  $\text{SiO}_2/\text{Fe}_2\text{O}_3$ , and (c) gold nanoparticle/ $\text{SiO}_2/\text{Fe}_2\text{O}_3$

In each synthetic step, the morphology was examined by TEM, as shown in Figure 4.1, and the silica coating and functionalization of gold nanoparticles were observed.

Furthermore, SQUID measurement was performed to investigate the magnetic property of the particles (Figure 4.2). The resulting particles had no hysteresis, indicating their superparamagnetic properties.

#### 4.2.4. Removal of metal ions from water



**Figure 4.3.** (a) The picture that the composite particles can be easily removed by a magnet and (b) the change in conductivity value at each step: (i) the initial value without  $\text{Cd}^{2+}$ , (ii) right after adding  $\text{Cd}^{2+}$ , (iii) after mixing with the composite particles, followed by that they being removed, and (iv) after the captured  $\text{Cd}^{2+}$  being released by heating the solution up to  $80\text{ }^\circ\text{C}$

The prepared composite nanoparticles were dispersed in Millipore water and collected by a magnet, as shown in Figure 4.3(a). The conductivity was measured at first (the value indicated by (i) in Figure 4.3(b)), and cadmium ions were added into the solution, followed by the conductivity measurement again (the value indicated by (ii) in Figure 4.3(b)). The conductivity increased as a result of the addition of cadmium ions. The composite nanoparticles were released from the magnet, and stirred for a while to give a sufficient time to mix with the ions. The nanoparticles were removed by the magnet, and the conductivity of the solution was measured



(the value indicated by (iii) in Figure 4.3(b)). The conductivity value was down to mostly the initial value. From the change of the conductivity, it was inferred that the composite nanoparticles were able to get rid of most of cadmium ions from aqueous solution.

Also, the composite nanoparticles containing cadmium ions were re-dispersed again, and the temperature of the solution was raised to 80 °C. As described in Chapter 2, the captured metal ions can be released from the striped gold nanoparticles. The dispersed nanoparticles were re-collected by the magnet at 80 °C, and the conductivity was measured again after the temperature was recovered to room temperature (the value indicated by (iv) in Figure 4.3(b)). It was shown that the conductivity was increased again, implying that the captured cadmium ions were released into the solution as a result of the entropic effect at high temperature.

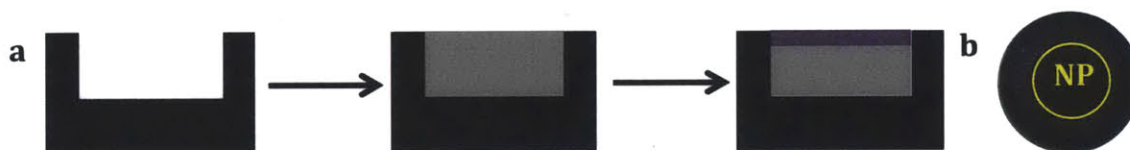
### **4.3. Metal ion sponge**

#### **4.3.1. Fabrication of metal ion sponge**

As for another remediation method, a small disk-shape pellet consisting of the striped nanoparticles was contrived. This pellet consisting of a certain kind of the striped nanoparticles was expected to function as a metal ion “sponge” when it was immersed in water contaminated by a specific type of metal ion such as

methylmercury and cadmium, by absorbing them. With this method, the striped gold nanoparticle itself can function as an absorbent.

The metal ion sponge was produced in a similar way to prepare a pellet of FT-IR sample. 60 mg of gold nanoparticles was fabricated in the pellet presser under the pressure of 6000 psi for 2 minutes. According to the previous literature, it was confirmed that the nanoparticles would not be affected under the high pressure<sup>24,25</sup>. The resulting pellet made up of gold nanoparticles was cross-linked by dipping it in 2 ml of 1,9-nonanedithiol for 2 hours to preventing them from dissolving out in water, and it was placed in a plastic frame with epoxy glue, as shown in Figure 4.4(a).



**Figure 4.4.** (a) The schematic representation of manipulating the metal ion sponge (black: plastic frame, gray: epoxy resin, purple: nanoparticle-pellet, and (b) The picture of metal ion sponge in a plastic frame

#### 4.3.2. Absorption of metal ions from water

The prepared metal ion sponge was placed in aqueous solution containing a certain concentration of cadmium ions. The conductivity of the solution was measured prior to putting the metal ion sponge for a reference value. The solution was stirred for a

while to improve the absorbing efficiency. The metal ion sponge was taken out from the solution, and the conductivity was measured again, as indicated in Figure 4.4(b). The conductivity decreased to some extent, displaying that some amount of cadmium ions in the solution was absorbed by the metal ion sponge.

#### **4.3.3. Removal of metal ions from an environmental sample**

In the following step, it was applied to an environmental sample. The lake sediment was collected from Lake Geneva, and two samples were taken in a same condition. Only one sample was spiked with a known concentration of cadmium ions. The initial concentration of the cadmium was determined by following the real concentration of other cadmium-contaminated lake, Empire Lake located in Kansas, which was monitored by USGS (the United States Geological Survey). Two sponge consisting of the same HT/EG2 striped nanoparticles were placed into each sediment sample: one is native sediment and the other is Cd<sup>2+</sup>-spiked sample (in a concentration of 87.2 ppm). The samples with the nanoparticle-pellet were shaken for 1 hour. Each pellet was taken from the sediment sample, and put in 25 ml of hot water (approximately 80 °C). The hot water was collected for ICP measurement. Under our hypothesis, a certain amount of Cd<sup>2+</sup> would be detected, since it would be released from the pellet into hot water, if the pellet absorbed some amount of Cd<sup>2+</sup> from the sediment sample, proving that amount of Cd<sup>2+</sup> was reduced in the sediment by the effect of the metal ion sponge. From ICP, no Cd<sup>2+</sup> was found in the pellet sample from the native sediment, whereas 5.89 ppm of Cd<sup>2+</sup> was detected that from

Cd<sup>2+</sup>-spiked sediment. It obviously indicated that the nanoparticle-pellet was able to absorb Cd<sup>2+</sup> ions from the environmental sample, which presented the potential use in an effective remediation.

As shown in the result of both the conductivity test and ICP, the removal efficiency of the metal ion sponge is not as good as that of the composite particle in the previous section (Chapter 4.2). It can be deduced that it was caused by the difference of surface area exposed to water. For the composite nanoparticles, the gold nanoparticles attached to the magnetic particles were completely exposed to water, leading to high surface area with metal ions in water. However, in the case of this metal ion sponge, the surface area is smaller, which requires more time for metal ions to be diffused into the nanoparticle-pellet. Despite of that, certainly it can function as a kind of metal ion “sponge” in water by simply putting it into water; therefore, with a slight engineering modification, it is expected that it can excellently act as a metal ion sponge.

#### 4.4. References

- 1 Akpor, O. B. & Muchie, M. Remediation of heavy metals in drinking water and wastewater treatment systems: Processes and applications. *Int J Phys Sci* **5**, 1807-1817 (2010).
- 2 Mulligan, C. N., Yong, R. N. & Gibbs, B. F. An evaluation of technologies for the heavy metal remediation of dredged sediments. *J Hazard Mater* **85**, 145-163, doi:Doi 10.1016/S0304-3894(01)00226-6 (2001).
- 3 Jarup, L., Berglund, M., Elinder, C. G., Nordberg, G. & Vahter, M. Health effects of cadmium exposure - a review of the literature and a risk estimate. (vol 24, pg 1, 1998). *Scand J Work Env Hea* **24**, 240-240 (1998).

- 4 Clifton, J. C. Mercury exposure and public health. *Pediatr Clin N Am* **54**, 237-+,  
doi:Doi 10.1016/J.Pcl.2007.02.005 (2007).
- 5 Staudinger, K. & Roth, V. S. Occupational lead poisoning. *Am Fam Physician*  
**57**, 719-726 (1998).
- 6 Smith, A. H. *et al.* Cancer Risks from Arsenic in Drinking-Water. *Environ*  
*Health Persp* **97**, 259-267, doi:Doi 10.2307/3431362 (1992).
- 7 Matlock, M. M., Howerton, B. S. & Atwood, D. A. Chemical precipitation of  
heavy metals from acid mine drainage. *Water Res* **36**, 4757-4764, doi:Pii  
S0043-1354(02)00149-5 Doi 10.1016/S0043-1354(02)00149-5 (2002).
- 8 Zvinowanda, C. M., Okonkwo, J. O., Shabalala, P. N. & Agyei, N. M. A novel  
adsorbent for heavy metal remediation in aqueous environments. *Int J*  
*Environ Sci Te* **6**, 425-434 (2009).
- 9 Yantasee, W. *et al.* Removal of heavy metals from aqueous systems with thiol  
functionalized superparamagnetic nanoparticles. *Environ Sci Technol* **41**,  
5114-5119, doi:Doi 10.1021/Es0705238 (2007).
- 10 Wang, L., Fields, K. A., Chen, A. H. & National Risk Management Research  
Laboratory (U.S.). (National Risk Management Research Laboratory, Office  
of Research and Development, U.S. Environmental Protection Agency,,  
Cincinnati, Ohio, 2000).
- 11 Lisha, K. P., Anshup & Pradeep, T. Towards a practical solution for removing  
inorganic mercury from drinking water using gold nanoparticles. *Gold Bull*  
**42**, 144-152 (2009).
- 12 Kostal, J. *et al.* Customizable biopolymers for heavy metal remediation. *J*  
*Nanopart Res* **7**, 517-523, doi:Doi 10.1007/S11051-005-5132-Y (2005).
- 13 Sang, Y. M., Li, F. S., Gu, Q. B., Liang, C. Z. & Chen, J. Q. Heavy metal-  
contaminated groundwater treatment by a novel nanofiber membrane.  
*Desalination* **223**, 349-360, doi:Doi 10.1016/J.Desal.2007.01.208 (2008).
- 14 Gupta, A. K. & Gupta, M. Synthesis and surface engineering of iron oxide  
nanoparticles for biomedical applications. *Biomaterials* **26**, 3995-4021,  
doi:Doi 10.1016/J.Biomaterials.2004.10.012 (2005).
- 15 Gupta, A. K. & Gupta, M. Cytotoxicity suppression and cellular uptake  
enhancement of surface modified magnetic nanoparticles. *Biomaterials* **26**,  
1565-1573, doi:Doi 10.1016/J.Biomaterials.2004.05.022 (2005).
- 16 Mornet, S. *et al.* Magnetic nanoparticle design for medical applications. *Prog*  
*Solid State Ch* **34**, 237-247, doi:Doi 10.1016/J.Progsolidstchem.2005.11.010  
(2006).
- 17 Li, Z., Wei, L., Gao, M. Y. & Lei, H. One-pot reaction to synthesize  
biocompatible magnetite nanoparticles. *Advanced Materials* **17**, 1001-+,  
doi:Doi 10.1002/Adma.200401545 (2005).
- 18 Hyeon, T. Chemical synthesis of magnetic nanoparticles. *Chem Commun*, 927-  
934, doi:Doi 10.1039/B207789b (2003).
- 19 Elliott, D. W. & Zhang, W. X. Field assessment of nanoscale biometallic  
particles for groundwater treatment. *Environ Sci Technol* **35**, 4922-4926,  
doi:Doi 10.1021/Es0108584 (2001).
- 20 Takafuji, M., Ide, S., Ihara, H. & Xu, Z. H. Preparation of poly(1-  
vinylimidazole)-grafted magnetic nanoparticles and their application for

- removal of metal ions. *Chemistry of Materials* **16**, 1977-1983, doi:Doi 10.1021/Cm030334y (2004).
- 21 Hyeon, T., Lee, S. S., Park, J., Chung, Y. & Bin Na, H. Synthesis of highly crystalline and monodisperse maghemite nanocrystallites without a size-selection process. *Journal of the American Chemical Society* **123**, 12798-12801, doi:Doi 10.1021/Ja016812s (2001).
- 22 Yi, D. K., Lee, S. S. & Ying, J. Y. Synthesis and applications of magnetic nanocomposite catalysts. *Chemistry of Materials* **18**, 2459-2461, doi:Doi 10.1021/Cm052885p (2006).
- 23 Lee, J. *et al.* Simple synthesis of functionalized superparamagnetic magnetite/silica core/shell nanoparticles and their application as magnetically separable high-performance biocatalysts. *Small* **4**, 143-152, doi:Doi 10.1002/Sml.200700456 (2008).
- 24 Hostler, S. R. *et al.* Thermoelectric properties of pressed bismuth nanoparticles. *Superlattice Microst* **43**, 195-207, doi:Doi 10.1016/J.Spmi.2007.10.001 (2008).
- 25 Liu, K., Zhao, L., Klavins, P., Osterloh, F. E. & Hiramatsu, H. Extrinsic magnetoresistance in magnetite nanoparticles. *J Appl Phys* **93**, 7951-7953, doi:Doi 10.1063/1.1556133 (2003).

## 5. Temperature Effect on Ion-Capturing

### 5.1. Introduction

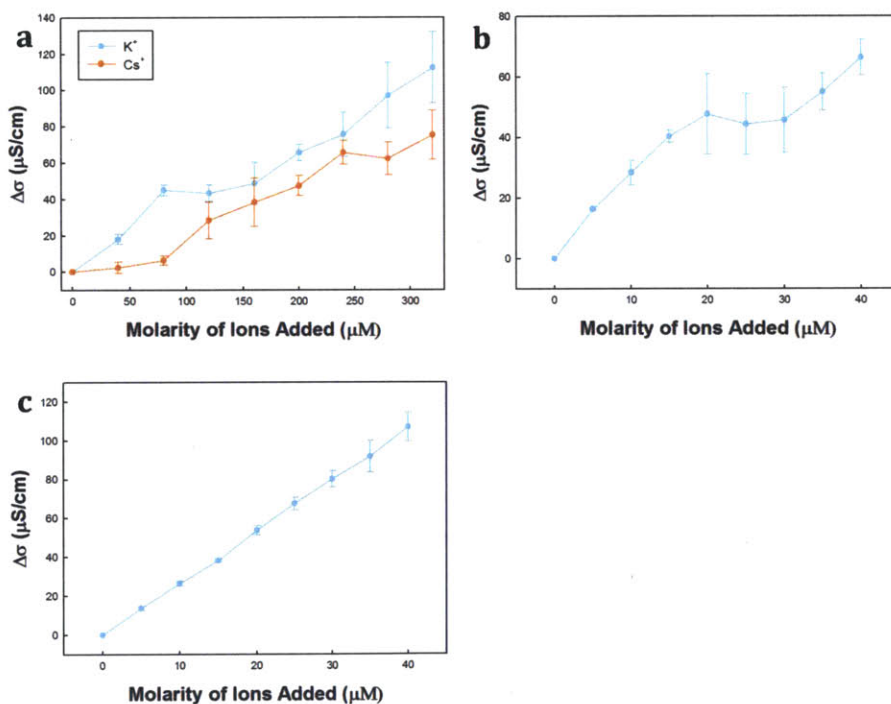
In the earlier work, it was observed that the captured metal ions were released from gold nanoparticles at 80 °C, as described in Chapter 2. Presumably, it is caused by the change of entropic contribution to free energy, accompanied by the increased temperature. In this context, it was assumed that the change of the temperature would be a key factor to alter the kinetics in ion-capturing mechanism. Accordingly, it was expected that a different ion-capturing behavior could be observed in a different temperature.

In thermodynamic studies on the complexation of crown ethers and metal ions, it is said that the enthalpy plays a key role in the free energy and the entropy is negligible<sup>1-3</sup>. Hence, when binding constants of different types of crown ethers were compared, mostly only enthalpy was regarded as an important parameter<sup>4</sup>. This is attributed to the rigidity of macrocyclic rings, where the change of the entropy would not be noticeable.

However, in our system the ion-capturing parts (i.e. EGn ligands) are quite flexible, unlike the rigid crown ethers<sup>5,6</sup>. This property would lead to a pronounced entropy change upon a complexation with metal ions, and also upon the temperature change.

This experiment was focused on HT/EG3 striped particle, and it was tested with various kinds of metal ions at different temperatures. The conductivity test result presented a different ion-capturing behavior according to the temperature, and it was commensurate with the following ITC results. Furthermore, FT-IR measurement supported that the change in the ion-capturing behavior was not induced by the modification in ligand-shell structure accompanied by the temperature.

## 5.2. Different ion-capturing behavior on conductivity test



**Figure 5.1.** The result of conductivity test for HT/EG3 striped nanoparticles (a) at 40 °C with  $\text{K}^+$  and  $\text{Cs}^+$ , (b) at 50 °C with  $\text{K}^+$ , (c) at 60 °C with  $\text{K}^+$ ; each measurement was done at least three times, resulting in the plots using their average values with the standard deviations, represented by error bars.

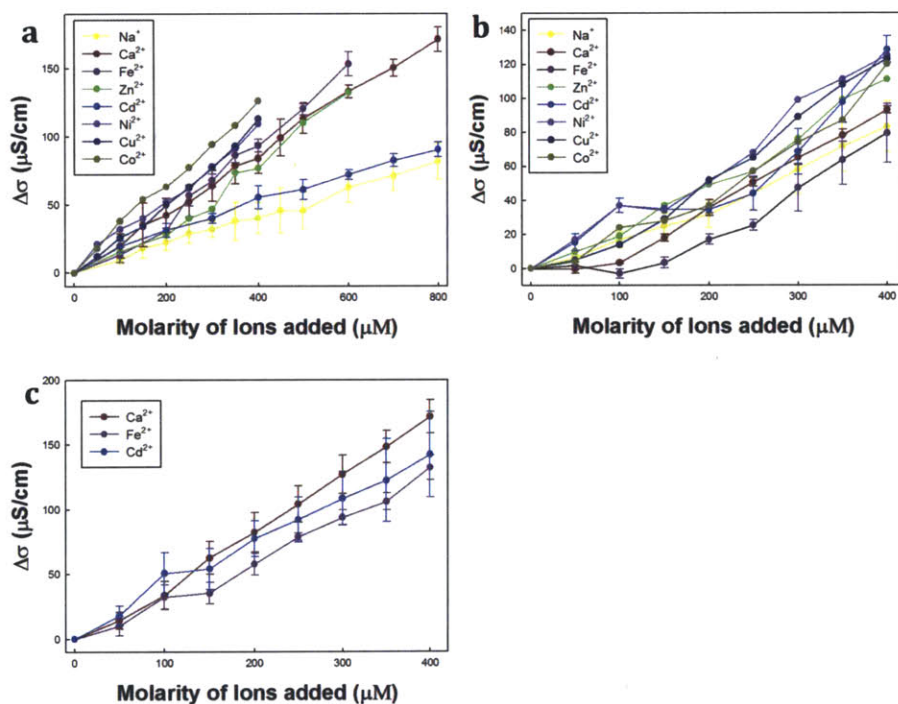


Conductivity tests similar to the ones described in Chapter 2 were performed at various temperatures; the striped nanoparticle solution was placed in an oil bath to maintain a certain temperature. The results were shown in Figure 5.1

Firstly, HT/EG3 striped particles were tested with  $K^+$  and  $Cs^+$  at 40 °C, and it was found that less  $Cs^+$  was captured by the nanoparticles, compared to at room temperature. More interestingly, a certain amount of  $K^+$  started to be trapped by HT/EG3 striped nanoparticles after adding some aliquots of  $K^+$  solutions, as shown in Figure 5.1(a). The plateau region was observed in the middle of the plot, unlike other ordinary plots, where it was spotted from the beginning. To determine that this was caused by time or concentration, the conductivity was measured again with a sufficient interval between measurements (more than 12 hours). The change in the conductivity behaved similarly, even though it had a quite long time interval, which implied that this was not the time issue, but the concentration issue. In other words, at 40°C, the HT/EG3 striped particles are able to trap  $K^+$  ions only in the presence of some amount of  $K^+$  ions. A similar phenomenon was observed at 50 °C, as shown in Figure 5.1(b); the plateau region was moved to the right slightly, requiring a higher concentration of  $K^+$  to be bound. However, no capturing was found at 60 °C (Figure 5.1(c)).

In the similar way, other kinds of metal ions such as  $Na^+$ ,  $Ca^{2+}$ ,  $Fe^{2+}$ ,  $Zn^{2+}$ ,  $Cd^{2+}$ ,  $Ni^{2+}$ ,  $Cu^{2+}$  and  $Co^{2+}$  were tested at elevated temperatures (Figure 5.2).  $Na^+$ ,  $Zn^{2+}$ ,  $Ni^{2+}$ ,  $Cu^{2+}$

and  $\text{Co}^{2+}$  were bound to HT/EG3 striped particles neither at room temperature nor at the elevated temperatures. On the contrary,  $\text{Ca}^{2+}$ ,  $\text{Fe}^{2+}$ , and  $\text{Cd}^{2+}$  displayed a different behavior at the elevated temperatures. None of them were trapped by HT/EG3 striped particles at room temperature, but  $\text{Ca}^{2+}$  and  $\text{Fe}^{2+}$  were captured at  $40^\circ\text{C}$  from the beginning, although they required a longer time to be stabilized, and  $\text{Cd}^{2+}$  started to be captured after some amount of them were added, just as  $\text{K}^+$ . At  $50^\circ\text{C}$ , this capturing was significantly alleviated for  $\text{Fe}^{2+}$  and  $\text{Cd}^{2+}$ , while no binding was observed for  $\text{Ca}^{2+}$ .



**Figure 5.2.** The result of conductivity test for HT/EG3 striped nanoparticles with (a)  $\text{Na}^+$ ,  $\text{Ca}^{2+}$ ,  $\text{Fe}^{2+}$ ,  $\text{Zn}^{2+}$ ,  $\text{Cd}^{2+}$ ,  $\text{Ni}^{2+}$ ,  $\text{Cu}^{2+}$  and  $\text{Co}^{2+}$  at room temperature, (b)  $\text{Na}^+$ ,  $\text{Ca}^{2+}$ ,  $\text{Fe}^{2+}$ ,  $\text{Zn}^{2+}$ ,  $\text{Cd}^{2+}$ ,  $\text{Ni}^{2+}$ ,  $\text{Cu}^{2+}$  and  $\text{Co}^{2+}$  at  $40^\circ\text{C}$  and (c)  $\text{Ca}^{2+}$ ,  $\text{Fe}^{2+}$ , and  $\text{Cd}^{2+}$  at  $50^\circ\text{C}$ ; each measurement was done at least three times, resulting in the plots using their average values with the standard deviations, represented by error bars.

In summary, the ion-capturing clearly have shown a different behavior at the elevated temperatures for our striped nanoparticles, even though it was just focused on the case of HT/EG3 particles. Also, each case with different metal ions took on a different aspect, signifying that the subtle difference in the electrostatic interaction determines the ion-binding, coming with the entropic effect at varying temperatures.

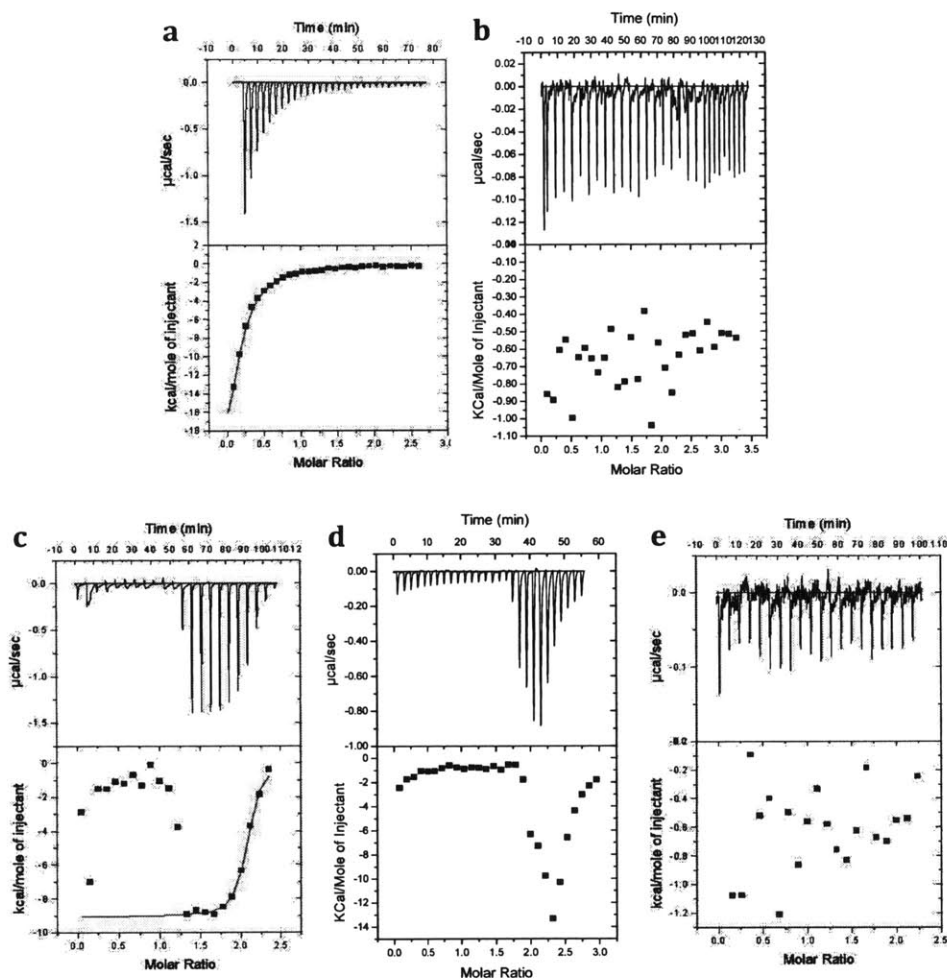
### **5.3. Characterization of metal ion-capturing gold nanoparticles at high temperatures**

#### **5.3.1. Isothermal titration calorimetry (ITC)**

In a similar way as depicted in Chapter 2, ITC measurements were conducted at elevated temperatures to acquire the thermodynamic parameters at different temperatures. Basically, they were performed in a same protocol, except the temperature. We focused on the analysis of HT/EG3 striped particles with  $K^+$  and  $Cs^+$  ions, and the results are illustrated in Figure 5.3.

Firstly, when the parameters with  $Cs^+$  at 40 °C are compared to those at room temperature, clearly the stoichiometric ratio decreased, indicating less  $Cs^+$  was captured at 40°C than at room temperature, which is quite consistent with the conductivity test. Also, the enthalpy changes were fairly similar, whereas more entropy was sacrificed at 40°C, and the binding constant was remarkably lowered at

40 °C. No significant Cs<sup>+</sup>-binding was found at 60 °C.



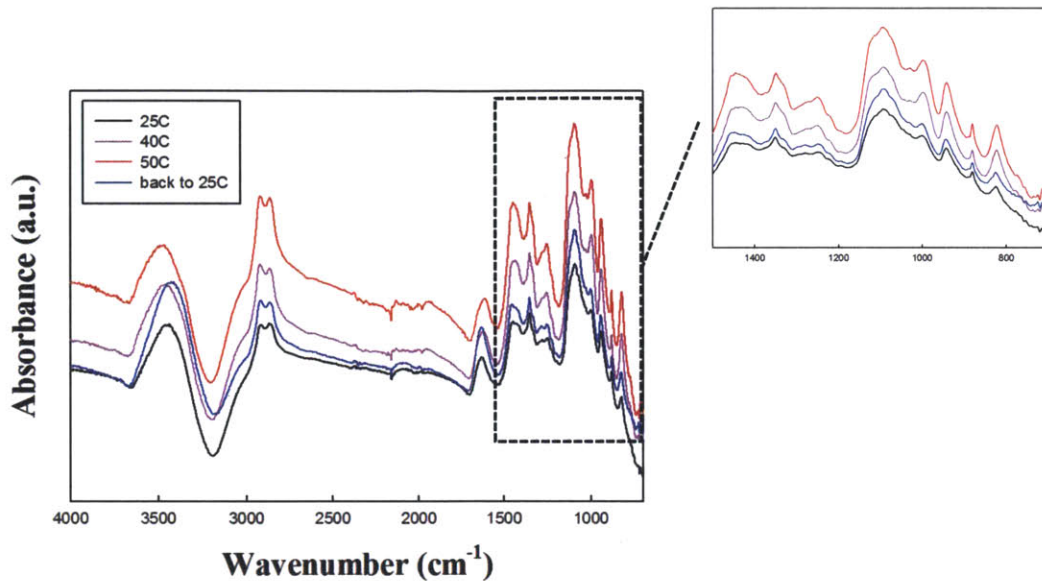
**Figure 5.3.** ITC results for HT/EG3 particles (a) with Cs<sup>+</sup> at 40 °C:  $N=0.210$ ,  $K=1.94 \times 10^5 (\pm 1.69 \times 10^4)$ ,  $\Delta H=-89.376$  kJ/mol,  $\Delta S=-197.4$  J/mol•K, (b) with Cs<sup>+</sup> at 60 °C: no particular change, (c) with K<sup>+</sup> at 40 °C:  $N=0.891$ ,  $K=1.05 \times 10^6 (\pm 5.00 \times 10^5)$ ,  $\Delta H=-40.333$  kJ/mol,  $\Delta S=-13.58$  J/mol•K, (d) with K<sup>+</sup> at 50 °C:  $N=0.704$ ,  $K=2.92 \times 10^6 (\pm 1.41 \times 10^6)$ ,  $\Delta H=-46.074$  kJ/mol,  $\Delta S=-30.324$  J/mol•K, and with (e) K<sup>+</sup> at 60 °C: no particular change

For HT/EG3 particles with K<sup>+</sup>, the heat change was observed in the reaction only after passing by several injections both at 40 °C and 50 °C, which is commensurate

with the conductivity test in the previous section. The thermodynamic parameters and the stoichiometric ratios were similar for both cases; however, all values were lower than the complex of HT/EG2 particles and  $K^+$  at room temperature, which was presented in Chapter 2. Also, no  $K^+$ -capturing was observed at 60 °C.

### **5.3.2. Fourier transform infrared spectroscopy (FT-IR)**

To verify that the change of the ion-capturing behavior with varying temperatures was not induced by transforming the pattern of the ligands shell, FT-IR measurement was carried out in the liquid state by varying the temperature (Figure 5.4). The measurement was achieved in a similar way as depicted in Chapter 2, using ATR accessory, but the sample trough plate was connected to a temperature controller (with  $\pm 0.1^\circ\text{C}$  accuracy). For background measurement, water solution without nanoparticles was used first at each temperature. Initially, HT/EG3 aqueous solution was measured at room temperature and also at higher temperatures (at 40 °C and at 50 °C). There was no substantial change in the spectra, especially in the region of the motions for -C-C- and -C-O-, and it was still same after recovering to room temperature. Therefore, it was concluded that there was no change in the ligand shell structure up to 50 °C and the change in ion-capturing behavior was not caused by any change in the ligand shell.



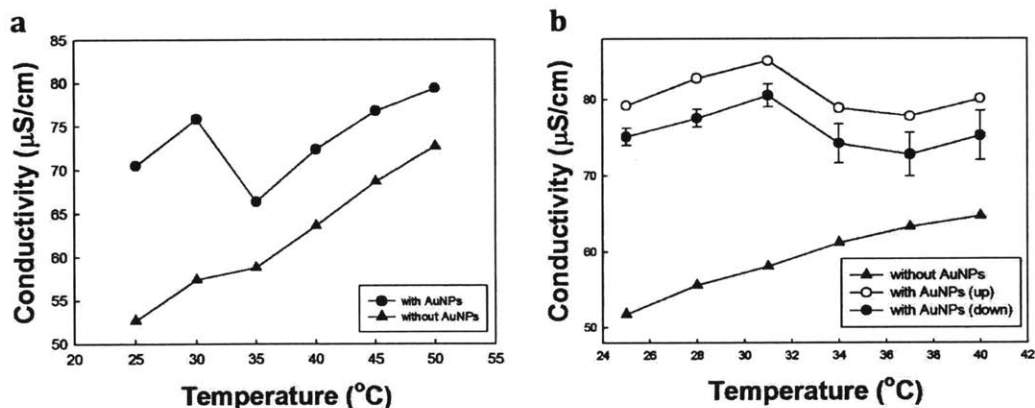
**Figure 5.4.** FT-IR spectra of HT/EG3 striped particles at varied temperatures

#### 5.4. Transition temperature

According to the conductivity test in the previous section, HT/EG3 striped particles were able to trap  $K^+$  ions only at elevated temperatures, but not at room temperatures. This  $K^+$ -capturing was observed in a range of  $40\text{ }^\circ\text{C} \sim 50\text{ }^\circ\text{C}$ ; hence, it was assumed that there would be a kind of transition temperature between room temperature and  $40\text{ }^\circ\text{C}$ .

To confirm the presence of the transition point, HT/EG3 striped nanoparticles were mixed with a stoichiometric amount of  $K^+$  at room temperature, and the conductivity was measured at each step upon raising the temperature by 5 degree. 30 minutes were given between each measurement for equilibrium after reaching a target temperature, and the result was represented in Figure 5.5(a). It was shown

that the conductivity of the control sample (i.e. only K<sup>+</sup> without nanoparticles) linearly increased, which was induced by the thermal effect on the conductivity; however, for the sample with HT/EG3 nanoparticles, this increasing pattern was ceased around 30 °C, and suddenly the conductivity value plunged. This implied that a certain amount of K<sup>+</sup> ions freely existed was bound to HT/EG3 nanoparticles at the corresponding temperature range, accompanying the decreased in the conductivity. The conductivity value increased again afterwards as a result of the thermal effect. This suggested that there would be a transition point around 30~35 °C.



**Figure 5.5.** The change in conductivity of K<sup>+</sup> aqueous solution with and without HT/EG3 nanoparticles measured by varying the temperature (a) in 5 degrees and (b) in 3 degrees

To find this transition temperature, the conductivity test was carried out in a more elaborated scale. The change in conductivity was investigated, varying the temperature from 25 °C to 40 °C by 3 degrees in each step (indicated with open circles in Figure 5.5(b)). The control experiment without nanoparticles was also

carried out to examine the thermal effect, and it was demonstrated that the conductivity increased linearly by temperature in the presence of only metal ions (indicated with triangles in Figure 5.5(b)). In Figure 5.5(b), the conductivity value reduced twice: firstly between 31 °C and 34 °C, and secondly between 34 °C and 37 °C. The drop in the conductivity was more noticeable in the former range than the latter one; hence it was deduced that the transition point would exist around 34 °C. The conductivity was measured again by reducing the temperature from 40 °C to 25 °C with the same solution after it reached 40 °C (indicated with closed circles in Figure 5.5(b)). A similar phenomenon was observed in an opposite way; the conductivity decreased at the beginning by lowering the temperature, and it escalated in the same temperature ranges. This also indicated the presence of the transition temperature.

## 5.5. Reference

- 1 Izatt, R. M., Bradshaw, J. S., Nielsen, S. A., Lamb, J. D. & Christensen, J. J. Thermodynamic and Kinetic Data for Cation Macrocyclic Interaction. *Chem Rev* **85**, 271-339, doi:Doi 10.1021/Cr00068a003 (1985).
- 2 Jozwiak, M. & Kosiorowska, M. A. Effect of Temperature on the Process of Hydrophobic Hydration. Part I. Hydrophobic Hydration of 1,4-Dioxane and 12-Crown-4 Ethers. *J Chem Eng Data* **55**, 2776-2780, doi:Doi 10.1021/Je900996k (2010).
- 3 Jozwiak, M., Kosiorowska, M. A. & Wasiak, M. Effect of Temperature on the Process of Hydrophobic Hydration. Part II. Hydrophobic Hydration of 15-Crown-5 and 18-Crown-6 Ethers. *J Chem Eng Data* **55**, 5138-5143, doi:Doi 10.1021/Je100700z (2010).
- 4 Spencer, J. N. *et al.* Comparison of the Macrocyclic Effect for Ether Hosts in Aqueous and Organic-Solvents. *J Phys Chem-Us* **97**, 10509-10512, doi:Doi 10.1021/J100142a040 (1993).
- 5 Borodin, O., Douglas, R., Smith, G. A., Trouw, F. & Petrucci, S. MD Simulations and experimental study of structure, dynamics, and thermodynamics of



- poly(ethylene oxide) and its oligomers. *J Phys Chem B* **107**, 6813-6823, doi:Doi 10.1021/Jp0275387 (2003).
- 6 Sasanuma, Y. *et al.* Conformational characteristics of poly(ethylene sulfide) and poly(ethylene oxide): Solvent dependence of attractive and repulsive gauche effects. *Macromolecules* **35**, 3748-3761, doi:Doi 10.1021/Ma012027o (2002).

## **6. Ion-Capturing with a Different Core Material: Eu<sup>3+</sup>-Binding to Silver Nanoparticles**

### **6.1. Introduction**

Theoretically, the striped structure was originated from the nature of two ligands and the curvature of nanoparticle (i.e. the size of nanoparticle)<sup>1</sup>. Hence, with an appropriate end-group functionality, which can be adsorbed onto a specific core material, we expect that the striped structure can be formed on a surface of a different metal nanoparticle. Here, silver nanoparticles were produced in the same way as gold nanoparticles, and their ion-capturing ability was investigated with optically active ions.

### **6.2. Background for lanthanide ions**

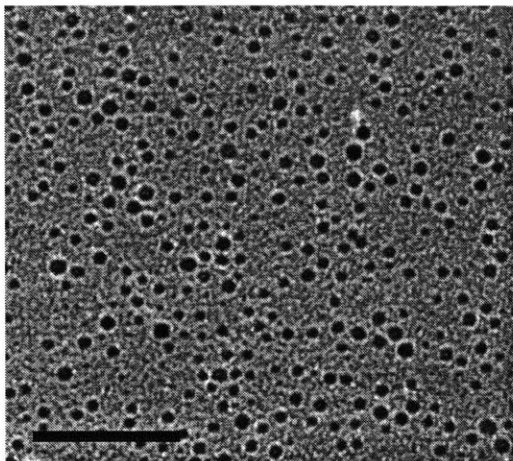
Recently optically active lanthanide ions have attracted lots of interest because of their potential applications in light emitting diode (LED)<sup>2</sup>, optical signal amplifier, laser<sup>3,4</sup>, fluoroimmunoassay<sup>5,6</sup>, and probes in biochemistry<sup>7,8</sup>. This is attributed by their unique optical properties, compared to other luminophores such as semiconductor nanoparticles and organic dye molecule; they have a large Stokes shift, long emission lifetime in the unit of milli-seconds, narrow emission bands, and higher color purity. Furthermore, lanthanide ions display multiple emissions, induced by several electronic transitions. Their excitation and emission spectra are

very sensitive to specific structural properties of ligands around them, which makes them highly promising tool for obtaining structural information. For this reason, lanthanide ions, especially  $\text{Eu}^{3+}$  and  $\text{Tb}^{3+}$ , are considered as a good candidate in diverse applications<sup>9</sup>.

To materialize them, it is critical to find a ligand, which is compatible with those metal ions, and also appropriate coordination chemistry is required for selectivity. It is known that lanthanide ions rarely interact with purely neutral ligands in an aqueous solution, since they are regarded as “hard” acids in the Pearson classification. The negatively charged oxygen atoms are included in the binding sites so that they can compete with water molecules. Also, even when these lanthanide ions bind to neutral molecules, they are in the form of very complicated multi-dentate structure.

It is well known that metal nanoparticles such as gold nanoparticle and silver nanoparticle change the optical properties of luminophore when it exists nearby<sup>10-15</sup>. Specifically, it depends on the distance between nanoparticles and luminophore, and the fluorescence could be enhanced or quenched under the influence of nanoparticles as shown in many studies<sup>15,16</sup>. In this work, the change of the luminescent property of europium ions under the interaction of the striped nanoparticles was examined.

### 6.3. Synthesis and characterization of silver nanoparticles



**Figure 6.1.** A typical TEM image of silver nanoparticles (The scale bar is 50 nm.)

In the preparation<sup>17</sup>, a thiol mixture (0.45 mmol) of OT and EG3 in the ratio of 1:3 was added into a solution of  $\text{AgNO}_3$  (0.9 mmol) in ethanol, and kept stirring for 20 min. A 80 ml of saturated  $\text{NaBH}_4$  (0.125 M) solution was added into the reactant drop-wise under vigorous stirring for 1h, and the reaction mixture was left for additional 2 h with stirring to complete the reaction. The resulting solution was purified by filtering and washing with copious amount of ethanol. The size distribution and morphology for the obtained silver nanoparticles were characterized by a transmission electron microscope (TEM), and a typical TEM image of silver nanoparticles are shown in Figure 6.1, and the average core size of silver nanoparticles is about 3.50 nm ( $\pm 0.73$  nm). The ligand ratio of the resulting silver nanoparticles was confirmed by NMR.

Also, silver nanoparticles coated with only EG3 ligands (EG3 homo-nanoparticles) were synthesized for a control experiment in the same way, and showed a similar size distribution with the striped silver nanoparticles.

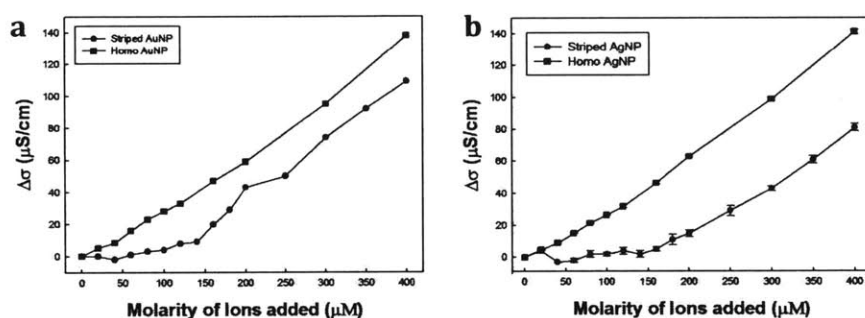
## **6.4. Investigation of the interaction between the striped nanoparticles and $\text{Eu}^{3+}$**

### **6.4.1. Conductivity test**

The conductivity test was performed with an aqueous gold and silver nanoparticle solution in a similar way as described in Chapter 2, by adding an aliquot of  $\text{EuCl}_3$  to it. Prior to the silver nanoparticles, the striped gold nanoparticles with a same ligand composition was tested (Figure 6.2(a)). The conductivity was not increased at the beginning of the addition, indicating that  $\text{Eu}^{3+}$  ions were captured by the nanoparticles. However, it increased linearly for homo-nanoparticles from the beginning as  $\text{Eu}^{3+}$  aliquots were added, implying no interaction between the nanoparticles and  $\text{Eu}^{3+}$ .

The same conductivity test was carried out with the silver nanoparticles. Figure 6.2(b) shows the change of conductivity of silver nanoparticle solutions on the addition of  $\text{Eu}^{3+}$ , displaying different patterns for the striped silver nanoparticles and the homo-nanoparticles. Upon the addition of  $\text{EuCl}_3$  into silver nanoparticle

solutions, the conductivity of the striped silver nanoparticles did not increase for a while, showing a plateau region, whereas that of the homo-nanoparticles increased linearly from the beginning. This conductivity result for silver nanoparticles was exactly consistent with for gold nanoparticles, and we assumed that silver nanoparticles would behave similarly with gold nanoparticles, forming the striped structure with the same ligand composition.

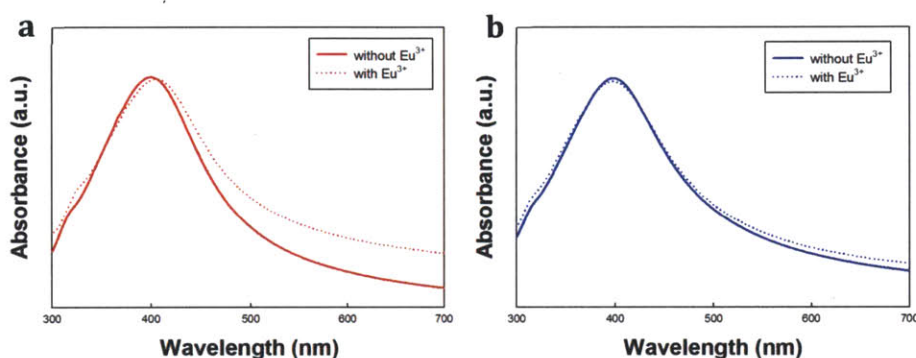


**Figure 6.2.** The conductivity test upon the addition of  $\text{Eu}^{3+}$  ions for (a) OT/EG3 striped and EG3 homo-gold nanoparticles and (b) OT/EG3 striped and EG3 homo- silver nanoparticles; each measurement was done at least three times, resulting in the plots using their average values with the standard deviations, represented by error bars.

#### 6.4.2. Ultraviolet-visible spectroscopy (UV-vis)

UV-vis measurement was performed with silver nanoparticles in the same way as illustrated in Chapter 2. The absorption spectra also displayed a similar phenomenon as gold nanoparticles (Figure 6.3). A characteristic band was observed around 400 nm for the striped silver nanoparticles, corresponding to the surface

plasmon absorption of silver nanoparticles, and it was slightly red-shifted in the presence of  $\text{Eu}^{3+}$ , attributed to the interaction between the striped silver nanoparticles and  $\text{Eu}^{3+}$ . However, no spectral change was observed for the homo-nanoparticles.



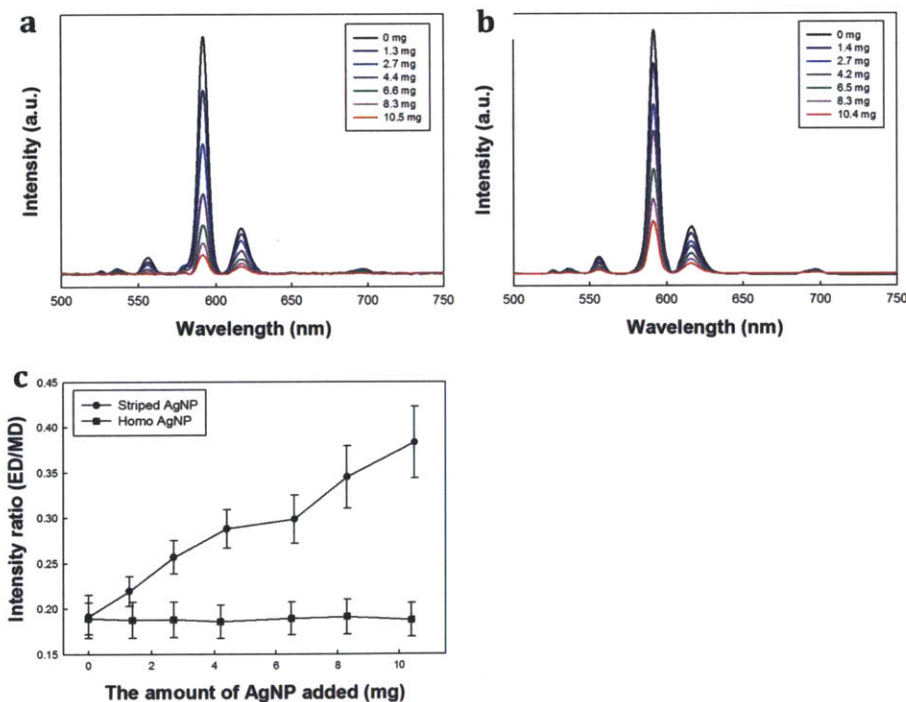
**Figure 6.3.** The change of UV-vis spectra upon the addition of  $\text{Eu}^{3+}$  (a) for the striped silver nanoparticles and (b) for the EG3 homo-silver nanoparticles (the solid lines: only silver nanoparticles without  $\text{Eu}^{3+}$ , the dot lines: silver nanoparticles with  $\text{Eu}^{3+}$ )

### 6.4.3. Fluorescence

The effect of silver nanoparticles on the emission intensity of  $\text{Eu}^{3+}$  was presented in Figure 6.4. All emission spectra were obtained with an excitation wavelength at 394 nm, which is the strongest absorption peak of  $\text{EuCl}_3$ .

Generally, there are five major emission peaks for  $\text{Eu}^{3+}$ , radiating from the non-degenerate  $^5\text{D}_0$  to  $^7\text{F}_j$  levels ( $J=0, 1, 2, 3, 4$ )<sup>10,18</sup>. Among them, two peaks arising from the transitions to  $^7\text{F}_1$  and  $^7\text{F}_2$  are stronger than others, and regarded as important.

Obviously, two major emission peaks were observed at 592 nm and 617 nm, corresponding to the transition of  $^5D_0$  to  $^7F_1$  and  $^5D_0$  to  $^7F_2$ , respectively. The  $^5D_0$  to  $^7F_1$  transition is induced by magnetic dipole one. The intensity of this transition is influenced by the crystal field strength upon  $\text{Eu}^{3+}$ , but not easily affected by the ligand environment. On the other hand, the  $^5D_0$  to  $^7F_2$  transition is attributed by electric dipole characteristics, which is highly sensitive to its detailed feature of the ligand environment in the vicinity of  $\text{Eu}^{3+}$ . For this reason, the intensity ratio between  $^5D_0$  to  $^7F_2$  transition and  $^5D_0$  to  $^7F_1$  transition is considered as a very useful tool to determine the coordination environment of  $\text{Eu}^{3+}$  due to the hypersensitive property of  $^5D_0$  to  $^7F_2$  transition<sup>10,19,20</sup>.



**Figure 6.4.** Variation of emission intensity of  $\text{Eu}^{3+}$  on the addition of (a) the striped silver nanoparticles and (b) the EG3 homo-silver nanoparticles, and (c) the intensity ratio of the transition of  $^5D_0$  to  $^7F_2$  transition and  $^5D_0$  to  $^7F_1$  transition for both types of silver nanoparticles



In Figure 6.4(a) and 6.4(b), it is shown that for both the striped and homo-nanoparticles, the fluorescence intensities of  $\text{Eu}^{3+}$  were reduced upon the addition of silver nanoparticles. However, the decreasing patterns were clearly different, comparing the intensity ratios between  ${}^5\text{D}_0$  to  ${}^7\text{F}_2$  transition (ED) and  ${}^5\text{D}_0$  to  ${}^7\text{F}_1$  transition (MD), as shown in Figure 6.4(c). The ratio value for the homo-nanoparticles was quite constant, ranging from 0.18 to 0.19, whereas it was increased from 0.19 up to 0.38 in case of the striped silver nanoparticles. This implies that the coordination structure around  $\text{Eu}^{3+}$  was changed by the influence of the striped silver nanoparticles nearby, specifically by the interaction with ligands on silver nanoparticles. It can be deduced that silver nanoparticles themselves did not cause the change of the intensity ratio, since it was constant for the homo-nanoparticles, and also it was reported that there was no remarkable change in the ratio only by the presence of silver nanoparticles in the previous work by Hayakawa et al. Therefore, it can be concluded that the increase in the intensity ratio was caused by the interaction with EG3 ligands on the striped nanoparticles, which results in altering the ligand field around  $\text{Eu}^{3+}$ . Unlike the homo-nanoparticles, the striped nanoparticles can provide  $\text{Eu}^{3+}$  ions with an open cavity to be captured with an alternating ligand structure thanks to its characteristic structure. Specifically, the electric-dipole and magnetic dipole transition rate can be described as<sup>19</sup>,

$$W(ED) = \frac{1}{4\pi\epsilon_0} \frac{8\pi^2\nu^2 e^2}{mc^3} \left[ \left( \frac{n^2+2}{3} \right)^2 n \right] f(ED),$$

$$W(MD) = \frac{1}{4\pi\epsilon_0} \frac{8\pi^2\nu^2e^2}{mc^3} n^3 f(MD),$$

respectively, where  $\epsilon_0$  is the dielectric constant in vacuum,  $\nu$  is the frequency of an electronic transition,  $e$  is the electronic quantity of electron,  $m$  is the mass of electron,  $c$  is the velocity of light,  $n$  is the refractive index of the media, and  $f(ED)$  and  $f(MD)$  indicate the oscillator strength of the electric-dipole and magnetic-dipole transitions, respectively. It can be assumed that the electric-dipole transition rate was increased by the change of  $f(ED)$ , caused by the interaction between EG3 ligands on the striped nanoparticles and  $\text{Eu}^{3+}$ .

## 6.5. References

- 1 Singh, C. *et al.* Entropy-mediated patterning of surfactant-coated nanoparticles and surfaces. *Phys Rev Lett* **99**, doi:Artn 226106 Doi 10.1103/Physrevlett.99.226106 (2007).
- 2 McGehee, M. D. *et al.* Narrow bandwidth luminescence from blends with energy transfer from semiconducting conjugated polymers to europium complexes. *Advanced Materials* **11**, 1349-1354, doi:Doi 10.1002/(Sici)1521-4095(199911)11:16<1349::Aid-Adma1349>3.0.Co;2-W (1999).
- 3 Sabbatini, N., Guardigli, M. & Lehn, J. M. Luminescent Lanthanide Complexes as Photochemical Supramolecular Devices. *Coordin Chem Rev* **123**, 201-228, doi:Doi 10.1016/0010-8545(93)85056-A (1993).
- 4 Piguet, C., Bunzli, J. C. G., Bernardinelli, G., Hopfgartner, G. & Williams, A. F. Self-Assembly and Photophysical Properties of Lanthanide Dinuclear Triple-Helical Complexes. *Journal of the American Chemical Society* **115**, 8197-8206, doi:Doi 10.1021/Ja00071a032 (1993).
- 5 Dehorrocks, W. & Collier, W. E. Lanthanide Ion Luminescence Probes - Measurement of Distance between Intrinsic Protein Fluorophores and Bound Metal-Ions - Quantitation of Energy-Transfer between Tryptophan and Terbium(Iii) or Europium(Iii) in the Calcium-Binding Protein Parvalbumin. *Journal of the American Chemical Society* **103**, 2856-2862 (1981).
- 6 Saha, A. K. *et al.* Time-Resolved Fluorescence of a New Europium Chelate Complex - Demonstration of Highly Sensitive Detection of Protein and DNA

- Samples. *Journal of the American Chemical Society* **115**, 11032-11033, doi:Doi 10.1021/Ja00076a088 (1993).
- 7 Zhu, X. J., Wang, X. L. & Jiang, C. Q. Spectrofluorimetric determination of heparin using a tetracycline-europium probe. *Anal Biochem* **341**, 299-307, doi:Doi 10.1016/J.Ab.2005.03.014 (2005).
- 8 Lamture, J. B. & Wensel, T. G. Intensely Luminescent Immunoreactive Conjugates of Proteins and Dipicolinate-Based Polymeric Tb(III) Chelates. *Bioconjugate Chem* **6**, 88-92, doi:Doi 10.1021/Bc00031a010 (1995).
- 9 Richardson, F. S. Terbium(III) and Europium(III) Ions as Luminescent Probes and Stains for Biomolecular Systems. *Chem Rev* **82**, 541-552, doi:Doi 10.1021/Cr00051a004 (1982).
- 10 Nabika, H. & Deki, S. Enhancing and quenching functions of silver nanoparticles on the luminescent properties of europium complex in the solution phase. *J Phys Chem B* **107**, 9161-9164, doi:Doi 10.1021/Jp035741b (2003).
- 11 Lakowicz, J. R., Maliwal, B. P., Malicka, J., Gryczynski, Z. & Gryczynski, I. Effects of silver island films on the luminescent intensity and decay times of lanthanide chelates. *J Fluoresc* **12**, 431-437, doi:Doi 10.1023/A:1021318127519 (2002).
- 12 Louis, C. *et al.* Gold nano-antennas for increasing luminescence. *Advanced Materials* **16**, 2163-+, doi:Doi 10.1002/Adma.200400299 (2004).
- 13 Haase, M., Riwozki, K., Meyssamy, H. & Kornowski, A. Synthesis and properties of colloidal lanthanide-doped nanocrystals. *J Alloy Compd* **303**, 191-197, doi:Doi 10.1016/S0925-8388(00)00628-9 (2000).
- 14 Nabika, H. & Deki, S. Surface-enhanced luminescence from Eu<sup>3+</sup> complex nearby Ag colloids. *Eur Phys J D* **24**, 369-372, doi:Doi 10.1140/Epjd/E2003-00165-X (2003).
- 15 Cheng, D. M. & Xu, Q. H. Separation distance dependent fluorescence enhancement of fluorescein isothiocyanate by silver nanoparticles. *Chem Commun*, 248-250, doi:Doi 10.1039/B612401a (2007).
- 16 Campion, A., Gallo, A. R., Harris, C. B., Robota, H. J. & Whitmore, P. M. Electronic-Energy Transfer to Metal-Surfaces - a Test of Classical Image Dipole Theory at Short Distances. *Chem Phys Lett* **73**, 447-450, doi:Doi 10.1016/0009-2614(80)80692-0 (1980).
- 17 Kang, S. Y. & Kim, K. Comparative study of dodecanethiol-derivatized silver nanoparticles prepared in one-phase and two-phase systems. *Langmuir* **14**, 226-230, doi:Doi 10.1021/La970696i (1998).
- 18 Richardson, F. S. & Brittain, H. G. A Structural Study of Tris(Beta-Diketonate)Europium(III) Complexes in Solution Using Magnetic Circularly Polarized Luminescence Spectroscopy. *Journal of the American Chemical Society* **103**, 18-24, doi:Doi 10.1021/Ja00391a004 (1981).
- 19 Fang, X. N. *et al.* Origin of luminescence enhancement and quenching of europium complex in solution phase containing Ag nanoparticles. *J Chem Phys* **131**, doi:Artn 054506  
Doi 10.1063/1.3193721 (2009).

- 20 Wang, Z., Wang, J. & Zhang, H. J. Luminescent sol-gel thin films based on europium-substituted heteropolytungstates. *Mater Chem Phys* **87**, 44-48, doi:Doi 10.1016/J.Matchemphys.2004.04.016 (2004).

## **7. Conclusions and Future Work**

### **7.1. Ongoing and Future Work**

#### **7.1.1. Striped gold nanoparticles with various ligand compositions**

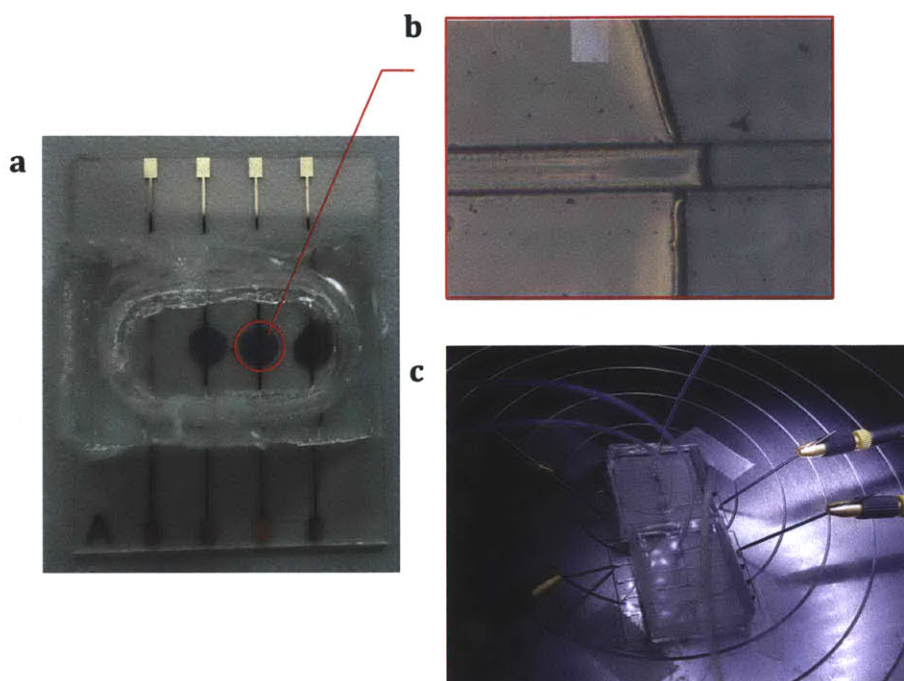
As briefly depicted in Chapter 2, the striped gold nanoparticles with different ligand compositions have different affinities toward metal ions. We have changed only hydrophobic ligands by replacing them with a longer or shorter length of aliphatic carbons and simply altering the other end group to amine or hydroxyl group, which led to a different ion-capturing behavior with a slight modification. For example, calcium ions were captured by OT/EG3 gold nanoparticles, even though not by any HT/EGn nanoparticles. Also, potassium ions were not captured by HT/EG2 gold nanoparticles when the end group of HT ligand was replaced with amine or hydroxyl groups. These imply the change of an electrostatic interaction, accompanied by altering the ligands. Therefore, with other ligands compositions, it would be possible to distinguish more various ions using the striped gold nanoparticles. For future work, both of two ligands can be replaced with other types of ligands. For example, HT ligand can be substituted with more hydrophobic group such as bezenethiol or other aliphatic hydrocarbon thiols. In addition, EG ligand can be also replaced by other ligands including amine groups, as crown ethers have also cyclic polyamine types. With more various ligands pairs, we can enhance the selectivity towards different ions using the striped gold nanoparticles.

### **7.1.2. Manipulation of a metal-ion sensor for a real-time monitoring**

Although our existing sensor device is able to effectively function on the environmental samples, it is vulnerable to a real-time measurement, since the dehydration process is required for a measurement. For the more practical use of the sensor, the system needs to be modified so that it can be directly used for a solution sample.

We have been trying to micro-fabricated chips for a real-time monitoring of metal ion concentration, using striped gold nanoparticles, by adopting the microfluidic system<sup>1,2</sup>. Specifically, several kinds of platinum electrodes with different sizes and gaps, ranging from 20nm to 100 nm, were patterned on a Pyrex substrate. The electrodes were covered with a 40  $\mu\text{m}$  layer of SU8 so that we could identify the surface area of the electrodes exposed to nanoparticles. The striped gold nanoparticles were drop-casted onto the substrate and cross-linked to prevent them from dissolving out in water. Finally, an ad hoc microfluidics was built, and the system was connected to a syringe pump and a reservoir to allow a real-time measurement (Figure 7.1). By flushing different kinds of aqueous ion solutions through the microfluidics, the current change upon the flow of ions will be measured, and it is expected that the interaction of the striped gold nanoparticles with metal ions would change the current. Even though more optimization process will be required to observe a remarkable change depending on the concentration, it

is highly optimistic to fabricate the real-time monitoring sensor, and it will be a very powerful tool to determine the amount of metal ions in a real life.



**Figure 7.1.** A schematic representation of a real-time monitoring sensor: (a) the picture of a chip with several electrodes, (b) gold nanoparticles between the electrodes, and (c) the set-up for measurement.

### 7.1.3. Sensor array for detecting multiple ions

With these several kinds of nanoparticles, it will be possible to fabricate a sensor array to detect the presence or even an approximate concentration of metal ions. There have been lots of reports regarding various sensor arrays that can detect explosives, DNA or organic compounds, using a mechanical, colorimetric or electronic signal (called “artificial nose”)<sup>3-6</sup>. In a similar way, each striped nanoparticle can be manipulated to be array-based device and function as a metal-

ion sensor, since each nanoparticle would have a different affinity towards each ion, resulting in a different signal. Therefore, it will be able to perform an excellent sensor for metal ions, combining with a real-time monitoring function described in the previous section.

#### **7.1.4. Modification of the metal ion sponge**

In Chapter 4, it was described that the metal ion-absorbing sponge made up of the striped gold nanoparticles was able to get rid of a substantial amount of toxic ions from water and also sediment. However, it was not so satisfactory since the nanoparticles did not fulfill its function perfectly. In other words, the metal ions would have been completely absorbed by gold nanoparticles if the metal ion sponge had performed its function more effectively. As mentioned in Chapter 4, it was regarded as an engineering problem, and it will be able to be improved, fulfilling a mechanical property so that it can serve as an excellent metal ion absorbent, resulting in a more efficient remediation.

#### **7.1.5. Striped nanoparticles with different core materials**

This will make it possible to produce a cheaper metal ion sensor and also metal ion sponge in the case of that it is actually used in a real life. As described in Chapter 6, it would be highly possible to prepare the striped nanoparticles with a different core material if the ligand molecules have an appropriate well-adsorbing functional



group. Even though our metal ion sensor and sponge were re-usable, it will be more economical if we can manipulate them with different cheaper core materials.

#### **7.1.6. Manipulation of a filter membrane for remediation**

As for another remediation method, a filter membrane consisting of the striped gold nanoparticles can be a very promising tool. In Chapter 4, the metal ion sponge made up of the gold nanoparticles was introduced, successfully removing some of metal ions as an absorbent. In a similar way, a filter membrane with the gold nanoparticles can be fabricated by incorporating into a porous material<sup>7,8</sup>, and by simply flowing water contaminated by metal ions through the filter membrane, it will be able to successfully play a role in water purification.

### **7.2. Conclusion**

We have demonstrated that various kinds of metal ions could be selectively captured by striped gold nanoparticles. Through the solution-based conductivity tests, it was firstly illustrated that a certain metal ion made a complex with a specific type of striped nanoparticles with a proper pair of ligands, and those interactions were characterized by a series of spectroscopic experiments.

Based on the fundamental results, we successfully exploited the solid-state metal ions sensor using striped gold nanoparticles with an unprecedented detection limit,

especially for methylmercury and cadmium. Also, it was proven that it has a strong possibility for the use in a real-life, exhibiting the excellent methylmercury detection of environmental samples such as a tap water, lake sample, and fish sample.

Furthermore, our striped gold nanoparticles were able to perform the remediation of metal ions from water and sediment by incorporating into magnetic nanoparticles or by being fabricated into a pellet, functioning as a metal ion sponge.

In addition, it was observed that the ion-capturing by striped gold nanoparticles displayed a different behavior, depending on the temperature, which was induced by a higher contribution of entropy to free energy. This kind of phenomenon was not shown in the rigid structure of macrocyclic rings; however, it would be possible for our striped nanoparticles due to the flexibility of the ion-capturing moiety.

Finally, the possibility of the formation of the striped structure with a different core material was presented with silver nanoparticle by particularly investigating the effect of the striped silver nanoparticles on luminescent properties of  $\text{Eu}^{3+}$  ions.

### 7.3. References

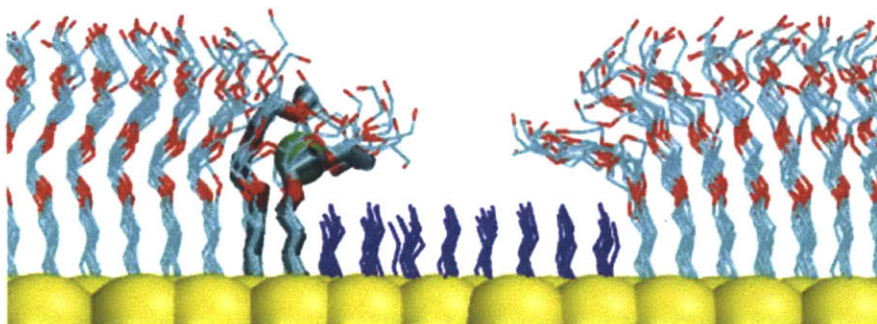
- 1 Guiducci, C. *et al.* Integrating Bio-sensing Functions on CMOS Chips. *Proceedings of the 2010 IEEE Asia Pacific Conference on Circuit and System (Apccas)*, 548-551 (2010).
- 2 Temiz, Y., Ferretti, A., Leblebici, Y. & Guiducci, C. A comparative study on fabrication techniques for on-chip microelectrodes. *Lab Chip* **12**, 4920-4928, doi:10.1039/c2lc40582b (2012).
- 3 Zhang, C. & Suslick, K. S. A colorimetric sensor array for organics in water. *J Am Chem Soc* **127**, 11548-11549, doi:10.1021/ja052606z (2005).

- 4 Roy, S. *et al.* Mass-produced nanogap sensor arrays for ultrasensitive detection of DNA. *J Am Chem Soc* **131**, 12211-12217, doi:10.1021/ja901704t (2009).
- 5 Baller, M. K. *et al.* A cantilever array-based artificial nose. *Ultramicroscopy* **82**, 1-9, doi:Doi 10.1016/S0304-3991(99)00123-0 (2000).
- 6 Gardner, J. W., Bartlett, P. N. & North Atlantic Treaty Organization. Scientific Affairs Division. *Sensors and sensory systems for an electronic nose*. (Kluwer Academic, 1992).
- 7 He, J. B. *et al.* Fabrication and Mechanical Properties of Large-Scale Freestanding Nanoparticle Membranes. *Small* **6**, 1449-1456, doi:Doi 10.1002/Smll.201000114 (2010).
- 8 Hanaoka, T., Kormann, H. P., Kroll, M., Sawitowski, T. & Schmid, G. Three-dimensional assemblies of gold colloids in nanoporous alumina membranes. *Eur J Inorg Chem*, 807-812 (1998).

## Appendix

### A.1. Theoretical explanation for ion-capturing by striped nanoparticles

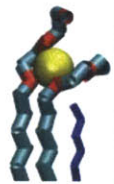



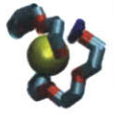
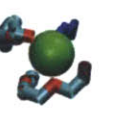


(Done by Dr. Hao Jiang from Prof. Sharon Glotzer group at University of Michigan)



**Figure A.1.** Molecular simulations of ion trapping; a snapshot from MD simulations shows that the ion is trapped near the edge of an EGn stripe

The striped nanoparticles exhibit a great selectivity without a classical rigid-like structure, which would be classically regarded as a good and selective ion-chelating structure. To understand this phenomenon, molecular dynamics simulations were performed on HT/EGn monolayers, as illustrated in Figure A.1. The system was constructed with a flay layer of the ligands at the center of the simulation box filled with water molecules and metal ions, and the ligands were assembled in the spacing of 0.45 nm, which was commensurate with the experimental spacing observed in STM. Three different kinds of system were studied: an EG2 homo-system, a mixed HT/EG2 system, and a HT/EG3 mixed system. Also, for both the HT/EG2 and HT/EG3 systems, EGn ligands comprised 75 % and HT ligands did 25 % of the

ligands, forming the stripes of alternating components.

	HT/EG <sub>2</sub>		HT/EG <sub>3</sub>	
	K <sup>+</sup>	Cs <sup>+</sup>	K <sup>+</sup>	Cs <sup>+</sup>
Life-time	>50 ns	2.4 ns	16 ns	>50 ns
Side View				
Top View				
	(a)	(b)	(c)	(d)

**Figure A.2.** The structures and lifetime of the longest-lasting ion-trapping motifs found in the simulations of the HT/EG<sub>2</sub> and HT/EG<sub>3</sub> nanoparticles: the trapped K<sup>+</sup> and Cs<sup>+</sup> ions are represented by yellow and green balls, respectively. The EGN ligand is represented using multi-colored sticks with the cyan and red portions respectively representing the carbon and oxygen atoms. All hydrogen atoms in the ligands are hidden from all views.

In the overall simulation, it was shown that the metal ion had a tendency to bind at the edges of the EGN stripes with the ethylene glycol units bending over the neighboring HT molecules and encaging around the ions, as depicted in Figure A.1. Specifically, upon introduction of ions in the systems the simulations showed that the EG<sub>2</sub> homo-SAMs had no substantial binding, while the HT/EG<sub>2</sub> monolayer had

significant binding for  $K^+$  but much smaller binding for  $Cs^+$ . Furthermore, it was demonstrated that the HT/EG3 monolayer bound more  $Cs^+$  than  $K^+$ , as experimentally observed. The binding happened by a mechanism that involves the ethylene glycol units near the border with the HT molecules to bend over the latter, and, upon the presence of an incoming ion, collaboratively form a cage enclosing the ion. It was observed that the binding resembled a cryptand for the most part involved two EGN molecules. Once formed, the cryptand-like structural part was able to persist for a certain amount of time, effectively trapping the captured ion inside the motif. It was found in the simulations that the stability of these motifs in both the EG2/HT and EG3/HT monolayers significantly depended on the specie of the ion being trapped. As depicted in Figure A.2, the longest-lasting  $K^+$ -binding motif had a lifetime larger than 50 ns in the EG<sub>2</sub>/HT monolayer, being still stable at the time the simulation ends, whereas the  $Cs^+$ -binding motifs could persist no longer than 3 ns. The relative order of stability of the  $K^+$ - and  $Cs^+$ -binding motifs changed in the EG<sub>3</sub>/HT monolayer, with the lifetime being about 16 ns and >50 ns for the most stable  $K^+$ - and  $Cs^+$ -trapping motifs, respectively.

The stability of the ion-capturing motif can be understood in terms of the change of free energy associated with the formation of the motif and the binding of the ion to the motif. Such free energy change is dominated by three competing factors. The first one is the energetic gains coming from the attractive electrostatic interactions between the captured ion and the oxygen atoms in the EG units constructing the motif, which stabilizes the motif. The second and third factors, both destabilize the

motif, are the loss of the entropic degrees of freedom associated with the localization of the ion inside the motif, and that with the reduction of the motions of the head groups of the EGN ligands forming the motif, which are otherwise able to wag freely at the empty space above the neighboring HT domain. The motif is stable when the energetic gain exceeds the total loss of entropy, as in the case where a  $K^+$  ion is trapped by the motif formed with 4 EG units (4-EG motif, shown in Figure A.2(a)) in the EG2/HT monolayer. The stability changes if, instead of a  $K^+$  ion, a  $Cs^+$  ion is trapped inside the 4-EG motif, as shown in Figure A.2 (b).  $Cs^+$  ion is larger in size, costing more entropic loss if localized. Moreover, the energetic gain from ion binding would be similar for  $K^+$  ion and for  $Cs^+$  ion because they have the same electric charge. The combination of these factors results in a net increase of free energy, rendering the 4-EG motif less stable when the ion trapped inside changes from  $K^+$  to  $Cs^+$ .

The situation is different with motifs formed by EG3 ligands in the EG3/HT monolayer. Since EG3 ligands have one more EG unit in each head group, they are capable to form larger motifs. When a  $Cs^+$  ion is trapped, all EG units in the head groups are utilized to form a large motif (6-EG motif, shown in Figure A.2(d)) encaging the  $Cs^+$  ion. The 6-EG motif provides more rooms than does the 4-EG motifs formed in the EG2/HT monolayer, effectively reducing the entropic cost of confining the  $Cs^+$  ion. At the same time, in the 6-EG motif there are more EG units interacting closely with the bound  $Cs^+$  ion, increasing the energetic gain. As a result, the  $Cs^+$ -trapping motif in the EG3/HT monolayer is much more stable than that in

the EG<sub>2</sub>/HT monolayer. When a K<sup>+</sup> ion is trapped in the EG<sub>3</sub>/HT monolayer, only the two outmost EG units in each head group of the EG<sub>3</sub> ligands are utilized to construct a motif (4-EG motif, shown in Figure A.2 (c)), which highly resembles the ones formed by the EG<sub>2</sub> ligands in the EG<sub>2</sub>/HT monolayer. However, compared to the case in the EG<sub>2</sub>/HT monolayer, the formation of such motif in the EG<sub>3</sub>/HT monolayer gives rise to more entropic penalty, with the extra penalty arising from the reduction of the motions of the extra EG units that are in the same EG<sub>3</sub> ligands and coupled with the motifs. Consequently, the stability of the K<sup>+</sup>-trapping motif is largely reduced in the EG<sub>3</sub>/HT monolayer.

The analysis above shows that the formation of the ion-trapping motifs is a key mechanism for the observed selective ion trapping phenomena. We note that this mechanism is very sensitive to local molecular environment rather than global order. Hence particles with a random mixture of HT and EG<sub>n</sub> molecules should show similar binding ability but lower selectivity.

## **A.2. Supporting Materials for Metal Ion Sensor (Chapter 3)**

(Taken from Cho, E. S.; Kim, J.; Nakanishi, H.; Jiang, H.; Tejerina, B.; Yu, M.; Patashinski, A. Z.; Glotzer, S.; Stellacci, F.; Grzybowski, B.A. " *Nature Materials* 2012, 11, 978-985)

### **A.2.1. Determination of the detection limit**



A two-sample  $t$ -test was performed to find out the detection limit of each pair of nanoparticle and metal ion, using  $\chi$  values (i.e. the ratio of the conductance of the film,  $\chi = \sigma_{after}/\sigma_{before}$ ) for two different concentrations of each metal ion solution, at 99% confidence level; hence, the detection limit was determined as p-value was larger than 0.01. The result was summarized in Table A.1.

NP:Cation Type	Two sample	$t$ -statistics	p-value	detection limit
HT/EG <sub>3</sub> :CH <sub>3</sub> Hg <sup>+</sup>	10 <sup>-4</sup> M, 10 <sup>-7</sup> M	434.1527	0	<b>10<sup>-18</sup>M</b>
	10 <sup>-7</sup> M, 10 <sup>-8</sup> M	40.01132	0	
	10 <sup>-8</sup> M, 10 <sup>-12</sup> M	54.4155	0	
	10 <sup>-12</sup> M, 10 <sup>-15</sup> M	21.90244	0	
	10 <sup>-15</sup> M, 10 <sup>-18</sup> M	3.08378	0.003	
	10 <sup>-18</sup> M, 10 <sup>-21</sup> M	<b>2.0318</b>	<b>0.029</b>	
HT/EG <sub>3</sub> :Cs <sup>+</sup>	10 <sup>-3</sup> M, 10 <sup>-6</sup> M	<b>2.404701</b>	<b>0.013</b>	<b>10<sup>-6</sup>M</b>
	10 <sup>-6</sup> M, 10 <sup>-9</sup> M	1.044072	0.142	
	10 <sup>-9</sup> M, 10 <sup>-12</sup> M	0.780784	0.164	
HT/EG <sub>2</sub> :Cd <sup>2+</sup>	10 <sup>-3</sup> M, 10 <sup>-6</sup> M	10.14517	0	<b>10<sup>-12</sup>M</b>
	10 <sup>-6</sup> M, 10 <sup>-9</sup> M	3.73495	0	
	10 <sup>-9</sup> M, 10 <sup>-12</sup> M	2.826025	0.005	
	10 <sup>-12</sup> M, 10 <sup>-15</sup> M	<b>-0.03359</b>	<b>0.5</b>	
	10 <sup>-15</sup> M, 10 <sup>-18</sup> M	1.7713	0.043	
HT/EG <sub>2</sub> :K <sup>+</sup>	10 <sup>-3</sup> M, 10 <sup>-5</sup> M	25.89332	0	<b>10<sup>-12</sup>M</b>
	10 <sup>-5</sup> M, 10 <sup>-6</sup> M	4.05654	0	
	10 <sup>-6</sup> M, 10 <sup>-9</sup> M	6.806372	0	
	10 <sup>-9</sup> M, 10 <sup>-12</sup> M	4.781077	0	
HT/EG <sub>1</sub> :Zn <sup>2+</sup>	10 <sup>-3</sup> M, 10 <sup>-6</sup> M	6.819308	0	<b>10<sup>-9</sup>M</b>
	10 <sup>-6</sup> M, 10 <sup>-9</sup> M	3.29275	0.002	
	10 <sup>-9</sup> M, 10 <sup>-12</sup> M	<b>1.178061</b>	<b>0.121</b>	
	10 <sup>-12</sup> M, 10 <sup>-15</sup> M	1.441561	0.088	
HT/EG <sub>1</sub> :Na <sup>+</sup>	10 <sup>-3</sup> M, 10 <sup>-6</sup> M	5.376975	0	<b>10<sup>-6</sup>M</b>
	10 <sup>-6</sup> M, 10 <sup>-9</sup> M	<b>1.133184</b>	<b>0.142</b>	

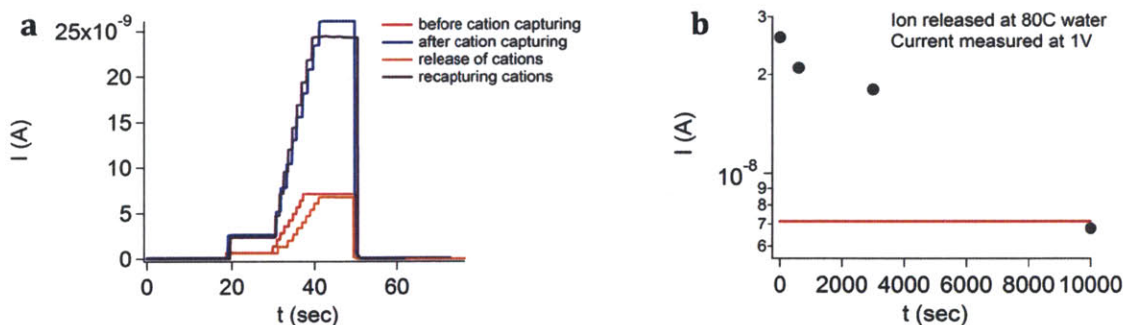
**Table A.1.** Detection limits for each pair of nanoparticle and metal ion determined by the two-sample  $t$ -test at the 99 % confidence level

## A.2.2. Reversibility of the sensor

A sensor to be utilized practically as needs to be reversible. As illustrated in Chapter

2, the striped nanoparticles released the capture ions at high temperature (80 °C) as a result of the entropic effect. Therefore, we were able to assume that the captured ions would be released from the nanoparticle film on the sensor and the conductance of the sensor would be recovered to its initial value.

The conductance values of the films before and after ion-capturing, also after ion-releasing and re-capturing were examined. The metal ion release was accomplished by immersing the nanoparticle films in 80 °C water for 2~3 hours. It was observed that there was no change in the integrity of the film during this immersing procedure. The obtained results were shown in Figure A.3(a), and it was observed that the conductivities returned to their initial values before ion binding after releasing ions. We could conclude that the films were reversible and the conductance change was only dependent on ion binding.



**Figure A.3.** Reversibility of the film of the striped nanoparticle (a) I-V characteristic plots of the film of HT/EG2 particles (i) before no ion binding, (ii) after binding  $\text{Cd}^{2+}$  ions, (iii) after releasing  $\text{Cd}^{2+}$  by putting the film in 80 °C water, and (iv) after re-binding  $\text{Cd}^{2+}$  ions, (b) the change in conductance of HT/EG2 striped nanoparticle film as a function of time from which  $\text{Cd}^{2+}$  ions are being released

Furthermore, the ion releasing from the film was examined in the aspect of kinetics (Figure A.3(b)). The conductance was measured as a function of time, and it took approximately 3 hours to recover to its initial value. The ion-releasing in the nanoparticle film took longer than that in the nanoparticle solution, and we assumed that it was attributed to the difference in their states; the nanoparticles in solutions would be more easily affected by the temperature since they had larger surface area exposed to hot water and also were not cross-linked each other, which meant they were less restrained.

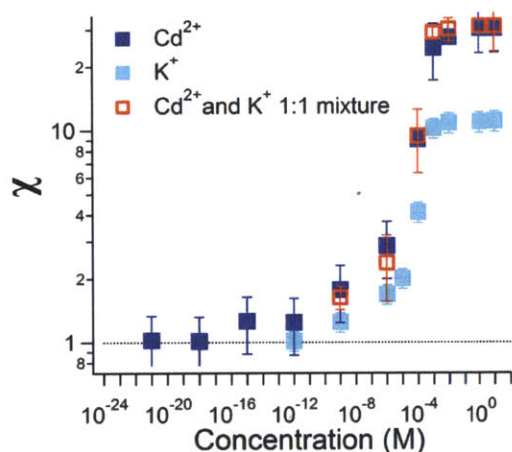
### A.2.3. Selectivity upon the exposure to mixed ions

	$\chi^{\text{binding}}$	$\chi^{\text{non-binding}}$	$\chi^{\text{mixture}}$
HT/EG3 AuNPs	$\chi^{\text{Cs}^+}=1.600 \pm 0.512$	$\chi^{\text{Na}^+}= 0.888 \pm 0.165$	$\chi^{\text{Cs}^+/\text{Na}^+}= 1.671 \pm 0.389$
HT/EG2 AuNPs	$\chi^{\text{Cd}^{2+}}= 2.859 \pm 0.858$	$\chi^{\text{Zn}^{2+}}= 1.170 \pm 0.182$	$\chi^{\text{Cd}^{2+}/\text{Zn}^{2+}}= 2.373 \pm 1.238$
HT/EG1 AuNPs	$\chi^{\text{Zn}^{2+}}= 2.337 \pm 0.716$	$\chi^{\text{Cd}^{2+}}= 1.105 \pm 0.125$	$\chi^{\text{Zn}^{2+}/\text{Cd}^{2+}}= 2.406 \pm 0.383$

**Table A.2.** The film sensitivity upon the exposure to the mixture of metal ions

As briefly discussed in Chapter 2, it is essential that the sensor has a superior selectivity, along with an excellent sensitivity. The selectivity of the film of the striped nanoparticles was evaluated upon the exposure to the mixture of ions. Each nanoparticle film was immersed in the mixture of a binding ion and a non-binding ion, and  $\chi$  valued was investigated in each case. The result was described in Table A.2. Specifically, for the film of HT/EG3 striped nanoparticles with  $\text{Cs}^+$  ions, the  $\chi$

value was not substantially influenced by the presence of  $\text{Na}^+$  ions, and similarly for the film of HT/EG2 nanoparticles, the change of the conductivity caused by  $\text{Cd}^{2+}$  was subtle in the presence of supplementary  $\text{Zn}^{2+}$ . Also, in reverse the presence of  $\text{Cd}^{2+}$  did not largely affect the  $\chi$  value of HT/EG1 nanoparticles by  $\text{Zn}^{2+}$ . These results confirms that the solid-state sensor displays an outstanding selectivity in presence of other non-binding ions, and also the  $\chi$  value is not influenced by the change of the ionic strength of the solution, resulting from non-binding ions.



**Figure A.4.** The film selectivity of HT/EG2 striped particles upon exposure to the mixture of  $\text{Cd}^{2+}$  and  $\text{K}^+$

However, the selectivity would decrease when the film of the nanoparticles are exposed to the mixture of the binding ions. This problem is not significant for the film of HT/EG3 particles, of which  $\chi$  value for  $\text{CH}_3\text{Hg}^+$  is considerably larger than that for  $\text{Cs}^+$  or  $\text{Hg}^{2+}$ , whereas it becomes tricky for the films of HT/EG1 and HT/EG2 nanoparticles. For example, the signals of HT/EG2 gold nanoparticles from  $\text{K}^+$  and  $\text{Cd}^{2+}$  were quite similar to that from the mixture of two of them, as demonstrated in

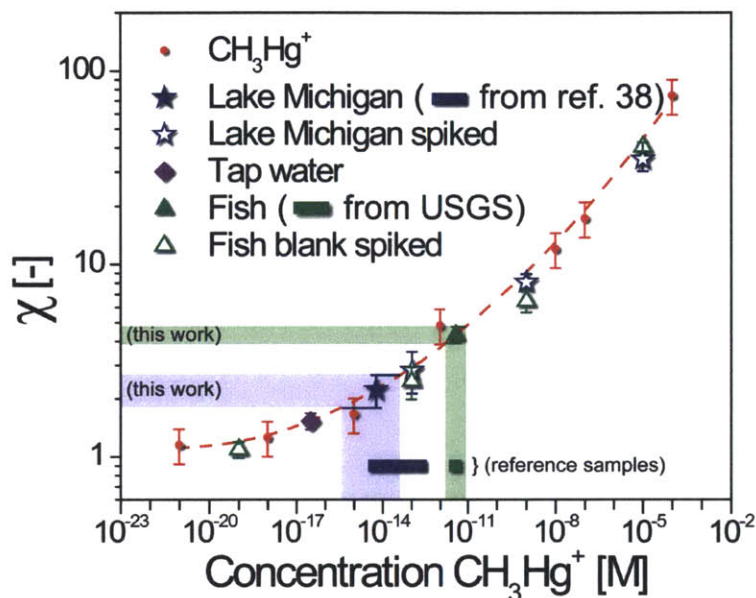
Figure A.4. It was not surprising, nevertheless, since the binding constants for  $K^+$  and  $Cd^{2+}$  against HT/EG2 nanoparticles were similar as illustrated in Chapter 2 from ITC measurement; therefore, it was predictable that the binding to HT/EG2 nanoparticles would be competitive when they were in the same solution. However, it seems different when closely observed, since the  $\chi$  values from the mixture  $K^+$  and  $Cd^{2+}$  in a series of measurements were very similar to those from pure  $Cd^{2+}$ . From this result, it was deduced that  $K^+$  and  $Cd^{2+}$  would be captured to different sites on HT/EG2 nanoparticles and  $Cd^{2+}$  would tend to be bound more selectively in a more ordered site.

#### **A.2.4. Application to environmental samples**

As described in the previous section, the film of HT/EG3 striped nanoparticles would present a superior selectivity, especially for  $CH_3Hg^+$ , in the presence of the mixed ions. Also, considering that the detection of  $CH_3Hg^+$  is of paramount importance, it was certainly worth testing it in real environmental samples.

Three kinds of environmental samples were tested with our solid-state sensor to determine the concentration of  $CH_3Hg^+$ : tap water, lake water, and fish sample. Prior to the sample preparation, all glasswares were cleaned with HCl solutions at 65 °C and washed with Millipore water sufficiently to prevent other contaminations. Tap water was used as obtained, and lake water was collected from Lake Michigan. Fish samples were acquired from the USGS (the United States Geological Survey), which

was approximately 10 mg of lyophilized mosquito fish from Everglades National Park, and the fish sample was prepared by following the protocol of USGS. The result was illustrated in Figure A.5.



**Figure A.5.** Selectivity of the film of HT/EG3 striped nanoparticles on exposure to ion mixtures and environmental samples

Firstly, the calibration curve (marked with red symbol) was drawn from the measurements of standard solution samples (i.e. the solution of the known  $\text{CH}_3\text{Hg}^+$  concentration in Millipore water), followed by the second order polynomial fit. Green symbols correspond to the values from fish samples and blue symbols are from the values from Lake Michigan samples. For both cases, open symbols correspond to the sample spiked with a known  $\text{CH}_3\text{Hg}^+$  concentration. The resulting value from Lake Michigan sample was directly compared to the one from the literatures, which tested the same sample, i.e. Lake Michigan, and the obtained concentration from fish sample was compared to the value decided by USGS.

For the lake water, the concentration of  $\text{CH}_3\text{Hg}^+$  from our measurement was 5.9 fM with a range of 0.35~43.3 fM, and the reported value from the literature was 5~210 fM<sup>1</sup>. Also, the amount of  $\text{CH}_3\text{Hg}^+$  for the fish sample was 3.81 pM with a range of 1.62~8.19 pM, and the reference value obtained from USGS was 3.58 pM. Both measurements gave the values in an excellent agreement with the reference ones, implying that the film of the striped nanoparticles will be a highly promising tool in a real life to determine the concentration of toxic ions. The concentration of  $\text{CH}_3\text{Hg}^+$  in the tap water was 27.7 aM with a range of 4.5~138 aM, which is very low.

Furthermore, it was demonstrated that the  $\chi$  values from the environmental samples spiked with known concentrations of  $\text{CH}_3\text{Hg}^+$  fell onto the calibration curves, which means that there is no background interference from other elements in the environmental samples. More importantly, our measurement was conducted quite straightforwardly, compared to other methods, which require tedious sample preparation procedures.

### A.3. References

- 1 Sullivan, K. A. & Mason, R. P. The concentration and distribution of mercury in Lake Michigan. *Sci Total Environ* **213**, 213-228, doi:Doi 10.1016/S0048-9697(98)00094-1 (1998).